Quark and Nuclear Matter with Fluctuations

Institut für theoretische Physik

Zur Erlangung des Grades
eines Doktors der Naturwissenschaften
(Dr. rer. nat.)

vorgelegte Dissertation von
M.Sc. Johannes Weyrich

Gießen 2018

Referent: Prof. Dr. Lorenz von Smekal
Korreferent: Prof. Dr. Christian Fischer

Zusammenfassung

Quantenchromodynamik (QCD) ist die Quantenfeldtheorie der starken Wechselwirkung, deren fundamentale Freiheitsgrade Quarks und Gluonen sind. QCD spielt eine entscheidene Rolle bei der Beschreibung physikalischer Phänomene, welche vom frühen Universum bis zu Wechselwirkungen innerhalb der Atomkerne reichen, die die Welt um uns herum ausmachen. Die Erforschung des Phasendiagramms stark wechselwirkender Materie ist eine große wissenschaftliche Herausforderung, der außerordentlicher experimenteller und theoretischer Aufwand gewidmet wird.

In dieser Arbeit untersuchen wir das Phasendiagramm der QCD mit chiral effektiven Modellen unter Verwendung der funktionalen Renormierungsgruppe, einer nichtperturbativen Methode zur Untersuchung von Quantenfeldtheorien. Wir verwenden das 2-Flavor Quark-Meson-Modell als effektives Modell der Niederenergie QCD und berechnen sowohl das entsprechende Phasendiagramm als auch Quark Spekralfunktionen, die wir aus analytisch fortgesetzten RG-Flussgleichungen gewinnen können. Zur Beschreibung von Kernmaterie benutzen wir ein chirales Baryon-Meson-Modell, das Parity-Doublet-Modell, welches den Baryonen erlaubt einen Dirac-Massenterm zu bekommen, ohne die chirale Symmetrie zu brechen. Mit diesem Modell lässt sich sowohl der flüssig-gas Phasenübergang nuklearer Materie als auch chirale Symmetrierestaurierung bei hohen Baryondichten beschreiben. Wir werden diesbezüglich Rechnungen sowohl in der sogenannten extended mean-field Näherung, als auch unter Berücksichtigung mesonischer und fermionischer Fluktuationen mit der FRG durchführen.

Abstract

Quantum Chromodyamics (QCD) is the quantum field theory of strong interactions, which have quarks and gluons as their fundamental degrees of freedom. QCD plays a crucial role in describing phenomena ranging from the early universe to forces within nuclei, which make up the world around us. The exploration of the phase diagram of strongly interacting matter is a scientific challenge a lot of effort is put in from experimental as well as theoretical groups around the globe.

In this thesis, we explore the phase diagram of QCD using chiral effective models within the non-perturbative framework of the functional renormalization group (FRG). We use the two-flavor quark-meson model as an effective model for low-energy QCD, calculating its phase diagram as well as quark spectral functions, which are obtained from analytically continued RG flow equations. For modelling nuclear matter we use a chiral baryon-meson model, the so-called parity-doublet model, which allows for the baryons to acquire a Dirac mass term without breaking chiral symmetry. This model can describe the liquid-gas transition of nuclear matter together with chiral symmetry restoration in the high baryon density phase and will be considered in the extended mean-field approximation as well as including mesonic and fermionic fluctuations using the FRG.

Contents

1 Introduction

Quantum Chromodynamics (QCD) is the well established theory of the strong interaction and as such responsible for a variety of physical phenomena. From the nuclear forces binding quarks and gluons together to form nucleons and eventually nuclei as the building blocks of the world that surrounds us, to strong interaction matter under the most extreme conditions. At small densities and extremely large temperatures QCD gives insight to the evolution of the early universe only fractions of a second after the Big Bang, whereas under cold but extremely dense conditions stellar objects like neutron stars and even more exotic states like color superconducting phases can be studied. QCD together with the electroweak force[1] constitutes the Standard Model of particle physics, covering three of the four fundamental forces in physics, where only the gravitational force so far is left out. The Standard Model of particle physics has been very successful in describing and predicting experimental findings for many years and is so far the best attempt of a uniform description of particle physics.

Back in the 1930s protons and neutrons were believed to be the fundamental building blocks that make up nuclei. Furthermore, the problem why electromagnetic forces had infinite range while strong (nuclear) forces only seemed to have a limited range in the femtometer scale, was still an unsolved issue at that time. Yukawa then made the argument, that the range of the electromagnetic force was infinite because its associated exchange particle, the photon, is massless. Consequently, he proposed a new massive particle as the exchange particle of the strong force, which he called meson [1]. It was not until 1947 that this proposed particle, matching Yukawa's requirements, was discovered and eventually called pion [2]. Even though we know now, that the pion itself is a composite particle and is in fact not the fundamental exchange boson of the strong force, Yukawa's work still gave an important impulse in the advancement of the theory of the strong interactions. For example in the

[1] The electroweak force itself is a unification of the theory of electromagnetism and the weak interaction (or weak force) which is for example responsible for the beta decay of nuclei.

low energy regime of QCD its interaction can even be described by effective pion exchange, since the effective degrees of freedom are pions and nucleons rather than quarks and gluons, giving rise to the important field of chiral effective field theory (χEFT) [3].

In 1964 Gell-Mann proposed that baryons are made up out of three quarks and mesons out of quark anti-quark pairs [4], making it possible to describe most particle spectra at the time. This quark model later on got refined by introducing a so-called color charge, similar to the charge in quantum electrodynamics (QED). In QED the charged spin-1/2 particles are electrons which couple to the photon, as the spin-1 exchange particle by which the electrons interact. Analogous to that in QCD the quarks are the spin-1/2 particles which carry color charge and couple to spin-1 exchange particles which are called gluons. In QCD, in contrast to QED, the gluon itself carries color charge as well. Furthermore three different colors were postulated, and physical states had to be color neutral, consisting either of three quarks or a quark and an antiquark. The first coherent formulation of quantum chromodyamics as the quantum field theory of the strong interaction was given in 1973 by Gell-Mann, Fritzsch and Leutwyler [5].

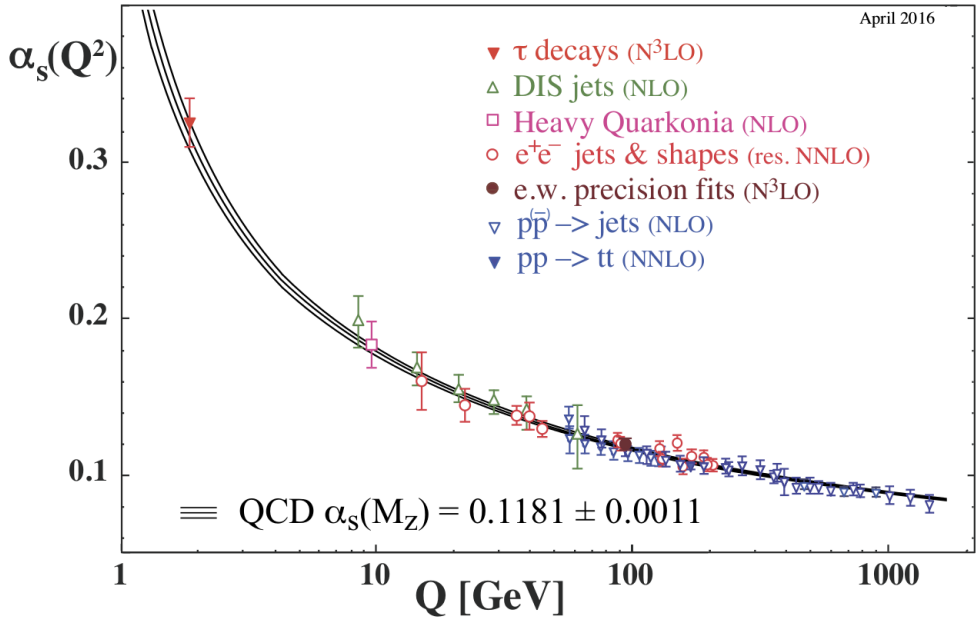

Figure 1.1.: The QCD running coupling α_s as a function of momentum transfer Q. Shown are theoretical predictions in comparison with a variety of experimental data. Figure taken from [6].

Already in 1969 deep inelastic electron-proton scattering experiments that were performed at the Stanford linear accelerator (SLAC) showed a peculiar scaling behaviour of the proton structure function, indicating that the electrons were scattered on unbound almost massless particles within the proton itself [7]. This puzzle could eventually be solved by Gross, Wilczek and Politzer in 1973, when they derived that quantum chromodynamics shows asymptotic freedom [8, 9]. Gross, Wilczek

and Politzer received the Nobel Prize in physics for their discovery in 2004, about 30 years after their publications.

$$\beta(\alpha_s) = -\left(11 - \tfrac{2}{3}N_f\right)\frac{\alpha_s^2}{2\pi} + \mathcal{O}(\alpha_s^4) \tag{1.1}$$

Eq. (1.1) sums up Gross, Wilczek and Politzer's result. The beta function, as the derivative of the coupling with respect to the energy scale, for the case of QCD, with gauge group $SU(3)$ and N_f quark flavors. This means that for QCD with $N_f \leq 16$ the beta function is negative, consequently the coupling becomes smaller and smaller for large energy scales, hence small length scales. This is depicted in Fig. 1.1, which shows the running coupling of QCD as a function of momentum transfer Q, for a variety of different experimental data together with theoretical predictions. In the large energy regime it thus follows that perturbation theory is applicable, whereas in the low energy regime the use of non-perturbative methods becomes inevitable.

Physical states in QCD, for example baryons and mesons, are understood as colorless states (color singlets) made up of quarks and gluons. This means that color charges are not observable in asymptotic states, they are confined inside the respective hadrons. This effect is called confinement and is the reason why single quarks or gluons cannot be observed in experiments. Confinement is commonly understood as a linear rising potential generated by a flux tube between color charges when trying to separate a quark anti-quark pair from each other [10]. At a certain point the energy stored in this flux tube gets large enough to generate another quark anti-quark pair, thus making it impossible to isolate a single quark.

Another important mechanism in the low energy regime of QCD is spontaneous chiral symmetry breaking. It explains why the pions with $m_\pi \simeq 140$ MeV have a much smaller mass than the rest of the hadrons. Pions are understood as the (pseudo-)Nambu-Goldstone bosons of spontaneously broken chiral symmetry.

Putting everything together, there is a good understanding of QCD at high energies where it is mainly managed by asymptotic freedom leading to almost free quarks and gluons. At low energies anyway, QCD is governed by color confinement and spontaneous chiral symmetry breaking. In that regime quarks and gluons are locked inside of baryons and mesons, which means that the degrees of freedom of strongly interacting matter drastically change from high to low energy scales. It is thus expected that at certain energies a change of degrees of freedom, in other words a phase transition (of some kind), has to happen.

The phase structure of strongly interacting matter is summarized in the QCD phase diagram. Much as any other phase diagram, it gives insight to thermodynamic properties and phases of QCD matter at different temperatures and densities. For QCD it is most commonly pictured in the temperature T vs. baryon chemical potential μ_B plane. A conjectured version of the QCD phase diagram is shown in Fig 1.2. For low to intermediate temperatures and chemical potentials there is a hadronic phase, whereas at very high temperatures and chemical potentials quarks and gluons form the so-called quark-gluon plasma [11].

A very successful non-perturbative method to study the QCD phase diagram, especially at vanishing densities, is lattice QCD. In lattice QCD the 4 dimensional Euclidean space-time is discretized on a finite space-time lattice, turning the infinite

dimensional path integrals into a finite number of regular integrals which are then calculated using Monte-Carlo methods.

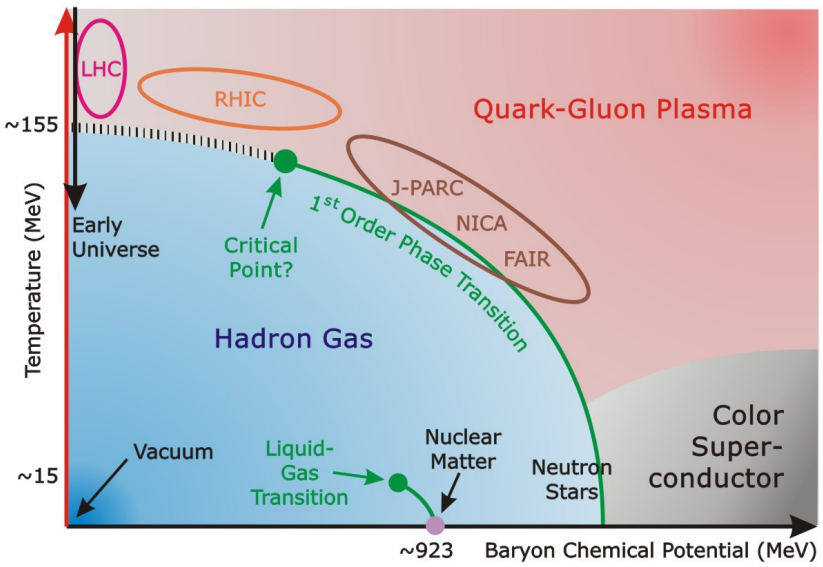

Figure 1.2.: Schematic view of the QCD phase diagram in the $T - \mu$ plane. Figure by courtesy of D. Rischke.

Already in the 1980s the existence of a confinement-deconfinement transition could be confirmed in studies of pure $SU(2)$ Yang-Mills theory. Nowadays it is well established by lattice studies, that the confinement-deconfinement transition[2] at $\mu = 0$ happens around $T_c \simeq 155$ MeV [12, 13].

Creating strongly interacting matter under such extreme conditions, meaning very high temperatures (and densities), was and still is experimentally very challenging. It can be achieved in so-called ultra-relativistic heavy ion collisions, which by now have a long and successful history of creating QCD matter at ever higher center of mass energies. The earliest experiments of this kind were performed at the Lawrence Berkeley National Laboratory (LBNL) at Berkeley and at the Joint Institute for Nuclear Research (JINR) in Dubna, in the 1970s. Experiments at low baryon chemical potentials and temperatures large enough to probe the transition between the quark-gluon plasma and the hadronic phase are performed at the Relativistic Heavy Ion Collider (RHIC) at Brookhaven National Laboratory (BNL) and at the Large Hadron Collider (LHC) at CERN in Geneva. Under these conditions matter is produced with approximately the same number of particles and antiparticles, making this region highly relevant to study the early universe. Considering lower temperatures, the system eventually starts to hadronize, which can be described with the statistical hadronization model [14]. Comparison with LHC data gives a transition temperature of $T_c \simeq 160$ MeV [15], which is in very good agreement with lattice predictions from above. Another experimental signature of

[2] To be precise at $\mu = 0$ the confinement-deconfinement transition is an analytic crossover, not a phase transition in the usual sense.

the onset of deconfinement is the suppression of heavy quarkonia, first and foremost J/Ψ suppression [16, 17].

But the confinement-deconfinement transition is not the only expected transition for high temperatures. Also the spontaneously broken chiral symmetry gets restored if one reaches sufficiently large temperatures. Chiral symmetry is a global flavor symmetry of massless QCD, which is approximately realized in the light quark sector of QCD. It is understood to be spontaneously broken in the hadronic phase, which for example manifests itself in the finite mass splitting of chiral partners, which would not exist if chiral symmetry was restored. Good examples for chiral partners showing a finite mass splitting are the mesons (σ, π), as well as ρ and a_1. But there are also strong indications for the nucleons themselves having chiral partners. For the (p, n) isodoublet with $m_{(p/n)} = 939$ MeV usually the much heavier $N(1535)$ is assumed to be the chiral partner. Vector mesons give a direct link between partial restoration of spontaneously broken chiral symmetry and dilepton spectra [18–20], which are accessible in ultra-relativistic heavy ion collisions. In-medium modifications of the vector mesons, in particular the ρ meson, which couples directly to a pair of dileptons, have a significant impact on the dilepton production. Dileptons are a very well-suited probe for the evolution of a heavy ion collision, since they have a very low cross section with strongly interacting matter, thus leave the fireball with negligible final-state interaction. Signals of chiral symmetry restoration have indeed been observed in invariant-mass spectra of vector mesons by the STAR collaboration RHIC as well as at the CERN-SPS [21–23].

Lattice QCD calculations found that the chiral transition at zero baryon chemical potential is also an analytic crossover and the critical temperature coincides with the confinement-deconfinement transition [24–27]. Concerning the finite density regime of the QCD phase diagram the infamous sign-problem of lattice QCD makes lattice calculations in this region unfeasible, or at least restricts them to small $\frac{\mu}{T}$.

Fortunately there are other methods at hand that are not restricted to vanishing densities, which show strong indications for a rich structure of the QCD phase diagram at finite densities. Those are helpful for getting a better understanding of the conjectured phase structure at finite densities in Fig. 1.2. Calculations in the Nambu−Jona-Lasinio model (NJL model) show that the continuous chiral phase transition at $\mu = 0$ becomes a first order phase transition for finite chemical potential which ends in a critical point [28–30]. Similar results are found in beyond mean-field studies of the quark-meson model [31]. These models share the chiral properties of QCD but are much simpler to solve. They have also been extended to incorporate confining aspects by including Polyakov loop dynamics, leading to the PNJL model [32–34] and the Polyakov quark-meson model [35, 36]. Considering spatially modulated chiral condensates $\langle\bar{\psi}\psi\rangle$ allows to study possible inhomogeneous phases of strongly interacting matter within these models [37–40].

A well established functional approach in QCD are Dyson-Schwinger equations (DSEs) [41–43]. DSEs are quantum equations of motion, which lead to an infinite tower of coupled integral equations relating the correlators of a theory to each other, see [44–48] for QCD reviews. DSEs are well suited to explore the QCD phase diagram at finite temperatures and chemical potentials [49] and have successfully been applied to both the chiral and the confinement-deconfinement transition [50–53]. Using quenched gluon propagators from the lattice as an input DSE calculations

were able to pin down the location of the critical endpoint [53, 54].

Looking at very large chemical potentials in Fig. 1.2 other proposed phases of strongly interacting matter appear, the so-called color super-conducting phases. Cooper pairing of quarks at low temperatures and high densities was first discussed in the 1970s [55, 56] and then regained attention in the 1990s [57, 58]. It was studied using effective models [30] as well as with Dyson-Schwinger equations [59–61].

For intermediate densities and low temperatures QCD shows another phase transition which will be of particular importance for this thesis, the nuclear matter liquid-gas transition. The modeling of nuclear matter has a long history, starting in the 1970s [62–64], we will shed light on this topic in a separate dedicated section, Sec. 3.1.1. The area of intermediate temperatures and very high densities, where baryonic degrees of freedom play a crucial role, will experimentally be studied with the Compressed Baryonic Matter (CBM) [65] experiment at the future Facility for Antiproton and Ion Research (FAIR) in Darmstadt.

Coming now to the functional method we will predominantly use throughout this thesis, the Functional Renormalization Group (FRG). Pioneered by Wetterich in 1993 [66], it has since been applied to a variety of problems from quantum and statistical physics, QCD at finite temperature and chemical potential in particular, see [67–70] for QCD related reviews. General studies of QCD at finite density [71] or the general phase structure [72] were performed within the FRG as well as effective models for low energy QCD like the quark-meson [73, 74] and the Polyakov quark-meson model [35, 36]. Also models for QCD-like theories like the quark-meson-diquark model for two-color QCD [75] and its Polyakov extended version, the Polyakov-quark-meson-diquark model [76] were successfully studied and tested against respective lattice simulations without a sign problem. Furthermore, also QCD with isospin chemical potential has been studied within a quark-meson model [77].

Another application is the modelling of nuclear matter, that can for example be considered within a chiral baryon-meson model (chiral Walecka model) which in recent years has been proven to be very useful for the investigation of nuclear and neutron matter at low temperatures. This has been done both in mean-field approximation [78] and beyond mean-field using the FRG [79–81]. A different effective model to study nuclear matter is the parity-doublet model, which we have used in this thesis. The parity-doublet model allows for modelling the liquid-gas transition of nuclear matter as well as chiral symmetry restoration in the high baryon density phase, which has been done within an extended mean-field approximation as well as with full RG fluctuations [82].

Another interesting topic that got attention in the recent years is the calculation of spectral functions from analytically continued RG flow equations. This has been done for purely mesonic $O(N)$-models [83, 84], as well as within a quark-meson model [84–87], both considering meson spectral functions. In this work we want to present a generalization of this procedure for an application concerning quark spectral functions, see Sec.4.1.

As we have seen in this brief introduction the rich phase structure of the QCD phase diagram in Fig 1.2 is reflected in the variety of theoretical approaches that are needed to describe strongly interacting matter in the different regions of the phase diagram. This complex structure, and consequently diverse needs in terms

of theoretical tools, is what makes the QCD phase diagram and its exploration so interesting from a theorist's point of view. The countless experiments running in many international research facilities further confirm its importance.

This thesis will be organized as follows: We will give an overview over the theoretical framework including a discussion of QCD and its symmetries in Chap.2. This will include a detailed introduction to FRG framework (Sec. 2.3) as well as an introduction to the modelling of nuclear and quark matter, Sec. 3.1 and Sec. 3.2. The models applied in this thesis are mainly the chiral two-flavor quark-meson model as a low energy model for QCD and the parity-doublet (or mirror-model) for the description of nuclear matter. We will present results for quark spectral functions calculated from the FRG and furthermore the quark-meson model in a truncation beyond local potential approximation, in Chap.4. Followed by results for nuclear matter within a parity-doublet model treated with the FRG in Chap.5.

The compilation of this thesis is solely due to the author, still some results were obtained in collaboration with others and are published to a certain extend. The results in Sec. 4.1 have been obtained in collaboration with Ralf-Arno Tripolt and Lorenz von Smekal. Parts of the results in Sec. 5 have been obtained in collaboration with Nils Strodthoff and Lorenz von Smekal and are published in [82].

2

Theoretical Framework

2.1. Quantum Chromodyamics and its Symmetries

We want to give a brief introduction to Quantum Chromodynamics, as the quantum field theory of strongly interacting matter. This introduction is not intended to be a complete introduction to quantum field theory in any sense, for a QFT introduction we kindly refer to the literature [88–90]. We rather want to explain the main features and aspects of QCD and its symmetries as a basis for later discussions.

The QCD Lagrangian

QCD belongs to the class of non-abelian gauge field theories which have a compact Lie group as their gauge group. $SU(N_c)$[3] for example, is such a compact Lie group, where we introduced the so-called number of colors N_c. QCD is the special case with $N_c = 3$, thus gauge group $SU(3)$. The quarks, as the fermion fields of the theory, are represented as N_c-component vectors in color space and are in the fundamental representation of the gauge group. The QCD Lagrangian has to be gauge invariant, which we will explain shortly, and has the form [5, 91]

$$\mathcal{L} = \bar{\psi}(x)\Big(i\gamma_\mu D^\mu - m\Big)\psi(x) - \frac{1}{4}F^{a\mu\nu}F^a_{\mu\nu}, \tag{2.1}$$

where we introduced the covariant derivative

$$D_\mu = \partial_\mu - igA_\mu = \partial_\mu - igA^a_\mu T^a. \tag{2.2}$$

In the covariant derivative the gauge coupling g and the gauge field $A_\mu = A^a_\mu T^a$ appear[4] which lies in the adjoint representation of the gauge group $SU(N_c)$. The

[3] $SU(N)$ is the Lie group of unitary $N \times N$ matrices with determinant equal to 1.

[4] Mathematically speaking, the gauge field serves as a connection, making the covariant derivative transform like $D_\mu \to D'_\mu = \Omega D_\mu \Omega^{-1}$, with $\Omega \in SU(N)$. This transformation is crucial for getting a gauge invariant formulation of the theory.

gauge field represents the gluons of the theory and has $N_c^2 - 1$ components A_μ^a, with the $N_c^2 - 1$ traceless hermitian generators T^a. In the case of QCD these $3^2 - 1 = 8$ traceless hermitian generators are closely related to the well-known Gell-Mann matrices $\lambda^a = \frac{T^a}{2}$.

The field strength tensor for the gauge fields is commonly defined through the commutator of two covariant derivatives

$$F_{\mu\nu} := \frac{i}{g}[D_\mu, D_\nu] = \partial_\mu A_\nu - \partial_\nu A_\mu - ig[A_\mu, A_\nu] \,, \tag{2.3}$$

$$F_{\mu\nu}^a = \partial_\mu A_\nu^a - \partial_\nu A_\mu^a + g f^{abc} A_\mu^b A_\nu^c \,. \tag{2.4}$$

In the second step we have made the color components of the field strength tensor explicit, by using the Lie algebra property

$$[T^a, T^b] = i f^{abc} T^c, \tag{2.5}$$

which is obeyed by the generators and defines the structure constants f^{abc} of the gauge group. Additionally, the generators are usually normalized like

$$\mathrm{tr}\,(T^a T^b) = \frac{1}{2}\delta^{ab} \,. \tag{2.6}$$

The QCD Lagrangian is invariant under local gauge transformation $\Omega(x) \in SU(3)$ of the form

$$\psi(x) \to \Omega(x)\psi(x) \quad , \quad A_\mu \to \Omega(x)\big(A_\mu + \frac{i}{g}\partial_\mu)\Omega^\dagger(x) \,. \tag{2.7}$$

The covariant derivative in the Lagrangian (2.1) is contracted with the gamma matrices, which are defined by the anticommutation relation

$$\{\gamma_\mu, \gamma_\nu\} = 2g_{\mu\nu} \,, \tag{2.8}$$

where $g_{\mu\nu}$ is the metric tensor.

The quark fields have further inner structure than just color, which we have so far suppressed for notational convenience. The quarks are Dirac spinors and come in 6 different so-called flavors. These six flavors are called up (u), down (d), strange (s), charm (c), bottom (b) and top (t). They each differ in their masses, which makes the mass m in Eq. (2.1) a matrix in flavor space. Additionally quarks also carry an electric charge of $-\frac{1}{3}e$ or $\frac{2}{3}e$, where e is the elementary charge of an electron.

Already at this point it is worth pointing out some special features of QCD which mainly come from its non-abelian nature. We can see that the gluon field strength tensor in Eq. (2.4), has an additional term $g f^{abc} A_\mu^b A_\nu^c$ compared to non-abelian theories, as for example QED. This term does not exist for an abelian gauge group, since the structure constants for abelian groups vanish. In the non-abelian case, anyway, this term gives rise to gluonic self interactions, which are a direct consequence of the gluon itself carrying color charge, wheres e.g. the photon in QED does not carry charge itself. This has further implications on the screening of color charges. In QED the electric charge gets screened by vacuum polarization, meaning virtual electron-positron pairs get attracted or repelled depending on their charge,

which partially cancels out the electric field, making the test charge appear smaller. This screening effect becomes smaller the closer you are to the test charge, consequently the effective charge becomes larger with decreasing distance (increasing momenta). The same screening effect also exists in the non-abelian case where the color charge gets partially screened by the virtual quark-antiquark pairs. Since the gluon also carries color charge there is also a similar effect by polarization of virtual gluons. This effect, as it turns out, leads to the opposite effect the so-called color antiscreening. Getting closer to a test color charge, it appears smaller than from large distances. These two competing effects are solely determined by the number of colors N_c and flavors N_f, to figure out whether the net effect is screening or antiscreening we recall the one-loop QCD coupling α_s as calculated by Gross, Wilczek and Politzer [8, 9]

$$\alpha_s(Q^2) = \frac{g^2(Q^2)}{4\pi} = \frac{4\pi}{\left(\frac{11}{3}N_c - \frac{2}{3}N_f\right)\log(\frac{Q^2}{\Lambda^2_{\mathrm{QCD}}})} \,, \tag{2.9}$$

with the QCD scale parameter $\Lambda_{\mathrm{QCD}} \simeq 200$ MeV. For QCD, with $N_c = 3$ and $N_f = 6$, this means the net effect is a color antiscreening leading to QCD being asymptotically free.

Chiral symmetry

Let us consider, for a moment, the QCD Lagrangian Eq. (2.1) in the limit of vanishing quark masses which can be decomposed as

$$\begin{aligned}\mathcal{L}_{m=0} = &\bar{u}_L i\gamma_\mu D^\mu u_L + \bar{u}_R i\gamma_\mu D^\mu u_R \\ &+ \bar{d}_L i\gamma_\mu D^\mu d_L + \bar{d}_R i\gamma_\mu D^\mu d_R \\ &+ \bar{s}_L i\gamma_\mu D^\mu s_L + \bar{s}_R i\gamma_\mu D^\mu s_R - \tfrac{1}{4}F^{a\mu\nu}F^a_{\mu\nu} \,,\end{aligned} \tag{2.10}$$

where we only considered the three lightest quarks (u, d, s) and decomposed the fields in terms of their left- and right-handed contributions

$$\psi_{L/R} = \frac{1}{2}\big(1 \pm \gamma_5\big) \quad , \quad \psi = \psi_L + \psi_R \,. \tag{2.11}$$

This Lagrangian is invariant under global flavor transformations on the left- and right-handed sector, described the by chiral group

$$U_L(N_f) \times U_R(N_f) \,. \tag{2.12}$$

This group can be further decomposed as

$$U_L(N_f) \times U_R(N_f) = U_V(1) \times SU_V(N_f) \times SU_A(N_f) \times U_A(1) \,, \tag{2.13}$$

in terms of vector and axial vector transformations. We will consider these transformations in the limit $N_f = 2$, where only up and down quarks contribute as well as including all three (u, d, s) quarks with $N_f = 3$.

Starting with the subgroup $U_V(N_f)$, this symmetry corresponds to a global transformation of the phases of all fields

$$\psi_L \to e^{-i\theta}\psi_L \quad , \quad \psi_R \to e^{-i\theta}\psi_R \,. \tag{2.14}$$

The conserved charge connected to this symmetry is baryon number, which is actually not only present in the massless QCD Lagrangian, thus serves as a conserved quantum number of strongly interacting matter in general.

Coming to the vector and axial vector transformations $SU_V(N_f)$ and $SU_A(N_f)$

$$\psi \to e^{-i\theta_V^a T^a}\psi \quad , \quad \psi \to \psi e^{-i\theta_A^a \gamma_5 T^a}\psi \, , \tag{2.15}$$

where $\theta_{V/A}^a$ are transformation angles, T^a the generators of flavor $SU(N_f)$ and $\gamma_5 = i\gamma_0\gamma_1\gamma_2\gamma_3$. While both symmetries are only exact in the case of massless QCD, they still serve a useful concept also for massive quarks in the (u, d) and (u, d, s) sector. $SU_V(N_f)$ is still an approximate symmetry of (massive) QCD and is especially well realized for $N_f = 2$ due to the very small mass difference of (u, d) (isospin symmetry). This leads to almost degenerate $SU(N_f)$ multiplets for $N_f = 2$ in particular, albeit larger deviations occur for $N_f = 3$.

The axial vector transformations $SU_A(N_f)$ change parity when acting on a definite parity state. So, if $SU_A(N_f)$ was (like $SU_V(N_f)$) realized as an approximate symmetry the hadronic spectrum of QCD should consist of approximately degenerate chiral partners. Since this (in the vacuum) is not the case, one concludes that the chiral symmetry is spontaneously broken in the vacuum. It is broken by the quark condensate $\langle\bar{\psi}\psi\rangle$ which breaks $SU_A(N_f)$ and serves as an order parameter for the spontaneously broken chiral symmetry. More evidence for spontaneously broken chiral symmetry is the comparatively low pion mass. The Goldstone theorem leads to the appearance of massless particles in the spectrum if a continuous symmetry gets spontaneously broken. One such Nambu-Goldstone boson appears for each generator of the symmetry that gets broken. We thus identify the three pions (in the case of $N_f = 2$) with the Nambu-Goldstone bosons of spontaneously broken chiral symmetry. To be more precise the pions are pseudo-Nambu-Goldstone bosons, since chiral symmetry is not exactly realized for finite m_u and m_d, which leads to small but finite masses of the pions. In the $N_f = 3$ case the corresponding pseudo-Nambu-Goldstone bosons appear in the pseudoscalar meson octet, which besides the pions (π_0, π_+, π_-) consists of the four kaons $(K_0, \bar{K}_0, K_+, K_-)$ and the η.

Coming to the axial $U_A(1)$

$$\psi \to e^{-i\theta\gamma_5}\psi \, , \tag{2.16}$$

which is realized by the QCD Lagrangian on a classical level. It is broken on the quantum level (axial anomaly) [92] which is best reflected by the large η' mass. If the η' was the pseudo-Nambu-Goldstone boson of a spontaneously broken symmetry it would have to be much lighter.

Confinement

In the opposite limit of the QCD Lagrangian in Eq. (2.1), the limit of infinitely heavy quarks, the matter part of the Lagrangian decouples and one is left with pure gauge part of the theory. This gives the Lagrangian of pure Yang-Mills theory

$$\mathcal{L}_{\mathrm{YM}} = -\frac{1}{4}F^{a\mu\nu}F^a_{\mu\nu}. \tag{2.17}$$

This Lagrangian, like the full QCD Lagrangian itself, is invariant under gauge transformation of the form (2.7). A particularly simple gauge transformation is given by [93]

$$\Omega_c = e^{i\theta_n} 1 \ , \ \theta_n = \frac{2\pi n}{N_c}. \tag{2.18}$$

This is just the multiplication with a constant phase, where $\theta_n = \frac{2\pi n}{N_c}$ follows from the condition $\det \Omega = 1$ and the index $n = 0, \ldots, N_c - 1$. This defines the center $Z(N_c)$ of $SU(N_c)$.

Let us now consider center transformations as topologically non-trivial gauge transformations, which are periodic in the time direction up to a center element

$$\Omega(\vec{x}, 0) = 1 \quad , \quad \Omega(\vec{x}, \tfrac{1}{T}) = \Omega_c \ . \tag{2.19}$$

Gauge fields are in the adjoint representation of the gauge group and as such are invariant under center transformations. Quarks on the other hand live in the fundamental representation and break center symmetry explicitly.

An order parameter for the breaking of center symmetry is given by the thermal Wilson line

$$L(\vec{x}) = \mathcal{P} \exp \left(ig \int_0^{\frac{1}{T}} \mathrm{d}\tau A_0(\vec{x}, \tau) \right), \tag{2.20}$$

where $\mathcal{P}$ denotes path ordering. The color trace of the Wilson line is the more commonly used Polyakov loop

$$P(\vec{x}) = \frac{1}{N_c} \mathrm{tr}\, L(\vec{x}), \tag{2.21}$$

which is gauge invariant but picks up a phase $e^{i\theta_n}$ under center transformations

$$P \to \Omega_c P \ , \tag{2.22}$$

which also makes it a good order parameter for center symmetry. Furthermore, the expectation value of the Polyakov loop is connected to the free energy needed to separate a static quark anti-quark pair

$$\langle P \rangle \sim e^{-\frac{F_{\bar{\psi}\psi}}{T}} \ . \tag{2.23}$$

We now get the following two cases, that connect center symmetry and confinement.

In the confined phase center symmetry is restored

$$\langle P \rangle = 0 \to F_{\bar{\psi}\psi} = \infty, \tag{2.24}$$

it thus takes infinite energy to separate a quark anti-quark pair.

In the deconfined phase center symmetry is broken

$$\langle P \rangle \neq 0 \to F_{\bar{\psi}\psi} < \infty, \tag{2.25}$$

only finite energy is needed to separate a quark anti-quark pair.

Similar to chiral symmetry which is just an exact symmetry in the limit of vanishing quark masses center symmetry is only exactly realized in pure gauge theory. Finite quark masses break center symmetry explicitly which for example turns the first order confinement-deconfinement transition in $SU(3)$ pure gauge theory into an analytic crossover.

2.2. Non-perturbative Approaches in QCD

Already from the running coupling of QCD in Eq. (2.9), or equivalently in Fig. 1.1, it becomes clear that perturbative approaches, as they are depending on an expansion in the coupling constant, are not feasible for low momentum exchange, i.e. the low energy regime of QCD. Consequently non-perturbative approaches are inevitable to study QCD.

We want to briefly discuss two different non-perturbative methods commonly used, namely lattice QCD and Dyson-Schwinger equations. Afterwards the functional renormalization group will be discussed in more detail in Sec. 2.3, since this is the non-perturbative method we will use throughout this thesis.

2.2.1. Lattice QCD

In lattice QCD the approach to solve path integrals in the theory is to discretize the space-time on a hypercube with finite lattice spacing a. Starting from the Euclidean (Wick-rotated) partition function

$$Z = \int \mathcal{D}A\mathcal{D}\psi\mathcal{D}\bar{\psi}e^{-S_E[A,\psi,\bar{\psi}]} \,. \tag{2.26}$$

The partition function is used to calculate expectation values of observables

$$\langle\mathcal{O}\rangle = \frac{1}{Z}\int \mathcal{D}A\mathcal{D}\psi\mathcal{D}\bar{\psi}\mathcal{O}e^{-S_E[A,\psi,\bar{\psi}]} \,, \tag{2.27}$$

where we used the Euclidean QCD action

$$S_E[A,\psi,\bar{\psi}] = \int \mathrm{d}^4x\Big(\bar{\psi}\big(\gamma_\mu D_\mu + m\big)\psi + \frac{1}{4}F^a_{\mu\nu}F^a_{\mu\nu}\Big). \tag{2.28}$$

By introducing a finite space-time lattice with lattice spacing a, the in principle infinite dimensional path integrals reduce to

$$\langle\mathcal{O}\rangle = \frac{1}{Z}\int [\mathrm{d}U][\mathrm{d}\psi][\mathrm{d}\bar{\psi}]\mathcal{O}e^{-S[U,\psi,\bar{\psi}]} \,, \tag{2.29}$$

with $[\mathrm{d}\psi] = \prod_{x\in\Lambda}\mathrm{d}\psi(x)$ and $[\mathrm{d}U] = \prod_{x\in\Lambda}\prod_\mu \mathrm{d}U_\mu(x)$. This is still a very high dimensional integral which can be solved using numerical Monte-Carlo integration methods. The variable U used in Eq. (2.29) is a so-called link variable, which are usually used to formulate gauge theories on the lattice. They are the lattice discretized version of a continuum parallel transporter and are given by

$$U_\mu(x) = e^{iaA_\mu(x)} \,. \tag{2.30}$$

This connects the link-variables, living in between lattice sites, to the gauge field A_μ. In fact, the link variables play the role of the gauge field in lattice formulations of gauge theories. We still have to specify the lattice action $S[U,\psi,\bar{\psi}]$, which for the sake of brevity, we will briefly discuss for the gauge part of the lattice action only.

Using link variables $U_\mu(x)$ it is possible to construct closed loops on the lattice, which consist of products of links. Color traces of those closed loops are gauge invariant and the smallest closed loop, the so-called plaquette

$$P_{\mu\nu}(x) = U_\mu(x)U_\nu(x+\hat{\mu})U_\mu^\dagger(x+\hat{\nu})U_\nu^\dagger(x) \ , \tag{2.31}$$

is used to define the Wilson plaquette action

$$S_W = -\frac{\beta}{N_c}\sum_{x,\mu<\nu} \mathrm{Re}\,\mathrm{tr}\, P_{\mu\nu}(x). \tag{2.32}$$

Where $\hat{\mu}$ is a unit vector in μ direction and the $\beta = \frac{2N_c}{g^2}$ is the lattice coupling. This action indeed shows the right continuum limit

$$\lim_{a\to 0} S_W = \int \mathrm{d}^4x F^a_{\mu\nu}F^a_{\mu\nu}. \tag{2.33}$$

The fermionic part of the action can also be discretized on the lattice leading for example to the introduction of Wilson fermions. There are many different possibilities of how to discretize fermions on the lattice, which each result in a different lattice Dirac operator $D(U)$.

The sign problem

Taking another look at the discretized partition function, it is possible to integrate out the fermion part, since it is quadratic in the fields

$$Z = \int [\mathrm{d}U][\mathrm{d}\psi][\mathrm{d}\bar{\psi}] e^{-S_W[U]-\bar{\psi}D(U)\psi} = \int [\mathrm{d}U] \det D(U) e^{-S_W[U]} \ , \tag{2.34}$$

which leads to the introduction of the fermion determinant $\det D(U)$. In the numerical Monte-Carlo calculations the fermion determinant is used as a probability weight and consequently is required to be real and positive. In many cases the Dirac operator, of the given discretization, fulfills a condition called γ_5-hermiticity

$$\gamma_5 D \gamma_5 = D^\dagger \ , \tag{2.35}$$

which ensures that the determinant is real. Furthermore including two degenerate quark flavor leads to $\det(D)^2 > 0$. Being real and positive this can be used as a probability weight. Unfortunately γ_5-hermiticity is lost once one includes chemical potential in the system

$$\gamma_5 D(\mu)\gamma_5 = D(-\mu)^\dagger \ . \tag{2.36}$$

The fermion determinant is not necessarily real anymore hence an interpretation as a probability weight no longer possible. This is the famous sign problem of lattice QCD, which prevents us from applying naive Monte-Carlo methods for finite densities and is an interesting issue that lot of attention is drawn to in the QCD community.

Lattice QCD is still the most successful ab initio approach to study strongly interacting matter and in recent years a lot effort has been put into either solving or circumventing the sign problem.

One possibility to avoid the sign problem altogether is to study so-called QCD-like theories. QCD-like theories share main features with QCD, like asymptotic freedom, confinement and chiral symmetry. To do so one usually replaces the gauge group $SU(3)$ with some other gauge group that does not suffer from a sign problem. The most prominent example is two-color QCD with gauge group $SU(2)$, which shows the peculiar feature that its baryons are bosons since they consist of two quarks, rather than three. Still, a lot can be learned from studying two-color QCD and its relation to QCD, which has been done for years and is still done today [94–97]. For example in two-color QCD the confinement-deconfinement transition was found to be of second order, as compared to first order in $SU(3)$ [98]. Another interesting QCD-like theory is G_2-QCD [99, 100], which uses the smallest of the exceptional Lie groups, G_2 as its gauge group. G_2-QCD includes bosonic as well as fermionic baryons, hence gives the possibility of studying a theory without sign problem but with fermionic baryons, like in QCD itself.

Aside QCD-like theories there are many other methods that try to avoid the sign problem in QCD, such include calculations at imaginary chemical potential [25, 101] or through a Taylor expansion for small $\frac{\mu}{T}$ [102, 103]. Recent methods still under development are complex Langevin dynamics, which have recently been successfully used to calculate full QCD at finite μ but still on small lattices [104] or calculations using Monte-Carlo on Lefshetz thimbles [105].

Also strong coupling expansions, either combined with a hopping expansion [106–108] or deriving a graph representation for light quarks [109, 110], have shown to be very useful. As an example, effective Polyakov loop models derived from combined strong coupling and hopping expansion have recently been used to calculate the baryonic matter onset in two-color QCD [111], showing characteristic differences between the diquark condensation for two colors and the liquid-gas transition of QCD.

2.2.2. Dyson-Schwinger equations

The first functional approach we want to discuss briefly are Dyson-Schwinger equations (DSE). The basic idea of the Dyson-Schwinger approach was already developed in the beginning of the 1950s by Dyson and Schwinger [41–43]. Dyson-Schwinger equations are the quantum field analogue of the classical Euler-Lagrange equations, meaning they are the equations of motion for the Green's functions of a given quantum field theory. Consequently, solving the full set of DSEs is equivalent to solving the theory.

Starting from the generating functional of a given theory

$$Z[J] = \int \mathcal{D}\phi e^{-\int_x (\mathcal{L}(\phi) - J(x)\phi(x))}, \tag{2.37}$$

the Dyson-Schwinger equations can be derived by making use of the fact that the

integral over a total derivative vanishes. Which in functional form reads

$$0 = \int \mathcal{D}\phi \frac{\delta}{\delta\phi} e^{-\int_x (\mathcal{L}(\phi) - J(x)\phi(x))} , \tag{2.38}$$

$$= \int \mathcal{D}\phi \Big(- \frac{\delta S(\phi)}{\delta\phi(y)} + J(y) \Big) e^{-\int_x (\mathcal{L}(\phi) - J(x)\phi(x))} , \tag{2.39}$$

$$= \Big(- \frac{\delta S}{\delta\phi(y)} \Big[\frac{\delta}{\delta J} \Big] + J(y) \Big) Z[J] , \tag{2.40}$$

where in the second step we used the functional generalization of $\int_x f(x) e^{\alpha x} = f(\frac{\partial}{\partial_\alpha}) \int_x e^{\alpha x}$. Eq. (2.40) can in principle be expanded around $J = 0$ to get the full set of Dyson-Schwinger equations.

In practice one is often more interested in the one-particle irreducible (1PI) Green's functions given by the full inverse propagators and n-point vertices. To include these one starts with the 1PI effective action

$$\Gamma[\Phi] = \ln[Z] - \int_x J(x)\Phi(x) , \tag{2.41}$$

where we used the classical field $\Phi = \langle\phi\rangle$. Following the same steps as above for $\Gamma[\Phi]$ one ends up with the Dyson-Schwinger equation for the 1PI effective action

$$\frac{\delta\Gamma[\Phi]}{\delta\Phi} = \frac{\delta S[\phi]}{\delta\phi}\Big|_{\phi\to\Phi + D\frac{\partial}{\partial\Phi}} , \tag{2.42}$$

from which the DSEs for any n-point function can be derived by functional differentiation[5]. Either way, for QCD one arrives for example at the DSE for the inverse quark propagator which is shown in diagrammatic form in Fig. 2.1.

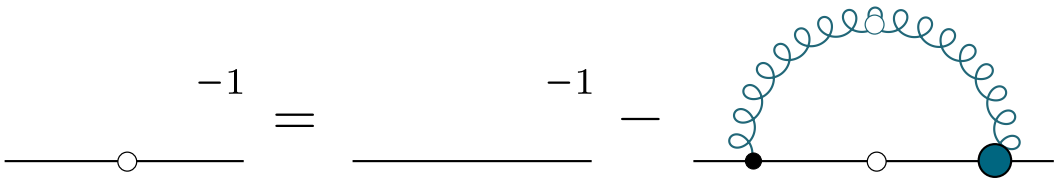

Figure 2.1.: Diagrammatic representation of the DSE for the full inverse quark propagator. Black solid lines correspond to quark propagators, wiggly blue lines to gluon propagators. White/blue circles indicate full propagators/vertices, whereas the black dot is a bare quark-gluon vertex.

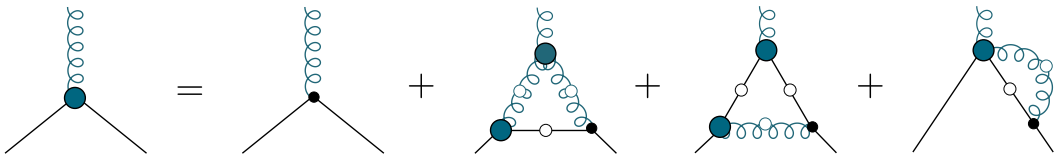

Figure 2.2.: Diagrammatic representation of the DSE for the quark gluon vertex.

[5] Precisely speaking, by functional differentiation followed by setting all sources to zero.

In Fig. 2.1 it can be seen that on the right-hand side of the equation not only the bare inverse propagator appears but in the loop also the full inverse propagator again. This means solving this DSE one has to apply a self-consistent iteration procedure. Furthermore, in the loop in Fig. 2.1 also the full quark-gluon vertex and the full gluon propagator appear, which both fulfill their own DSEs. The corresponding DSE for the quark-gluon vertex is shown in Fig. 2.2, involving even higher fully dressed n-point vertices, which yet again fulfill separate DSEs. This already shows that in general the Dyson-Schwinger approach leads to an infinite tower of coupled equations for all n-point functions, which can rarely be solved in their entirety. Consequently, one has to truncate the infinite tower of coupled equations to end up with a closed system of equations. This can be done in a systematic way by neglecting higher n-point functions starting from a certain order. By taking more and more fully dressed n-point vertices into account this approximation can be systematically improved, which has been successfully done for QCD in the recent years [112–119].

2.3. The Functional Renormalization Group

In 1966 Kadanoff first introduced the renormalization group in the context of block-spin transformations in condensed matter physics [120]. To get an idea of the utilization of the renormalization group one best looks at a system near criticality. Going towards a critical point correlation lengths typically become large and eventually diverge at the critical point, which basically means that fluctuations at all length scales become relevant, making a non-perturbative treatment inevitable.

Critical behavior and universality

This leads us to an interesting finding in statistical physics, namely that completely different systems (considering their microscopic degrees of freedom) can show the same behavior when going towards a phase transition. This phenomenon is called universality. At this point let us briefly discuss how we distinguish different kinds of phase transitions, applying a more modern classification which goes slightly beyond the Ehrenfest classification[6] of phase transitions. We distinguish between first-order phase transitions, which are all phase transition involving some kind of latent heat, for example transitions of the liquid-gas kind. Secondly continuous phase transitions, or second-order phase transitions which show diverging correlation lengths and power-law decays of correlation functions. Near such a continuous phase transition the thermodynamics of a system become independent of their microscopic structure, which makes it possible to group microscopically very different theories into classes with the same behavior at criticality. These universality classes only depend on a small number of parameters like the space-time dimensions, number of spin-like degrees of freedom and on the underlying symmetries [121]. They are characterized by critical exponents describing the scaling relations of observables which typically look like

$$\xi \sim \left(\frac{T - T_c}{T_c}\right)^{-\nu} \quad , \quad \langle \psi(0)\psi(x)\rangle \sim |x|^{2-d-\eta} \, , \tag{2.43}$$

for the correlation length ξ and the two-point correlator $\langle \psi(0)\psi(x)\rangle$, where T_c is the critical temperature and d the number of space-time dimensions. It is worth noting that such scaling relations are intrinsically non-perturbative in their nature, and as such are not accessible through perturbative calculations.

Coming back to Kadanoff's idea, which was not to consider fluctuations at at all scales at once, but rather looking at finite intervals of fluctuations scale by scale. Employing the principle that fluctuations at a certain scale are only coupled locally makes it possible to deal with fluctuations sequentially from small length scales to large ones. This can also be understood as successively integrating out fluctuations at a certain scale, thus effectively reducing the degrees of freedom of the underlying system.

Wilson then applied this principle idea to the path integral formulation of a quantum field theory (QFT), leading to the Wilsonian formulation of the renormalization group [122, 123]. The starting point is the bare (microscopical) action of

[6] The Ehrenfest classification of thermodynamic phase transitions labels phase transitions by the lowest derivative of the free energy showing a discontinuity.

a theory in momentum space at some UV cutoff Λ. We can now integrate over a momentum shell $\frac{\Lambda}{b} \leq q \leq \Lambda$ (with $b > 1$), followed by a rescaling of the momenta $q \to q' = bq$ and the fields $\phi' = \lambda(b)\phi$ in a way that we recover the same action as before but now at a new momentum scale $\frac{\Lambda}{b}$ with different couplings. Such a RG step basically maps the old couplings at the UV scale Λ to a new set of effective couplings at a scale $\frac{\Lambda}{b}$. Repeating these steps for infinitesimally small momentum shells until we reach the IR leads to a trajectory in theory space, that starts with a bare action in the UV Γ_Λ and by integrating out degrees of freedom momentum shell by momentum shell we end up with a macroscopic action Γ in the IR. This action Γ has physics at all scales encoded in itself, showing that the renormalization group[7] is a very effective tool to bridge microscopic physics in the UV with macroscopic physics in the IR.

It is a quintessential feature of strongly interacting quantum field theories that their microscopic degrees of freedom may differ drastically from their macroscopic ones. For example for QCD the respective microscopic degrees of freedom are quarks and gluons whereas the macroscopic ones are mesons and baryons. This makes a methods like the renormalization group highly relevant to study such systems.

The Functional Renormalization Group

The so-called functional renormalization group (FRG) is a very effective realization of Wilson's idea of momentum shell integration and was first introduced by Christof Wetterich in 1993 [66]. The central object in the FRG is the scale dependent effective average action Γ_k, where k is the RG scale, an effective IR cutoff above which all fluctuations have already been integrated out. Γ_k is an interpolating functional functional, in the sense that at the UV scale $k = \Lambda$ it corresponds to the classical action S_{bare} of the theory, where no fluctuations are included. For $k \to 0$ on the other hand the effective average action approaches the full quantum action Γ.

$$\begin{aligned} \Gamma_{k\to\Lambda} &= S_{bare} \\ \Gamma_{k\to 0} &= \Gamma \end{aligned} \tag{2.44}$$

This shows again how the functional RG bridges the gap between short and long range physics. The functional differential equation governing the evolution of the effective average action with the RG scale k is the so-called Wetterich equation, which we will discuss shortly. The functional RG has been successfully applied to a variety of problems in quantum and statistical physics. The applications range from ultracold Fermi gases [124, 125] to condensed matter physics [126] and from quantum gravity [127–129] to QCD [67–70, 73, 75, 76, 130–132].

The effective average action Γ_k

The central objects in all FRG calculations is the scale dependent effective average action Γ_k which is a generalization of the generating functional for one-particle

[7] The renormalization group is not a group in the mathematical sense, since a RG step is not reversible. Once a momentum shell is integrated the microscopical information at this scale is not accessible anymore, but encoded in $\Gamma_{\frac{\Lambda}{b}}$.

irreducible (1PI)[8] correlators. It is defined by introducing a regulator function $R_k(q)$ which acts as a scale dependent mass term suppressing fluctuations at momenta smaller than the RG scale k. The IR regulated generating functional is introduced as

$$Z_k[J] = \mathrm{e}^{W_k[J]} = \int \mathcal{D}\varphi \mathrm{e}^{-S[\varphi]-\Delta S_k[\varphi]+\int J^T\varphi}, \tag{2.45}$$

which is the IR regulated generalization of the usual generating functional, cf. Eq.(B.2). The regulator function $R_k(q)$ enters in the scale dependent regulator functional defined by

$$\Delta S_k[\varphi] = \frac{1}{2}\int \frac{\mathrm{d}^4q}{(2\pi)^4}\varphi(-q)R_k(q)\varphi(q). \tag{2.46}$$

Here one can clearly see that the regulator function $R_k(q)$ acts as a scale dependent mass term, since the regulator functional is quadratic in the fields. The regulated Schwinger functional as can be seen from Eq. 2.45 is given by

$$W_k[J] = \ln(Z_k[J]), \tag{2.47}$$

and is the generating functional of connected correlators. It is closely connected to the effective average action through a regulator modified Legendre transform

$$\Gamma_k[\phi] = \sup_J \left(\int J\phi - W_k[J] \right) - \Delta S_k[\phi]. \tag{2.48}$$

Where the sup singles out a source J for which the supremum is reached. At this source $J = J_{\mathrm{sup}}$ the field ϕ corresponds to the expectation value of φ:

$$\phi(x) = \frac{\delta W_k[J]}{\delta J(x)} = \langle\varphi(x)\rangle_J. \tag{2.49}$$

Having now given the definition of the effective average action we should check whether it has the right limits, see Eqs. (2.44). Doing so it turns out we have to demand certain restrictions considering the choice of the regulator $R_k(q)$ [69]. Making sure Γ_k approaches the classical action S_{bare} in UV we have to demand

$$R_k(q) \to \infty \quad \text{for} \quad k \to \Lambda, \tag{2.50}$$

which guarantees that the path integral in this limit is dominated by the classical solution, giving $\Gamma_{k\to\Lambda} \to S_{\mathrm{bare}}$.

Another requirement is

$$R_k(q) = 0 \quad \text{for} \quad \frac{k^2}{q^2} \to 0, \tag{2.51}$$

which ensures that Γ_k has the proper IR limit. For vanishing $R_k(q)$ one can see from Eq. 2.48, that the effective average action approaches the usual definition of

[8] 1PI diagrams are those which cannot be separated by cutting one internal line.

the effective action Γ, cf. Eq. B.5, consequently $\Gamma_k \to \Gamma$. Thus the full quantum effective action is recovered. Finally we demand

$$R_k(q) > 0 \quad \text{for} \quad \frac{q^2}{k^2} \to 0, \tag{2.52}$$

which implements a scale dependent mass. If we for example take $R_k(q) \sim k^2$ all momentum modes with momenta $q^2 < k^2$ get suppressed while modes above the RG scale k remain unchanged. Successively lowering the scale k we end up with an effective action in the IR that includes all fluctuations. Apart from these restrictions one is free in choosing the regulator functions.

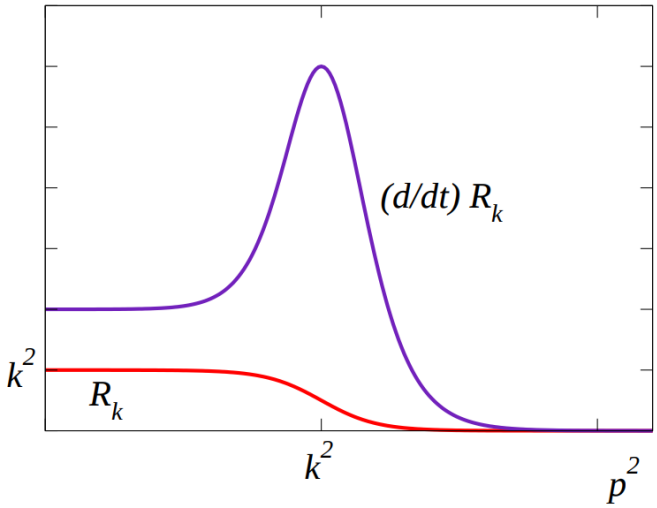

Figure 2.3.: Illustrated is the shape of a regulator function $R_k(q)$ together with its derivative $\partial_t R_k(q) = k\partial_k R_k(q)$. The regulator itself serves as a mass term for momenta $q^2 < k^2$, whereas the form of the derivative implements the momentum shell integration around the scale k. Figure taken from [69]

In Fig. 2.3 a typical regulator function is shown together with its derivative $\partial_k R_k(q)$. The form of the regulator function shows how IR regularization is achieved, by serving as a mass term $m^2 \sim k^2$. We note that the integration of momentum modes around the scale k is actually governed by the derivative of the regulator, not the regulator itself, to be precise. The regulator derivative is peaked around $q^2 \sim k^2$ thus implementing Wilsons's idea of momentum shell integration.

The Wetterich Equation

We are now going to derive Wetterich equation [66] which describes the evolution of the effective average action Γ_k with the RG scale k. In a first step we will take a scale derivative of Γ_k at $J = J_{\text{sup}}$ in Eq. (2.48), which gives

$$\partial_k \Gamma_k[\phi] = -\partial_k W_k[J] - \partial_k \Delta S_k[\phi] \, . \tag{2.53}$$

We can do the same for the regulated Schwinger functional in Eq. (2.47)

$$\begin{aligned}\partial_k W_k[J] &= \partial_k \ln Z_k[J] \\ &= \frac{1}{Z_k[J]} \int \mathcal{D}\varphi\big(- \partial_k \Delta S_k[\varphi]\big) \mathrm{e}^{-S[\varphi]-\Delta S_k[\varphi]+\int J^T\varphi},\end{aligned} \tag{2.54}$$

where the only scale dependence comes from the regulator functional only

$$\partial_k \Delta S_k[\varphi] = \frac{1}{2}\int \frac{\mathrm{d}^4 q}{(2\pi)^4}\varphi(-q)\partial_k R_k(q)\varphi(q). \tag{2.55}$$

Using the definition of the full propagator

$$\langle\varphi\varphi\rangle(q) = \left(\frac{\delta^2 W_k[J]}{\delta J \delta J}\right)(q) + \langle\varphi\rangle\langle\varphi\rangle(q), \tag{2.56}$$

Eq. (2.54) can be rearranged to give

$$\partial_k W_k[J] = -\frac{1}{2}\int \frac{\mathrm{d}^4 q}{(2\pi)^4}\left(\partial_k R_k \frac{\delta^2 W_k[J]}{\delta J \delta J}\right) - \partial_k \Delta S_k[\phi]. \tag{2.57}$$

Going back to Eq. 2.49, we can perform another functional derivative which gives

$$\frac{\delta^2 W_k[J]}{\delta J(x)\delta J(y)} = \frac{\delta\phi(x)}{\delta J(y)}. \tag{2.58}$$

Furthermore, by taking one functional derivative (with respect to $\phi(x)$) of the effective average action in Eq. (2.48), one can see that the also quantum equation of motion receives a regulator modification, giving

$$\frac{\delta\Gamma_k[\phi]}{\delta\phi(x)} = J(x) - R_k\phi(x). \tag{2.59}$$

This is the regulated generalization of the quantum equation of motion, which governs the dynamics of the field $\phi(x)$. A second functional derivative yields

$$\frac{\delta^2\Gamma_k[\phi]}{\delta\phi(x)\delta\phi(y)} = \frac{J(x)}{\delta\phi(y)} - R_k(x,y). \tag{2.60}$$

Eq. (2.58) and Eq.(2.59) can now be combined using the following trick

$$\begin{aligned}\frac{\delta J(x)}{\delta J(y)} = \delta(x-y) &= \int \mathrm{d}^4 z \frac{\delta J(x)}{\delta\phi(z)}\frac{\delta\phi(z)}{\delta J(y)} \\ &= \int \mathrm{d}^4 z \left(\frac{\delta^2\Gamma_k[\phi]}{\delta\phi\delta\phi} + R_k\right)(x,z)\left(\frac{\delta^2 W_k[J]}{\delta J\delta J}\right)(z,y).\end{aligned} \tag{2.61}$$

This means, that $\Gamma_k^{(2)} + R$ is the inverse regulated propagator of the theory, in a more short-hand notation it reads

$$\left(\Gamma_k^{(2)} + R_k\right)^{-1} = \frac{\delta^2 W_k[J]}{\delta J\delta J}. \tag{2.62}$$

Finally coming back to the scale dependence of Γ_k itself. Right in the beginning of the derivation we found

$$\partial_k \Gamma_k[\phi] = -\partial_k W_k[J] - \partial_k \Delta S_k[\phi], \tag{2.63}$$

where we can now plug in Eq. 2.57 to give

$$\partial_k \Gamma_k[\phi] = \frac{1}{2} \int \frac{\mathrm{d}^4 q}{(2\pi)^4} \left(\partial_k R_k \frac{\delta^2 W_k[J]}{\delta J \delta J} \right), \tag{2.64}$$

and finally plugging in the regulated propagator Eq. 2.62 yields

$$\begin{aligned} \partial_k \Gamma_k &= \frac{1}{2} \int \frac{\mathrm{d}^4 q}{(2\pi)^4} \left(\Gamma_k^{(2)} + R_k \right)^{-1} \partial_k R_k \\ &= \frac{1}{2} \mathrm{Tr} \left[\left(\Gamma_k^{(2)} + R_k \right)^{-1} \partial_k R_k \right]. \end{aligned} \tag{2.65}$$

In the last step we introduced a trace that runs over all internal indices that might occur and also includes an integration over the internal momentum variable. The whole derivation in principle also holds for a field containing bosonic as well as fermionic components

$$\Phi = (\phi, \psi, \bar{\psi}^T),$$

where ϕ stands for a bosonic field and $(\psi, \bar{\psi}^T)$ for fermionic ones. Further internal indices are suppressed but can of course be included. Using this, one finds for the Wetterich equation

$$\partial_k \Gamma_k = \frac{1}{2} \mathrm{STr} \left[\left(\Gamma_k^{(2)} + R_k \right)^{-1} \partial_k R_k \right], \tag{2.66}$$

which can then be split into its bosonic and fermionic contributions

$$\partial_k \Gamma_k = \frac{1}{2} \mathrm{Tr} \left[\left(\Gamma_{k,B}^{(2)} + R_{k,B} \right)^{-1} \partial_k R_{k,B} \right] - \mathrm{Tr} \left[\left(\Gamma_{k,F}^{(2)} + R_{k,F} \right)^{-1} \partial_k R_{k,F} \right]. \tag{2.67}$$

The supertrace (STr) in Eq. 2.66, apart from running over all possible internal indices and including a momentum integration, also gives a minus sign in the fermionic subspace. In Fig. 2.4 we see a diagrammatic representation of the Wetterich equation, where dashed lines stand for bosonic propagators and solid lines for fermionic ones. The blue and grey crossed circles stand for bosonic and fermionic regulator insertions, respectively.

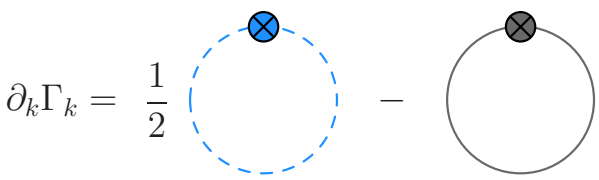

Figure 2.4.: Diagrammatic representation of the Wetterich equation for the effective average action Γ_k

Here one can also see the formal one-loop structure of the Wetterich equation, which should not be confused with perturbative one-loop order, although one can use the Wetterich equation as a starting point for a perturbative 1-loop calculation by replacing $(\Gamma_k^{(2)} + R) \to (S^{(2)} + R)$. Still the Wetterich equation is exact since it has the full field dependent propagator appearing in the loop.

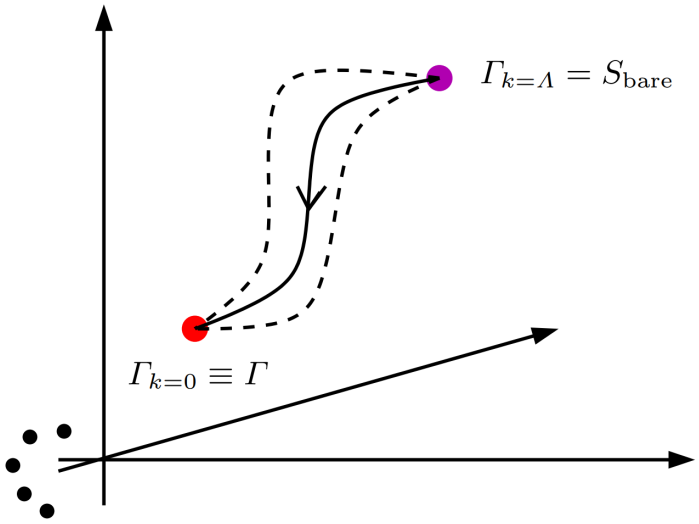

Figure 2.5.: Shown is a sketch of the RG flow in theory space, the space spanned by all possible couplings of a given theory. The different trajectories correspond to different regulator choices. If the regulators are chosen properly, all relevant physical information will still be covered. In this case the UV and IR limit of the different trajectories coincide, giving $\Gamma_{k=\Lambda} = S_{\text{bare}}$ and $\Gamma_{k=0} = \Gamma$. Figure taken from [69].

As we have already mentioned before, the regulator $R_k(q)$ has actually different but intimately related functions. Through conditions (2.50) and (2.51) the proper UV and IR limits are governed. But furthermore, through the regulator derivative appearing in the numerator of Eq. (2.66) and its peaked structure around $q^2 = k^2$ realizes the Wilson's idea of successive momentum shell integration, see also Fig. 2.3. Apart from the conditions (2.50), (2.51) and (2.52) the regulators can be chosen freely. Different regulators may then influence the exact RG trajectory in theory space, the UV and especially the IR limit, will always coincide, which is depicted in Fig. 2.5.

As a last remark, provided the full theory is considered, the solutions to the FRG (in the infrared) in principle are also solutions to the corresponding DSE. The major difference being that DSEs correspond to integrating out fluctuations at all scales at once, whereas the FRG incorporates fluctuations momentum shell by momentum shell.

3

Modelling of Quark and Nuclear Matter

3.1. Nuclear Matter and its Modelling

Through ultra-relativistic heavy ion collisions it is possible to probe QCD matter at finite temperature and baryon density [133, 134]. The region of large baryon densities in the phase diagram is of special interest and due to the notorious sign problem of lattice QCD this region cannot be be investigated with straightforward Monte-Carlo methods. Still, there is evidence for a first-order transition analogous to the liquid-gas transition of nuclear matter studying QCD-like theories. For example G_2-QCD, a QCD-like theory with fermionic baryons, does not show a sign problem and can consequently be used to investigate finite baryon densities. This theory indeed showed such a first-order transition [99, 100].

For the most part, studying the low temperature region of the QCD phase diagram around the nuclear matter liquid-gas transition one is left with effective models. Since effective models have a long and successful history to describe nuclear as well as neutron matter, we want to shed some light on their evolution throughout the years in the following.

3.1.1. History of nuclear matter

In 1974 J. D. Walecka studied nuclear matter by introducing a model that considered a baryon field $\psi(x) = \begin{pmatrix} \psi_p \\ \psi_n \end{pmatrix}$ representing the nucleons as the fermionic degrees of freedom. This baryon field was then coupled to a neutral scalar field $\phi(x)$ and to a vector field V_λ. See [62] for the original work or [135, 136] for more recent reviews.

In Fig. 3.1 we show the Lagrangian used by Walecka, where $F_{\lambda\rho} = \partial_\lambda V_\rho - \partial_\rho V_\lambda$ is the field strength tensor of the vector meson and M, μ, m are the mass parameters

of the respective fields.

$$\mathscr{L} = -\hbar c \left[\bar{\psi}\left(\gamma_\lambda \frac{\partial}{\partial x_\lambda} + M\right)\psi\right] - \frac{c^2}{2}\left[\left(\frac{\partial\phi}{\partial x_\lambda}\right)^2 + \mu^2\phi^2\right] - \frac{1}{4}F_{\lambda\rho}F_{\lambda\rho} - \frac{m^2}{2}V_\lambda V_\lambda + ig_v\bar{\psi}\gamma_\lambda\psi V_\lambda + g_s\bar{\psi}\psi\phi,$$

Figure 3.1.: The Lagrangian introduced by Walecka. A baryon field ψ coupled to a neutral scalar field ϕ as well as to a vector field V_λ. [62].

The couplings g_v and g_s as well as the mass parameters are phenomenological constants that in principle can be determined by experimental observables. This simple Lagrangian corresponds to a phenomenological nuclear potential of the form

$$V(x) \sim \left(g_v^2 \frac{e^{-mr}}{r} - g_s^2 \frac{e^{-\mu r}}{r}\right). \tag{3.1}$$

The coupling to the vector meson thus produces a short range repulsion whereas the scalar meson (for $\mu < m$) renders the potential attractive for large distances, thus realizing the main feature responsible for nuclear matter saturation. This model was solved using a relativistic mean-field approach by setting the scalar and vector fields to their respective uniform expectation values

$$\phi(x) = \langle\phi(x)\rangle = \phi_0 \quad , \quad V_\lambda(x) = \langle V_\lambda(x)\rangle = (V_0, 0, 0, 0) \tag{3.2}$$

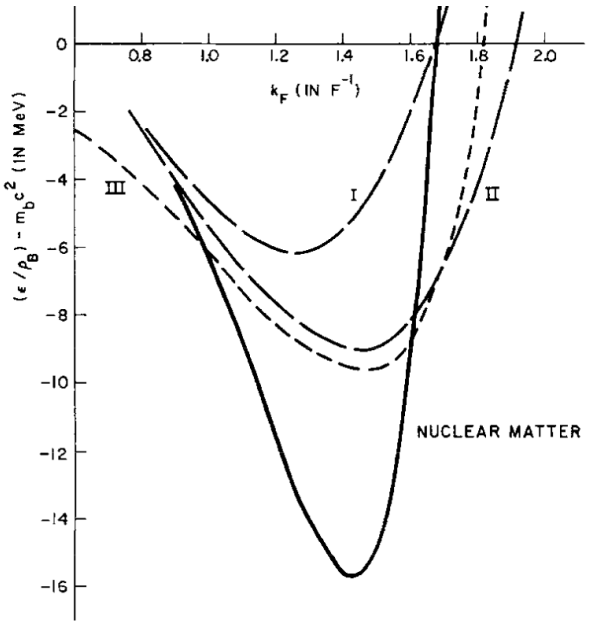

Figure 3.2.: Binding energy per nucleon $E_b = \frac{\epsilon}{\rho_B} - m_b$ as a function of the Fermi momentum. Bound nuclear matter with a binding energy of $E_b \simeq -16$ MeV and an equilibrium Fermi momentum $k_F = 1.42$ fm^{-1} is realized (solid black curve). [62].

Walecka found bound nuclear matter, by adjusting the model parameters to realize nuclear matter binding energy $E_b \simeq -16\,\mathrm{MeV}$ per nucleon as well as saturation density of $n_0 = 0.16\,\mathrm{fm}^{-3}$, as can be seen in Fig. 3.2. The Fermi momentum is directly related to the baryon density [62]

$$\rho_B = \frac{\gamma}{(2\pi)^3}\int_0^{k_F} \mathrm{d}^3k = \frac{\gamma}{6\pi^2}k_F^3 \,, \tag{3.3}$$

where the degeneracy factor $\gamma = 4$ for symmetric nuclear matter and $\gamma = 2$ for neutron matter. Unlike nuclear matter, neutron matter remained unbound in the Walecka model, as it is commonly called nowadays.

In the same year T. D. Lee and G. C. Wick published a work on nuclear matter that incorporated a chirally invariant version of the Walecka model, nowadays usually called a chiral Walecka or linear sigma model [63]. Taking another look at Walecka's Lagrangian in Fig. 3.1, we can observe that the explicit mass term $\sim M\bar{\psi}\psi$ breaks chiral symmetry explicitly. In Lee and Wick's approach on the other hand, they coupled the baryon field $\psi(x) = \begin{pmatrix}\psi_p \\ \psi_n\end{pmatrix}$ to the scalar and pseudoscalar meson fields $(\sigma, \vec{\pi})$ in a chirally invariant way, resulting in a Yukawa-like coupling term of the usual form $g\bar{\psi}(\sigma + i\vec{\pi}\cdot\vec{\tau}\gamma_5)\psi$. Another difference is, that in the chiral Walecka model as originally applied by Lee and Wick, no coupling to a vector meson is included, although it maybe easily included. Their original full Lagrangian is shown in Fig. 3.3.

$$\mathfrak{L} = -\psi^\dagger \gamma_4 \gamma_\mu \frac{\partial}{\partial x_\mu}\psi - g\psi^\dagger\gamma_4[\sigma + i\vec{\pi}\cdot\vec{\tau}\gamma_5]\psi$$

$$-\frac{1}{2}\left[\left(\frac{\partial\sigma}{\partial x_\mu}\right)^2 + \left(\frac{\partial\vec{\pi}}{\partial x_\mu}\right)^2\right] - U_\sigma \,,$$

Figure 3.3.: Lagrangian of the chiral Walecka model used by Lee and Wick [63].

The potential term is of the form [63]

$$U_\sigma = \frac{1}{4}\lambda^2\left(\sigma^2 + \vec{\pi}^2 - \left(\frac{\mu}{\lambda}\right)^2\right)^2 - c\sigma \,, \tag{3.4}$$

where λ, μ and c are parameters. This is the usual form of a mesonic self interaction potential up to fourth order in the fields. Also an explicit chiral symmetry breaking term $c\sigma$ is included. At the expectation value of the meson fields $\sigma = \sigma_0$ and $\vec{\pi} = 0$ the nucleon mass can be related to the uniform expectation value of the sigma meson

$$m_N = g\sigma_0 \,. \tag{3.5}$$

This means, that the nucleon mass is generated solely by the condensation of the sigma field.

When they adjusted the parameters to realize physical nuclear matter density, they found two minimum energy solutions. These two solutions showed practically no potential barrier between each other, which can be seen from Fig. 3.4. In Fig. 3.4 their resulting function $V(\chi)$ is plotted against the rescaled field variable $\chi = \frac{\lambda\sigma}{\mu}$, the black solid curve corresponds to the calculation which realizes nuclear matter density $n = n_0$. The minimum near $\chi = 1$ resembles nuclear matter with an effective nucleon mass of $m_N \sim 940$ MeV. The other minimum, which Lee and Wick called *abnormal*, compares to a nucleon mass which effectively vanishes.

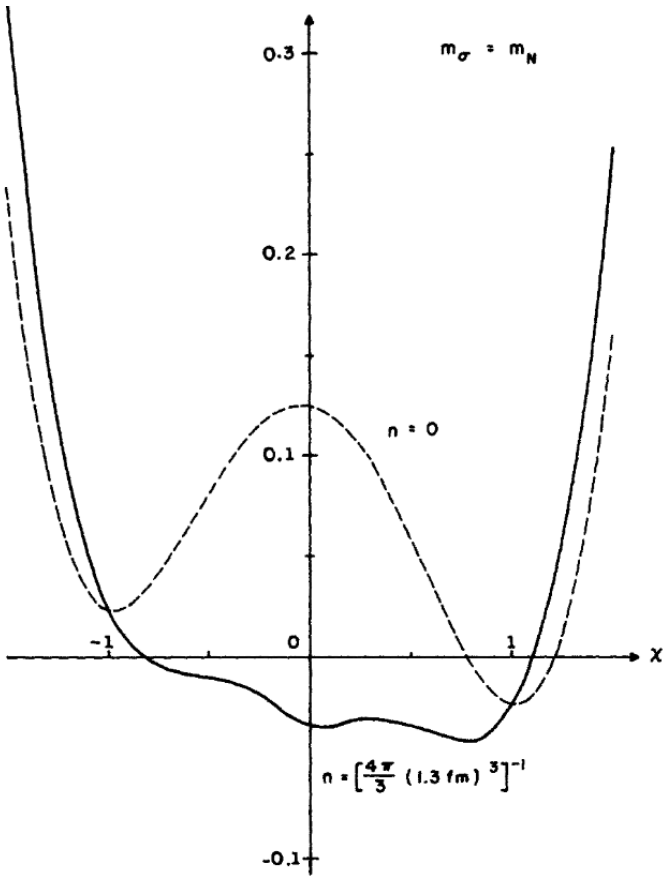

Figure 3.4.: The Resulting function $V(\chi)$, where χ is the rescaled sigma field $\chi = \frac{\lambda\sigma}{\mu}$. The solid black curve corresponds to a solution that realizes physical nuclear matter density. Two minima can be seen, the one near $\chi = 1$ corresponds to a nucleon mass $\sim m_N$. The minimum near $\chi = 0$ is an "abnormal" solution, with a vanishing nucleon mass. [63].

This phenomenologically problematic situation can be made sense of by looking at the problem from the standpoint of chiral symmetry. The difficulties in the zero temperature chiral Walecka model are intimately related to the way the nucleon mass is generated in this model. Already on mean-field level, what Lee and Wick's work basically represents, this can be seen from Eq. 3.5. The predominant contribution to the nucleon mass comes from dynamical chiral symmetry break-

ing, consequently when chiral symmetry gets restored one gets so-called massless Lee-Wick matter, where the baryonic degrees of freedom become massless. This is very similar to quark-meson models, in contrast to quarks anyway, nucleons are not expected to become massless in the chirally restored phase.

Still, using a phenomenological parametrization of the effective potential at vanishing temperature and density as an initial condition, the chiral Walecka model has recently gained renewed interest. With this approach it was possible to successfully investigate both nuclear and neutron matter at small temperatures both in the mean-field approximation [78] and including beyond mean-field fluctuations by means of the functional renormalization group [79–81].

The problem of massless nucleons in the chirally restored phase can very effectively be circumvented by employing parity doubling of baryons, which we will discuss now.

3.1.2. Parity doubling

As a motivation to why parity doubling is an interesting concept it is worthwhile taking a look at hadron spectra as obtained from experiment [137]. Fig. 3.5 shows a collection of hadron masses for the mesons and baryons as they appear in the spectrum of QCD.

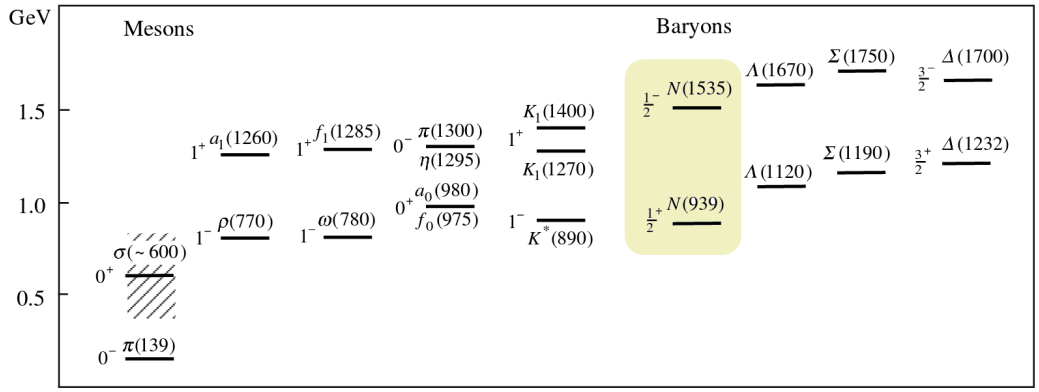

Figure 3.5.: Mesons and baryons with opposite parity as they appear in the QCD spectrum. A mass splitting between positive and negative parity hadrons can be seen. Figure taken from [138].

It can be seen that hadrons with opposite parity appear in pairs that show a clear mass splitting. The question is now, what happens with those parity partners when we move towards chiral restoration. In case of the mesons it is well known for example the chiral partners σ and $\vec{\pi}$ become degenerate in the chirally restored phase. For baryons, anyway, there are two scenarios. The Lee-Wick scenario that results in massless nucleons in the chirally restored phase. But one could also identify a negative parity baryon as the nucleon's chiral partner, the two would then become degenerate in the restored phase. How we include a negative parity partner in a larger representation for both the nucleon and its parity partner and

how they will be related to chiral symmetry, will be discussed shortly. It will, anyway, be somewhat more involved than getting the meson representations.

Following from the quark representation $SU(2)_R \otimes SU(2)_L$ we find in the usual way the corresponding representations for the scalar and pseudoscalar mesons

$$(\sigma, \vec{\pi}) \sim (\bar{q}q, i\bar{q}\gamma_5\vec{\tau}q) \sim (\tfrac{1}{2}, \tfrac{1}{2}) \ , \tag{3.6}$$

and similarly for the vector and axial vector mesons

$$(\rho, a_1) \sim (\bar{q}\gamma^\mu q, i\bar{q}\gamma_5\gamma^\mu\vec{\tau}q) \sim (1,0) \oplus (0,1) \ . \tag{3.7}$$

In the next section we want to give a cohesive explanation of how to describe baryons and their possible mass terms by considering their transformation behavior under chiral transformations. It will be seen, that it is impossible to have a chirally invariant Dirac-like mass term for a single baryon species. Conversely, for two different baryon species it turns out to be possible to have such a mass term without breaking chiral symmetry explicitly. We will follow the discussions in [138], where a more detailed explanation of chiral representations for baryons is given, for a more recent discussion of this topic see, e.g. [139].

Chiral representations for baryons

To get an overview of a baryon's possible representations under $SU(2)_R \times SU(2)_L$ transformations, let us consider the product of three $(\frac{1}{2},0) \oplus (0,\frac{1}{2})$ quark representations. Without any loss of generality one assigns the first label in the product representations (m,n) to an irreducible representation of $SU(2)_R$ and the second to one of $SU(2)_L$, which gives [138],

$$\begin{aligned} &\big((\tfrac{1}{2},0) \oplus (0,\tfrac{1}{2})\big) \otimes \big((\tfrac{1}{2},0) \oplus (0,\tfrac{1}{2})\big) \otimes \big((\tfrac{1}{2},0) \oplus (0,\tfrac{1}{2})\big) \\ &\qquad = 5\,\big(\tfrac{1}{2},0) \oplus (0,\tfrac{1}{2})\big) \oplus 3\,\big((1,\tfrac{1}{2}) \oplus (\tfrac{1}{2},1)\big) \oplus \big((\tfrac{3}{2},0) \oplus (0,\tfrac{3}{2})\big) \ . \end{aligned}$$

The most intuitive choice for the isodoublet of proton and neutron is taking $(\frac{1}{2},0) \oplus (0,\frac{1}{2})$. Thus the same representation as for a pair of up and down quarks is used for the left and right-handed components of the nucleon field $\psi_{l/r} \equiv \frac{1 \mp \gamma_5}{2}\psi$.

If one now not only takes a single baryon species into account but two species ψ_1 and ψ_2, both belonging to a $(\frac{1}{2},0) \oplus (0,\frac{1}{2})$ representation, there are two (and only two) possibilities of how to assign the field labels to their corresponding chiral transformation behavior. This is reflected in the freedom of choosing to assign for example the first label of the first species to $\psi_{1,l}$. The first label of the second species can now either refer to $\psi_{2,l}$ or $\psi_{2,r}$.

The first possibility is the so called *naive* assignment

$$\begin{aligned} &\psi_{1,l} \to \Omega_L\psi_{1,l}, \ \psi_{1,r} \to \Omega_R\psi_{1,r} \ , \\ &\psi_{2,l} \to \Omega_L\psi_{2,l}, \ \psi_{2,r} \to \Omega_R\psi_{2,r} \ . \end{aligned} \tag{3.8}$$

Here the two baryon species transform exactly in the same way.

In contrast the second possibility, referred to as the *mirror* assignment gives

$$\begin{aligned} &\psi_{1,l} \to \Omega_L\psi_{1,l}, \ \psi_{1,r} \to \Omega_R\psi_{1,r} \\ &\psi_{2,r} \to \Omega_L\psi_{2,r}, \ \psi_{2,l} \to \Omega_R\psi_{2,l}. \end{aligned} \tag{3.9}$$

The transformation properties of the second baryon species is interchanged as compared to the first species, hence the name *mirror* assignment. In both cases $\Omega_{R,L} \in SU(2)_{R,L}$.

Taking a look at the generic kinetic term

$$\mathcal{L}_{\text{kin}} = \sum_{i=1,2} \bar{\psi}_i \mathrm{i}\partial\!\!\!/ \psi_i \tag{3.10}$$

it can directly be seen, that this term is invariant under chiral transformations irrespective of which assignment is chosen.

On the other hand a Dirac-like mass term of the form

$$\mathcal{L}_m = -m\bar{\psi}_i\psi_i \tag{3.11}$$

surely breaks chiral symmetry in both assignments, which inevitably leads us to the conclusion that it is not possible to construct an invariant Dirac-mass term with only a single baryon species. If one, however, considers two baryon species in *mirror* assignment it is possible two write down a mass term of the form

$$\begin{aligned} \mathcal{L}_{m,\text{mirror}} =& m_0(\bar{\psi}_2\psi_1 + \bar{\psi}_1\psi_2) \\ =& m_0(\psi_{2r}^\dagger\psi_{1l} + \psi_{1l}^\dagger\psi_{2r} + \psi_{1r}^\dagger\psi_{2l} + \psi_{2l}^\dagger\psi_{1r}) \end{aligned} \tag{3.12}$$

which indeed is invariant under the $SU(N_f)_R \times SU(N_f)_L$, but would still break chiral symmetry in the *naive* assignment.

So the subtle but crucial difference in baryon assignments gives rise to a chirally invariant local mass term which is the main feature of the so parity-doublet or mirror models [140–142].

3.1.3. Lattice evidence for parity doubling

Parity doubling of mesons and baryons is in fact also supported by lattice studies of the hadron spectrum towards chiral symmetry restoration, that have been performed in recent years [143–145]. In these studies the connection to chiral symmetry is made by means of the Banks-Casher relation [146]

$$\langle 0|\bar{\psi}\psi|0\rangle = -\pi\rho(0) \ , \tag{3.13}$$

which relates the vacuum quark condensate to the density of the lowest quasi-zero eigenmodes of the Dirac operator. Making use of this, one can gradually restore chiral symmetry by removing more and more low-lying Dirac modes in valence quark propagators [143]

$$S' = S - \sum_i^k \frac{1}{\mu_i}|v_i\rangle\langle v_i|\gamma_5 \ . \tag{3.14}$$

S is the full quark propagator. The μ_i and v_i are eigenvalues and eigenvectors of the hermitian Dirac operator $\gamma_5 D$. For increasing k more lowest-lying modes are filtered out and one eventually reaches chiral symmetry restoration.

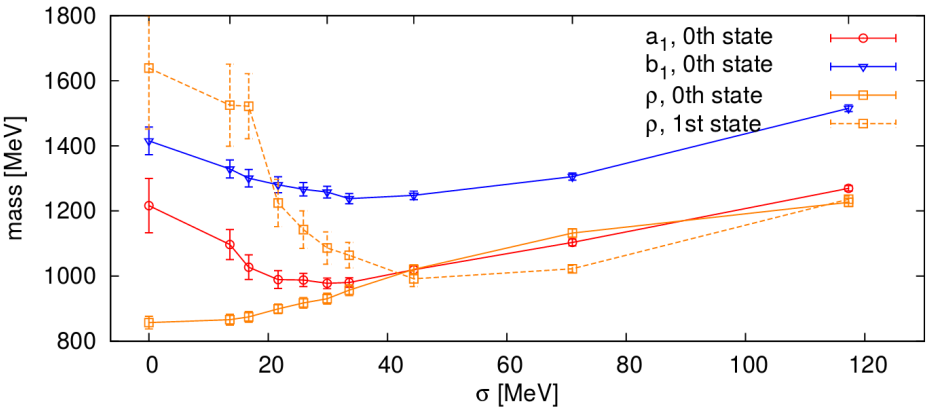

Figure 3.6.: Mass evolution for the isovector mesons, obtained by the described mode filtering. σ is a measure for how many low-lying Dirac modes were filtered out, for larger values of σ one is closer to the chirally restored phase. Figure taken from [143].

In Fig. 3.6 the masses of the isovector mesons are shown as a function of the truncation level, higher values of σ correspond to being closer to the chirally restored phase. For the (ρ, a_1) pair (solid red and orange curve) one can see, that they have a mass splitting in the broken phase but gradually become degenerate with increasing σ.

The analogous plot for the baryon masses is shown in Fig. 3.7. For the (0th state) nucleons (solid red and orange curve) a similar behavior compared to the ρ and a_1 can be observed. The masses of the nucleon and its opposite parity counterpart start with a finite mass splitting, but the masses do not drop to zero, as in the Lee-Wick scenario, if anything the masses slightly increase and become degenerate in the chirally restored phase.

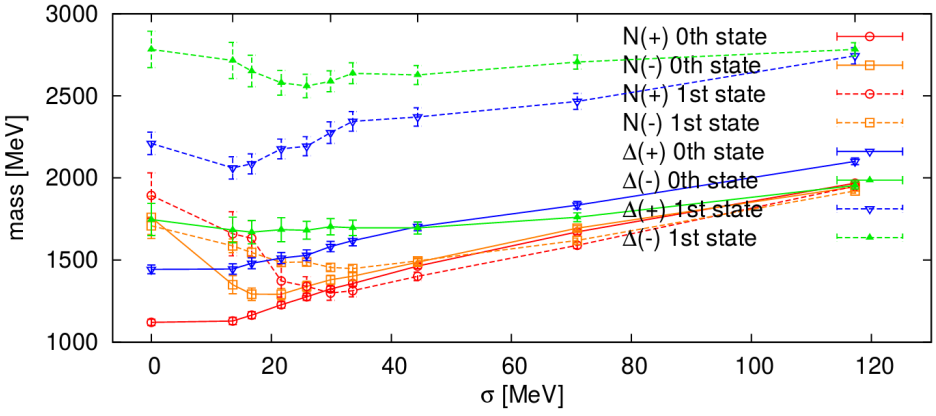

Figure 3.7.: Baryon masses as obtained by the described mode filtering. Again for larger values of σ one is closer to the chirally restored phase. Figure taken from [143].

In conclusion, a model reflecting the fact that the mass of the nucleon stays finite when going towards restored chiral symmetry, which we expect for chemical potentials beyond the liquid-gas transition, has to include the nucleons as well as their parity partners [147, 148]. In the next section we will discuss the model setup of such a parity-doublet model which later on will be used to study the nuclear matter transition together with chiral symmetry restoration in the high baryon density phase.

3.1.4. Construction of the parity-doublet model

The parity-doublet model, in the form that we will use throughout this thesis, consists of two baryon species with mirror-assignment and a chirally invariant mass term of the form described in Eq. (3.12). We just need to make minor changes to get the right phenomenology identifying the two baryon species with the nucleons and their parity partners. Compared to Sec. 3.1.2 we identify $N_1 \equiv \psi_1$ and $N_2 \equiv \gamma_5\psi_2$ with the two nucleon species. This way, N_1 and N_2 have opposite parity and the eigenvalues of the chirally invariant mass matrix in the chirally restored phase are both m_0, as compared to $\pm m_0$ in Eq. (3.12), see [138]. The nucleons and their parity partners are coupled to the scalar and pseudoscalar mesons $\vec{\phi} = (\sigma, \vec{\pi})$ in a $SO(4)$-invariant way. This leads to the following Euclidean Lagrangian, which includes baryon chemical potential μ_B and a vector coupling to the ω-meson

$$\begin{aligned}\mathcal{L} =&\bar{N}_1\big(\partial\!\!\!/ - \mu_B\gamma_0 + h_1(\sigma + \mathrm{i}\gamma_5\vec{\tau}\vec{\pi}) + \mathrm{i}h_v\gamma^\mu\omega_\mu\big)N_1 \\ &+ \bar{N}_2\big(\partial\!\!\!/ - \mu_B\gamma_0 + h_2(\sigma - \mathrm{i}\gamma_5\vec{\tau}\vec{\pi}) + \mathrm{i}h_v\gamma^\mu\omega_\mu\big)N_2 \\ &+ m_0(\bar{N}_1\gamma_5 N_2 - \bar{N}_2\gamma_5 N_1) + \mathcal{L}_{\mathrm{mes}}.\end{aligned} \tag{3.15}$$

We note that the parity N_2 transforms as $N_2 \to e^{-i\theta^a\gamma^5 T^a}N_2$ under axial transformations compared to the nucleon transforms as $N_1 \to e^{i\theta^a\gamma^5 T^a}N_1$. This relative sign in the axial transformations requires also opposite signs in the respective Yukawa couplings to the pion. The vector coupling constant $\mathrm{i}h_v$, which is purely imaginary reflecting the repulsive nature of the included isoscalar vector meson, is equal for both the nucleons and their parity partners. Furthermore the mesonic part of the Lagrangian (3.15) has the following form

$$\mathcal{L}_{\mathrm{mes}} = \frac{1}{2}\partial_\mu\vec{\phi}\partial^\mu\vec{\phi} + \frac{1}{4}F_{\mu\nu}F^{\mu\nu} + U(\phi^2, \omega^2) - c\sigma\,, \tag{3.16}$$

with the field strength tensor of the vector meson $F^{\mu\nu} = \partial^\mu\omega^\nu - \partial^\nu\omega^\mu$. The mesonic potential at the ultraviolet cutoff Λ is of the form

$$U(\phi^2, \omega^2) = -\frac{\mu^2}{2}\phi^2 + \frac{\lambda}{4}\phi^4 + \lambda_6\phi^6 + \frac{m_\omega^2}{2}\omega^2, \tag{3.17}$$

where $\phi^2 = \sigma^2 + \vec{\pi}^2$ and $\mu^2, \lambda, \lambda_6$ are parameters. The explicit breaking term $c\sigma$ lets us includes a non-vanishing mass of the pion as the pseudo Nambu-Goldstone boson of chiral symmetry, giving

$$V_{\mathrm{M}} = U(\phi^2, \omega^2) - c\sigma. \tag{3.18}$$

In the further considerations we will treat the vector meson as a mean-field, which is a reasonable approximation since due to its comparatively large mass $m_\omega = 782$ the contributions from vector meson loops are not expected to be of major importance. The vector meson ω could in principle be included as a fluctuating degree of freedom as well, for instance in the Stueckelberg formalism [149, 150]. The exact way how to include a fluctuating vector meson within the FRG, anyway, is still a topic of current research. This corresponds to evaluating its expectation value on a given solution of the effective potential U_k. The repulsive nature of the vector meson interaction, is reflected in a purely imaginary expectation value corresponding to a stationary phase approximation for complex saddle points.

The Lagrangian can be rewritten in momentum space by introducing $\Psi = \binom{N_1}{N_2}$, which gives

$$\mathcal{L} = \bar{\Psi} S_0^{-1} \Psi + \mathcal{L}_{\text{mes}}, \tag{3.19}$$

and

$$S_0^{-1} = \begin{pmatrix} -\mathrm{i}\not{p} + h_1(\sigma + \mathrm{i}\gamma_5 \vec{\pi}\vec{\tau}) + \mathrm{i}h_v \phi - \mu_B \gamma^0 & m_0 \gamma_5 \\ -m_0 \gamma_5 & -\mathrm{i}\not{p} + h_2(\sigma - \mathrm{i}\gamma_5 \vec{\pi}\vec{\tau}) + \mathrm{i}h_v \phi - \mu_B \gamma^0 \end{pmatrix}.$$

This form will later be the starting point of the RG considerations in Chap. 5.

Parameter fixing and phenomenology

In the previous sections the general setup of the parity-doublet model has been done, so now we want to briefly explain how the model parameters are fixed by experimental observables. As reflected in the model itself the most relevant degrees of freedom near the liquid-gas transition of nuclear matter matter are nucleons and mesons. There are, however, no nucleons in the vacuum, consequently the model parameters should be fixed at $T = 0$ and at values of the baryon chemical potential near the nuclear matter transition, guaranteeing small excitation energies for the nucleon. Due to the Silver-Blaze property, see App. B.2, we might as well fix the model parameters at vanishing temperatures and $\mu_B = 0$. It well known that in the local potential approximation this procedure introduces a minor artificial Silver-Blaze problem, which is mainly due to the curvature masses extracted from the effective potential by taking the $k \to 0$ limit

$$m_\sigma = \sqrt{2U_k' + 4U_k'' \phi^2}\,, \quad m_\pi = \sqrt{2U_k'}\,, \quad k \to 0\,, \tag{3.20}$$

do not coincide exactly with the physical particle masses. The physical masses are the pole masses, defined by the pole in the respective propagators. By calculating mesonic tow-point functions from their analytically continued RG flow equations [75, 77, 84–87] one can extract the pole masses and finds that they can differ significantly from the associated curvature masses. For instance, in the quark-meson-diquark model for two-color QCD [75] and the quark-meson model with isospin chemical potential [77] the curvature mass of the pion can differ by up to 30% from the pole mass. Furthermore, at mean-field level the pole masses, in the same model, agree with the onset of Bose-Einstein condensation of diquarks or charged pions. Similar results are seen in beyond mean-field calculations where the pole mass calculated from two-point functions in current truncation schemes is usually closer

to such onsets than the corresponding curvature masses. On the other hand, the difference between pole and curvature masses in purely mesonic $O(N)$-models is, in contrast to models including fermions, a rather small effect that can be ignored in most cases [84, 151]. This important difference between pole and curvature masses will be further discussed in Sec. 4.1 in the context of quark spectral functions calculated from the FRG. To reduce the large differences between curvature and pole masses, one has to extend the truncation beyond the local potential approximation (LPA) [152] by including wave function renormalization factors, cf. Sec. 3.4.1.

Still, since we want to study the parity-doublet model in LPA first, we ignore this discrepancy and use the usual curvature masses to fix our parameters. We have indeed verified, that fixing the parameters to realize a somewhat larger pion mass, as a primitive fix to compensate for the missing wave function renormalization factors, does not make a big difference in our results.

In the potential at the ultraviolet cutoff V_M we adjust the parameters to realize physical meson masses in the IR. For the pion, with a physical pion mass $m_\pi = 138$ MeV, this determines the explicit breaking parameter c. The sigma on the other hand is a broad resonance, see for example the hatched region in Fig. 3.5, making the fixing to a certain value not well constrained. We thus chose to fix its mass to reasonable values of $m_\sigma \sim 500$ MeV. The Yukawa couplings h_1 and h_2 are adjusted to realize the correct physical masses of the nucleons and their parity partners. This is done by solving Eq. (5.5) for $m_\pm$, for a fixed chiral invariant mass parameter m_0. The nucleon mass is $m_+ = 939$ MeV whereas we chose the $N(1535)$[9], with $m_- = 1535$ MeV, as its parity partner. The minimum of the effective potential in the IR, at $T = \mu_B = 0$ and $\vec{\pi} = 0$, is related to the pion decay constant by the Goldberger-Treiman relation [153, 154]

$$\bar{\sigma}_0 = f_\pi = 93 \text{ MeV} . \tag{3.21}$$

The in-medium condensate $\langle\bar{\psi}\psi\rangle(n_0) = \bar{\sigma}(n_0)$ [155–157] right at the liquid-gas phase transition is determined the Feynman-Hellmann theorem [158] in combination with the Gell-Mann-Oakes-Renner relation [159]. This gives a relation between the in-medium condensate $\bar{\sigma}(n_0)$ and the saturation density of nuclear matter n_0 [160]

$$\frac{\bar{\sigma}(n_0)}{\bar{\sigma}_0} = 1 - \frac{\sigma_N}{m_\pi^2 f_\pi^2}\, n_0. \tag{3.22}$$

Where on the right-hand side the so-called nucleon sigma term σ_N appears. The remaining two model parameters m_0 and h_v can hence be fixed by the physical saturation density of symmetric nuclear matter $n_0 \simeq 0.16$ fm^{-3} and a phenomenologically acceptable nucleon sigma term, given by $\sigma_N \simeq 36$ MeV [157].

[9] There is a slight ambiguity of what particle to chose as the parity partner of the nucleon. The two candidates that have the right quantum numbers and opposite parity as the nucleon are $N(1535)$ and $N(1640)$. For our purposes we just chose the $N(1535)$.

3.1.5. Promising mean-field results

As a final motivation to study the parity-doublet model within a FRG approach we want to note that the model showed very promising results at tree-level as well as in a mean-field approach [155, 161–170].

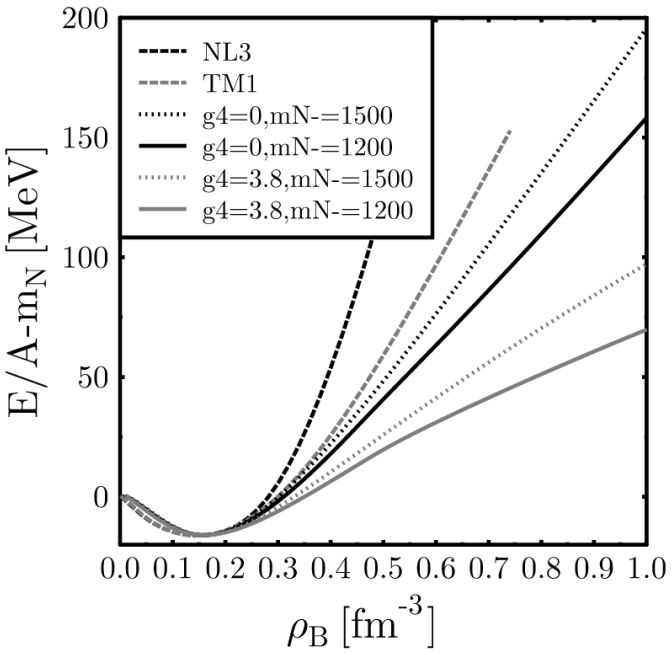

Figure 3.8.: Binding energy $E_b = \frac{E}{A} - m_N$ as a function of baryon density. A parity-doublet model was considered within a mean-field approximation. Results for different values of the vector coupling $g4$ and the parity partner mass m_{N_-} are plotted. Nuclear matter saturation density $\rho = 0.16$ fm^{-3} and a physical binding binding energy $E_b = -16$ MeV are realized. Figure taken from [161].

We want to show some results of a parity-doublet model considered within a mean-field approximation [161]. In Fig. 3.8 the binding energy $E_b = \frac{E}{A} - m_N$ is plotted as a function of the baryon density. Bound nuclear matter with the correct nuclear matter saturation density $\rho = 0.16$ fm^{-3} and physical binding energy $E_b = -16$ MeV could be realized in this approximation. These results were good motivation to study the effects of including mesonic as well as fermionic fluctuations beyond mean-field.

We will present results for the parity-doublet model from the FRG in Chap. 5.

3.2. Modelling of Quark Matter

3.2.1. The quark-meson model

In this section we want to introduce the chiral quark-meson model [171], as a low-energy model for QCD. In the $N_f = 2$ case its degrees of freedom consist of two degenerate quark flavors (u, d) and the scalar and pseudoscalar mesons $(\sigma, \vec{\pi})$. It has been successfully applied to explore the phase structure of QCD at finite temperature and chemical potential [31, 73].

The quark-meson model can be nicely motivated by considering a four-fermion interaction in the scalar and pseudoscalar channel, which is known to be the dominant channel driving dynamical chiral symmetry breaking. It is consequently a sufficient approximation considering a NJL-type four-fermion interaction of the form

$$\mathcal{L}_{\text{int}} = (\bar{\psi}\psi)^2 + (\bar{\psi} i\gamma_5 \vec{\tau}\psi)^2 \,, \tag{3.23}$$

as a low energy description of the chiral properties of QCD. Here $\psi = \begin{pmatrix} u \\ d \end{pmatrix}$ and $\vec{\tau}$ is the vector containing the Pauli matrices.

If we now take a look at the generating functional

$$Z = \int \mathcal{D}\psi \mathcal{D}\bar{\psi} e^{-S[\bar{\psi},\psi]} \,, \tag{3.24}$$

with

$$S[\bar{\psi},\psi] = \int \mathrm{d}^4x \Big((\bar{\psi}\psi)^2 + (\bar{\psi} i\gamma_5 \vec{\tau}\psi)^2 \Big) \,, \tag{3.25}$$

we can perform a Hubbard-Stratonovich transformation [172, 173] by multiplying the fermionic path integral in Eq. (3.24) with the following factor

$$\mathcal{N} \int \mathcal{D}\phi e^{-\int_x \frac{1}{2} m^2 \phi^2} \,, \tag{3.26}$$

with a normalization constant $\mathcal{N}$ and auxiliary four component scalar field ϕ. Such a factor does not change the fermionic path integral, we thus get the following modified generating functional

$$Z = \mathcal{N} \int \mathcal{D}\psi \mathcal{D}\bar{\psi} \mathcal{D}\phi e^{-\int_x [\frac{1}{2} m^2 \phi^2 + (\bar{\psi}\psi)^2 + (\bar{\psi} i\gamma_5 \vec{\tau}\psi)^2]} \,. \tag{3.27}$$

If we now shift the integration variables for the auxiliary field

$$\phi_0 \to \phi_0 + \frac{h^2}{2m}(\bar{\psi}\psi) \quad , \quad \phi_i \to \phi_i + \frac{h^2}{2m}(\bar{\psi}\gamma_5 \tau_i \psi) \,, \tag{3.28}$$

we end up with a yet again modified version of the generating functional

$$Z = \mathcal{N}' \int \mathcal{D}\psi \mathcal{D}\bar{\psi} \mathcal{D}\phi e^{-\int_x [\frac{1}{2} m^2 \phi^2 + h(\bar{\psi}\psi\phi_0 + \bar{\psi} i\gamma_5 \vec{\tau}\vec{\phi}\psi)]} \,. \tag{3.29}$$

Where we needed to set $h = 2m^2$, which we are free to do, since h and m were arbitrary parameters throughout.

So what we achieved through the Hubbard-Stratonovich transformation is an effective bosonization of the four-fermion interaction in terms of a Yukawa coupled term, which is bilinear in the fermion fields.

As a final step we identify the auxiliary field with the scalar meson σ and the pseudoscalar isospin triplet $\vec{\pi}$. This lets us write down the Lagrangian of the chiral two-flavor quark-meson model, as a bosonized NJL model with effective degrees of freedom

$$\sigma \sim \bar{\psi}\psi \quad , \quad \vec{\pi} \sim \bar{\psi} i\gamma_5 \vec{\tau} \psi \, , \tag{3.30}$$

giving

$$\mathcal{L} = \bar{\psi} i \partial\!\!\!/ \psi + h\bar{\psi}\big(\sigma + i\vec{\tau}\vec{\pi}\gamma_5\big)\psi + \frac{1}{2}(\partial_\mu \phi)^2 + U_k(\phi^2) - c\sigma. \tag{3.31}$$

Here we added kinetic terms for the bosonic fields $\phi = (\sigma, \vec{\pi})$ and added a general potential of the chiral invariant $U(\phi^2)$. Also we added a term $c\sigma$ which breaks chiral symmetry explicitly, to include non-vanishing pion masses. Spontaneous chiral symmetry breaking will be realized by a non-vanishing expectation value of the bosonic fields $\phi_0 = (\sigma_0, \vec{0})$. The three pions are then identified with the (pseudo-)Nambu-Goldstone bosons of the theory, whereas the condensation in the sigma direction gives the quarks a mass proportional to the Yukawa coupling $m_q = h\sigma_0$. Since the quark-meson model is a low energy model for QCD we will apply it with UV cutoff of about 1 GeV.

3.2.2. Reviewing the LPA phase diagram

We want to briefly review the phase diagram of the two-flavor quark-meson model in local potential approximation at finite temperature and density. In particular its low-temperature behavior as recently studied in detail in [74]. Typical mean-field calculations in the quark-meson model give a first-order critical line with $\frac{\mathrm{d}T_c}{\mathrm{d}\mu_c} < 0$. With a Clausius-Clapeyron equation [174]

$$\frac{\mathrm{d}T_c}{\mathrm{d}\mu_c} = -\frac{\Delta n}{\Delta s} \, , \tag{3.32}$$

for the difference in number density Δn and entropy density Δs, the mean-field calculations are usually consistent with an order-disorder transition, obeying both $\Delta n > 0$ and $\Delta s > 0$.

The quark-meson model has also been studied making use of the functional RG, see e.g. [73]. The simplest truncation allowing to include beyond mean-field fluctuations is the so-called local potential approximation, with an ansatz of the form

$$\mathcal{L} = \bar{\psi}\left(\gamma_\mu \partial^\mu + h(\sigma + i\vec{\tau}\vec{\pi}\gamma^5)\right)\psi + \frac{1}{2}(\partial_\mu \phi)^2 + U_k(\phi^2) - c\sigma \, , \tag{3.33}$$

which is the Euclidean counterpart of the Lagrangian (3.31). In this ansatz the only scale dependent object is the effective local potential U_k. Exploring the phase diagram at finite temperature and density within this truncation one finds a critical first-order line looking distinctly different, compared to mean-field calculations.

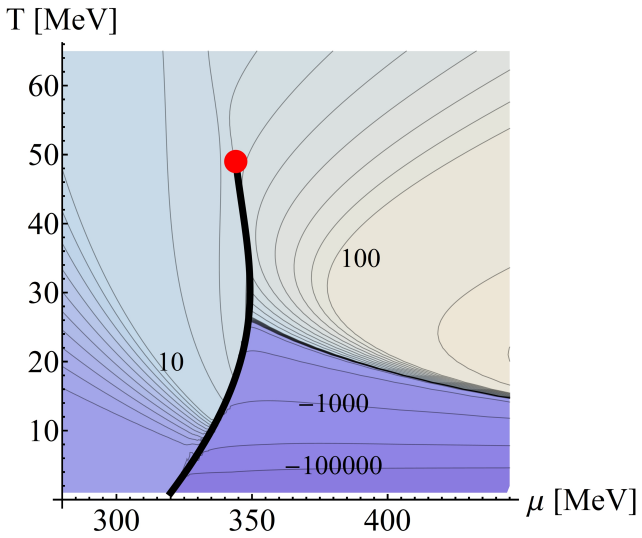

Figure 3.9.: Typical phase diagram of the LPA quark-meson model. For low temperatures the slope of the first-order critical line shows $\frac{\mathrm{d}T_c}{\mathrm{d}\mu_c} > 0$, leading to a region of negative entropy density, see inset numbers. Figure taken from [74].

In Fig. 3.9 a typical phase diagram of a LPA quark-meson model is shown. It can be seen that there is a region for low temperatures with $\frac{\mathrm{d}T_c}{\mathrm{d}\mu_c} > 0$. To interpret this behavior it is important to distinguish between entropy per particle and the entropy density (per volume). Going from a disordered to an ordered phase one expects the entropy per particle to decrease. This makes both signs for Δs possible, depending on the discontinuity in the number density. Only if the jump in the number density is large enough will $\Delta s > 0$ be possible even though the density per particle decreases. In the LPA quark-meson model, anyway, the density jump is not large enough leading to $\Delta s < 0$. This itself would not be a problem, but as it turns out the density jump Δs is larger than the entropy density on the disordered side of the critical line, leading to a region of negative entropy density beyond the critical line as indicated by the numbers in Fig. 3.9. This is, of course, phenomenologically problematic.

We found a similar general behavior when comparing mean-field calculations with local potential FRG calculations in the parity-doublet model [82], which we will discuss in detail in Sec. 5.2.2.

3.3. Analytic Continuation and Spectral Functions

A general issue arising in all Euclidean approaches to QCD is the problem of how to analytically continue back to real frequencies, which is needed in order to access observables like pole masses, spectral functions or transport coefficients. In finite temperature Euclidean approaches the Euclidean propagator is easily accessible, but only given on a discrete set of Matsubara frequencies $i\omega_i$. The question now is how to reconstruct the spectral function as a function of the continuous real frequency ω, when only a discrete set of data points is given as an input.

To get a better understanding of this issue consider the Källén-Lehmann spectral representation of the retarded, advanced and Euclidean propagator, given by

$$G^R(\omega,\vec{p}) = -\int_{-\infty}^{\infty} \mathrm{d}\omega' \frac{\rho(\omega',\vec{p})}{\omega'-\omega-i\epsilon}\,, \tag{3.34}$$

$$G^A(\omega,\vec{p}) = -\int_{-\infty}^{\infty} \mathrm{d}\omega' \frac{\rho(\omega',\vec{p})}{\omega'-\omega+i\epsilon}\,, \tag{3.35}$$

$$G^E(p_0,\vec{p}) = \int_{-\infty}^{\infty} \mathrm{d}\omega' \frac{\rho(\omega',\vec{p})}{\omega'-ip_0}\,. \tag{3.36}$$

It becomes clear, that the spectral function $\rho(\omega,\vec{p})$ governs the real as well as the imaginary time behavior of the propagator. Also the problem of how to reconstruct the spectral function from the Euclidean propagator $G^E(p_0,\vec{p})$, given on discrete $p_0 = p_{0,i}$, becomes apparent here. The Euclidean propagator is given by a continuous integral transform of the spectral function. Consequently, reconstructing the spectral function from the Euclidean propagator is an inverse problem, which becomes ill-posed when only a finite set of data points (including numerical errors), is given.

There are still methods to reconstruct spectral properties from noisy data which rely on so-called Bayesian reconstruction methods, the most successful of which is the maxim entropy method (MEM). MEM has been used in lattice QCD [175], as well as to calculate quark spectral functions around the pseudocritical temperature at vanishing density [176–178]. Also quark spectral functions have successfully been reconstructed from Euclidean data obtained from DSEs [179, 180].

3.3.1. Analytic continuation of flow equations

To avoid these sorts of reconstruction methods, we chose another route here, that will allow us to analytically continue on the level of the two-point flow equations, from which the spectral functions can be calculated directly.

From the Källén-Lehmann spectral representations Eqs. (3.34-3.36) we can express the retarded and advanced propagators through analytic continuation of the Euclidean propagator

$$G^R(\omega,\vec{p}) = -G^E(p_0 = -i\omega+\epsilon,\vec{p})\,, \tag{3.37}$$

$$G^A(\omega,\vec{p}) = -G^E(p_0 = -i\omega-\epsilon,\vec{p})\,. \tag{3.38}$$

A similar analytic continuation can be performed for the RG flow equations of two-point functions by applying the following two-step procedure.

In a first step the periodicity of the bosonic and fermionic occupation numbers with respect to the Euclidean momentum component $p_0 = 2\pi T n$ is used

$$n_B(E+i2\pi Tn) = n_B(E)\,, \tag{3.39}$$

$$n_F(E+i2\pi Tn) = n_F(E)\,. \tag{3.40}$$

This is possible because we use $3d$ Litim regulators, c.f. Sec. C.1.2, which allow for all appearing Matsubara sums to be performed analytically, which results in

terms containing bosonic and fermionic occupation numbers and their respective derivatives. In a second step we can perform the analytic continuation of the two-point function or its respective RG flow

$$\partial_k \Gamma_k^{(2),R}(\omega, \vec{p}) = -\partial_k \Gamma_k^{(2),E}(p_0 = -i\omega + \epsilon, \vec{p}) \; . \tag{3.41}$$

Taking the limit $\epsilon \to 0$, this guarantees retarded boundary conditions for the two-point function. Solving the RG flow equation one ends up with the retarded two-point function in the IR. From the retarded propagator $G^R(\omega, \vec{p})$, which is just the inverse of the retarded two-point function $\Gamma_k^{(2),R}(\omega, \vec{p})$ the spectral function can then directly be calculated

$$\rho(\omega, \vec{p}) = -\frac{1}{\pi} \mathrm{Im}\, G^R(\omega, \vec{p}), \tag{3.42}$$

is thus basically given by the imaginary part of the retarded propagator.

This two-step procedure yields physical Baym-Mermin boundary conditions [181] and has been applied in purely mesonic models [83, 84] as well as in a quark-meson model [85, 86], both studying meson spectral functions.

In Sec. 4.1 we apply this procedure to the RG flow of quark two-point functions within a quark-meson model and extract quark spectral functions from those. The generalization of this method to include propagators with explicit Dirac structure and the several different spectral functions following from those, is also in detail explained in the same section, Sec. 4.1.

3.4. Truncation and Numerical Procedure

3.4.1. Truncation schemes

The flow equation for the effective average action Eq. 2.66 can rarely be solved exactly, thus requires some sort of truncation schemes, i.e. expansions of the effective average action. The two most prominent ones are the vertex expansion [182] and the derivative expansion [67]. The vertex expansion is an expansion in terms of the 1-PI vertex functions leading to the following ansatz for the effective average action

$$\Gamma_k = \sum_N \frac{1}{N!} \big(\phi_{i1} \dots \phi_{iN}\big) \Gamma^{(N)}_{i1 \dots iN} \; . \tag{3.43}$$

Flow equations for n-point functions are then obtained by functional differentiation of the right-hand side of the Wetterich equation. This, anyway, results in an infinite tower of coupled flow equations similar to the one observed in DSEs, consequently the expansion has to be performed for a fixed order.

The derivative expansion, on the other hand, is a expansion in orders of derivatives and corresponds to an ansatz of the form

$$\Gamma_k = \int_x \big(U_k(\phi^2) + \frac{1}{2} Z_k (\partial_\mu \phi)^2 + \dots \big) \; . \tag{3.44}$$

In this thesis we work in the derivative expansion in two different truncation orders. The lowest order in the derivative expansion, where only the scale dependence of

the effective potential U_k is taken into account is commonly called local potential approximation (LPA). The first step beyond LPA is to also take scale dependent but field independent wave function renormalizations Z_k into account, which is commonly called LPA'.

3.4.2. Numerical methods

We now want to present two methods, most often used to solve RG flow equations for the effective potential.

Taylor expansion

Taylor expansion methods are very often used because of their very simple general idea. One expands the effective potential in a Taylor series around a scale dependent expansion point ϕ_k, leading to an ansatz of the form

$$U_k(\phi^2, \sigma) = \sum_n \frac{1}{n!} A_{n,k}(\phi^2 - \phi_k^2)^2 - c\sigma \ . \tag{3.45}$$

Consequently for the RG flow of the potential looks like

$$\partial_k U_k(\phi^2, \sigma) = \sum_n \frac{1}{n!} B_{n,k}(\phi^2 - \phi_k^2)^2 \ , \tag{3.46}$$

with scale dependent Taylor coefficients $B_{n,k} = \frac{\partial^n \partial_k U_k}{\partial \phi^n}|_{\phi=\phi_k}$. Although, this is rather simple conceptually, one has to appreciate that the scale dependent Taylor coefficients involve increasing numbers of ϕ-derivatives of the original right-hand side of the Wetterich equation for the effective potential itself. This, of course, makes the flow equations for the Taylor coefficients B_k increasingly complicated, depending on the order of the Taylor expansion.

While Taylor expansions are well suited for the calculation of critical exponents, first order phase transitions cannot be described as easily, since the expansion only includes information of the effective potential in the vicinity of a local minimum and to a fixed order in the fields.

Grid method

The so-called grid method, on the other hand, has the advantage that it keeps the full field-dependence of the effective potential intact, hence arbitrarily high field interactions are in principle included. This makes the grid method well suited to study first order phase transitions, since the potential can develop several minima. From a technical standpoint the RG flow equations we are dealing with are functional differential equations of the form

$$\partial_k U_k(\phi^2) = f(k, \phi(x), U_k', \ldots, U_k^{(n)}, Z_{1,k}, \ldots, Z_{m,k}, Z_{1,k}', \ldots, Z_{m,k}') \ , \tag{3.47}$$

where the $Z_{i,k}$ and $Z_{i,k}'$ indicate the possible inclusion of wave function renormalization in beyond LPA considerations, for LPA they are set to $Z_{i,k} = 1$. What all grid methods have in common is that they rely on a discretization in field space. The

dependence on the continuous field variable ϕ is replaced by a finite grid ϕ_i. This transforms the functional differential equation into a finite system of coupled ordinary differential equations, where the number of grid points typically lies between 50 and 100. This system of ordinary differential equations is coupled through the potential's derivatives $U_k', \ldots, U_k^{(n)}$, which are approximated by finite differences or spline interpolations.

In the LPA case Eq. (3.47) can be directly integrated using standard ODE solvers like the Runge-Kutta method.

In the case including wave function renormalization $Z_{i,k}$, which fulfill their own RG flow equations we solve the coupled system for U_k and $Z_{i,k}$ applying an iterative procedure. Starting with a LPA step, we solve the RG flow for the potential first. On this scale dependent solution for the potential we solve the RG flow for the wave function renormalizations $Z_{i,k}$, which are then used as scale dependent input for a new potential integration. This procedure is repeated until we see convergence in the renormalized observables.

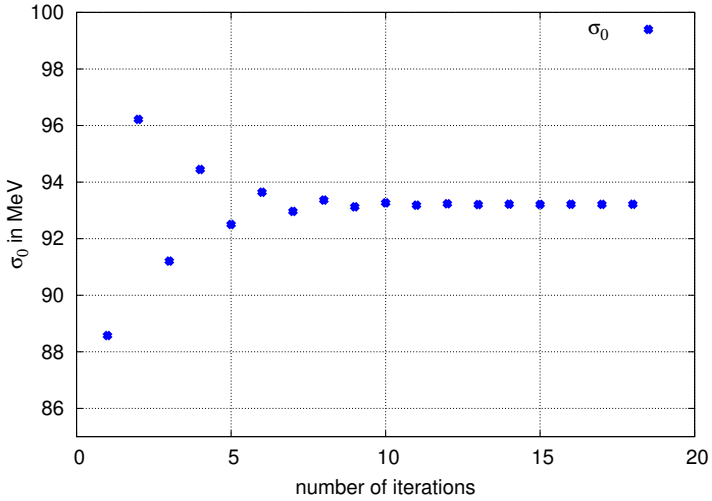

Figure 3.10.: Shown is the renormalized chiral condensate in the IR as a function of the number of iterations.

As an example, in Fig. 3.10 we show the renormalized chiral condensate $\sigma_0 = \sqrt{Z_{\sigma,IR}}\sigma_{0,\text{bare}}$ in the IR as a function of the number of iterations. It can be seen that with increasing number of iterations the condensate clearly converges against its physical value $\sigma_0 \simeq 93$ MeV.

4

Quark Matter Results

4.1. Quark Matter and Quark Spectral Functions

The method of calculating spectral functions from analytically continued flow equations has been put forward in recent years in purely mesonic $O(n)$-models [84] as well as in chiral quark-meson models [85, 86]. These works are exclusively concerned with the calculation of mesonic spectral functions from the RG flow of the meson two-point functions. Here we want to extend these methods to calculate real-time quark two-point functions and quark spectral functions within a chiral quark-meson model as an effective model for QCD.

4.1.1. RG Flow for U_k and $\Gamma^{(2)}_{\psi,k}$

Let us start with a brief discussion of the RG flow of the local scale-dependent potential U_k and the resulting flow of the scale dependent quark two-point function. Starting from the Lagrangian of the quark-meson model in Euclidean space-time and local potential approximation as introduced in Sec. 3.2.2

$$\mathcal{L} = \bar{\psi}\left(\gamma_\mu \partial^\mu + h(\sigma + i\vec{\tau}\vec{\pi}\gamma^5)\right)\psi + \frac{1}{2}(\partial_\mu \phi)^2 + U_k(\phi^2) - c\sigma\,, \tag{4.1}$$

where we used hermitian γ-matrices, see App. A.1 and $\phi = (\sigma, \vec{\pi})$. Plugging this ansatz into the Wetterich equation, cf. Eq. (2.67), we get the following, well known expression for the flow of the effective potential, cf. eg. [73]

$$\begin{aligned}\partial_k U_k = &\frac{k^4}{12\pi^2}\left[\frac{1 + 2n_B(\epsilon_k^\sigma)}{\epsilon_k^\sigma} + \frac{(N_f^2 - 1)(1 + 2n_B(\epsilon_k^\pi))}{\epsilon_k^\pi}\right] \\ &- \frac{N_c N_f k^4}{3\pi^2}\left[\frac{1 - n_F(\epsilon_k^\psi - \mu) - n_F(\epsilon_k^\psi + \mu)}{\epsilon_k^\psi}\right].\end{aligned} \tag{4.2}$$

See App. C.1 for details. In Eq. (4.2) we used the scale-dependent single-quasiparticle energies

$$\begin{aligned} \epsilon_k^\sigma &= \sqrt{k^2 + m_\sigma^2} = \sqrt{k^2 + 2U_k' + 4U_k''\sigma^2}\,, \\ \epsilon_k^\pi &= \sqrt{k^2 + m_\pi^2} = \sqrt{k^2 + 2U_k'}\,, \\ \epsilon_k^\psi &= \sqrt{k^2 + m_\psi^2} = \sqrt{k^2 + (h\sigma)^2}\,. \end{aligned} \tag{4.3}$$

Those give us the Euclidean curvature masses for $k \to 0$

$$\begin{aligned} m_\sigma &= \sqrt{2U_k' + 4U_k''\sigma^2}\,, \\ m_\pi &= \sqrt{2U_k'}\,, \\ m_\psi &= h\sigma\,. \end{aligned} \tag{4.4}$$

Where σ is understood as the IR minimum of the effective potential $U_k|_{k\to 0}$ and U_k', U_k'' are derivatives with respect to the invariant ϕ^2.

In the UV the potential is assumed to be symmetric

$$U_\Lambda(\phi^2) = \frac{1}{2}m_\Lambda^2\phi^2 + \frac{1}{4}\lambda_\Lambda(\phi^2)^2, \tag{4.5}$$

while the explicit symmetry breaking term $c\sigma$, corresponding to the current quark mass, is only added to the effective potential in the IR. Spontaneous chiral symmetry breaking on the other hand is considered dynamically by quark fluctuations which are included by integrating the flow equation in Eq. (4.2) from the UV cutoff Λ down to the IR.

Flow of $\Gamma^{(2)}_{\psi,k}$

To calculate the flow of the quark two-point function one has to take two functional derivatives of the flow of the effective average action Γ_k, which is formally equivalent to pulling two quark legs out of the (diagrammatic) Wetterich equation, cf. Fig. 2.4.

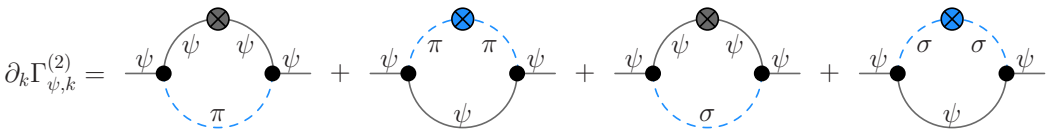

Figure 4.1.: Diagrammatic representation of the RG flow of the quark two-point function.

This leads to the four mixed loops in Fig. 4.1, where grey and blue crossed circles stand for (fermionic) bosonic regulator insertions. These diagrams in principle give us the full scale dependent Euclidean quark two-point function. The black dots represent the vertex functions $\Gamma^{(3)}_{\bar\psi\psi(\sigma/\pi)}$ which are obtained from the ansatz

in Eq. (4.1) and are given in App. C.1.4. The analytic continuation of $\partial_k \Gamma^{(2)}_{\psi,k}$ to real frequencies and the projection onto its different Dirac-structures give access to several different quark spectral functions, as we will explain in the following.

4.1.2. Analytic continuation and quark spectral functions

Starting from the Euclidean Lagrangian in Eq. (4.1) one can read off the form of the Euclidean two-point function after performing a Fourier transform to get its momentum space representation. Setting the meson fields to their vacuum expectation values $\tilde{\phi} = (\sigma, \vec{0})$, we find the well known form of the Euclidean quark two-point function at the UV scale Λ

$$\Gamma^{(2),E}_{\Lambda,\psi}(p_0, \vec{p}) = -i\not{p} + m = -i\gamma_0 p_0 - i\vec{\gamma}\vec{p} + h\sigma \,. \tag{4.6}$$

Now the analytic continuation can be performed by setting the Euclidean zero-component $p_0 = -iz$ and assuming $z = \omega + i\epsilon$. This guarantees retarded boundary conditions for the quark two-point function when taking the limit $\epsilon \to 0$. For the imaginary part of the two-point flow equations the limit $\epsilon \to 0$ can be performed analytically, as done in Ref. [87]. An additional overall minus sign needs to be introduced compared to Eq. (4.6) to end up with the standard form of the Dirac operator in Minkowski space-time

$$\Gamma^{(2)}_{\Lambda,\psi}(z, \vec{p}) = \gamma_0 z + i\vec{\gamma}\vec{p} - h\sigma \,. \tag{4.7}$$

Keeping the hermitian $\gamma-$matrices will be beneficial in the actual calculations of the flow equations for the two-point functions, where usually one changes to their anti-hermitian counterparts ($\vec{\gamma} \to i\vec{\gamma}$) in Minkowski space-time.

Considering that the RG flow keeps the Dirac structure intact we make the following ansatz for the full scale-dependent quark two-point function

$$\Gamma^{(2)}_{k,\psi}(\omega, \vec{p}) = \gamma_0 C_k(\omega, \vec{p}) + i\vec{\gamma}\hat{\vec{p}}\, A_k(\omega, \vec{p}) - B_k(\omega, \vec{p}) \,, \tag{4.8}$$

where we introduced the normalized momentum variable $\hat{\vec{p}} \equiv \vec{p}/|\vec{p}|$. All fluctuation induced modifications occurring in the full quark two-point function are by this ansatz encoded in the dressing functions $A_k(\omega, \vec{p})$, $B_k(\omega, \vec{p})$ and $C_k(\omega, \vec{p})$. The UV values of the dressing functions can be read off comparing Eq. (4.7) with Eq. (4.8), giving

$$A_\Lambda(\omega, \vec{p}) = |\vec{p}| \,, \tag{4.9}$$
$$B_\Lambda(\omega, \vec{p}) = h\sigma \,, \tag{4.10}$$
$$C_\Lambda(\omega, \vec{p}) = \omega \,. \tag{4.11}$$

The full scale dependent dressings are obtained by projecting on the corresponding Dirac structures of $\Gamma^{(2)}_{k,\psi}(\omega, \vec{p})$. The projections are given by

$$\begin{aligned} A_k(\omega, \vec{p}) &= -\frac{1}{4} \operatorname{tr}\left(i\vec{\gamma}\hat{\vec{p}}\, \Gamma^{(2)}_{k,\psi}(\omega, \vec{p}) \right) , \\ B_k(\omega, \vec{p}) &= -\frac{1}{4} \operatorname{tr}\left(\Gamma^{(2)}_{k,\psi}(\omega, \vec{p}) \right) , \\ C_k(\omega, \vec{p}) &= \frac{1}{4} \operatorname{tr}\left(\gamma_0 \Gamma^{(2)}_{k,\psi}(\omega, \vec{p}) \right) . \end{aligned} \tag{4.12}$$

Since the flow equation for the quark two-point function has the following form

$$\partial_k \Gamma^{(2)}_{k,\psi}(\omega,\vec{p}) = \gamma_0 \partial_k C_k(\omega,\vec{p}) + i\vec{\gamma}\hat{\vec{p}}\,\partial_k A_k(\omega,\vec{p}) - \partial_k B_k(\omega,\vec{p})\,, \tag{4.13}$$

the flow equations for the dressing functions can be obtained by the same projections Eqs. (4.12). Explicit expressions for $\partial_k B_k(\omega,\vec{p})$ and $\partial_k C_k(\omega,\vec{p})$ are given in App. C.1.4 . Later on we will need the imaginary parts of the quark propagator to define the different quark spectral functions, so let us also write down the inverse of the retarded quark two-point function in Eq. (4.8)

$$G_{k,\psi}(\omega,\vec{p}) = \gamma_0 G^{(C)}_{k,\psi}(\omega,\vec{p}) + i\vec{\gamma}\hat{\vec{p}}\,G^{(A)}_{k,\psi}(\omega,\vec{p}) + G^{(B)}_{k,\psi}(\omega,\vec{p})\,. \tag{4.14}$$

Here the different components $G^{(A)}_{k,\psi}$, $G^{(B)}_{k,\psi}$ and $G^{(C)}_{k,\psi}$ are obtained similarly to the Dirac components of the quark two-point function itself [10], giving

$$\begin{aligned}
G^{(A)}_{k,\psi}(\omega,\vec{p}) &= \frac{A_k(\omega,\vec{p})}{C_k^2(\omega,\vec{p}) - A_k^2(\omega,\vec{p}) - B_k^2(\omega,\vec{p})}\,,\\
G^{(B)}_{k,\psi}(\omega,\vec{p}) &= \frac{B_k(\omega,\vec{p})}{C_k^2(\omega,\vec{p}) - A_k^2(\omega,\vec{p}) - B_k^2(\omega,\vec{p})}\,,\\
G^{(C)}_{k,\psi}(\omega,\vec{p}) &= \frac{C_k(\omega,\vec{p})}{C_k^2(\omega,\vec{p}) - A_k^2(\omega,\vec{p}) - B_k^2(\omega,\vec{p})}\,.
\end{aligned} \tag{4.15}$$

In the UV the full scale dependent quark propagator defined by Eq. (4.14) takes the form

$$G_{\Lambda,\psi}(\omega,\vec{p}) = \frac{\gamma_0\omega + i\vec{\gamma}\vec{p} + h\sigma}{(\omega+i\epsilon)^2 - \vec{p}^{\,2} - h^2\sigma^2}\,, \tag{4.16}$$

which indeed is the usual form of a quark propagator with mass $m = h\sigma$ and retarded boundary conditions, indicated by the term $\omega + i\epsilon$.

The quark spectral function is defined by the imaginary part of the retarded propagator, as we already introduced in Sec. 3.3

$$\rho_{k,\psi}(\omega,\vec{p}) = -\frac{1}{\pi}\mathrm{Im}\,G_{k,\psi}(\omega,\vec{p}) \tag{4.17}$$

and consequently has the same Dirac structure as $G_{k,\psi}$ itself

$$\rho_{k,\psi}(\omega,\vec{p}) = \gamma_0 \rho^{(C)}_{k,\psi}(\omega,\vec{p}) + i\vec{\gamma}\hat{\vec{p}}\,\rho^{(A)}_{k,\psi}(\omega,\vec{p}) + \rho^{(B)}_{k,\psi}(\omega,\vec{p})\,, \tag{4.18}$$

where the individual components are directly connected to the respective Dirac components of the propagator

$$\rho^{(A,B,C)}_{k,\psi}(\omega,\vec{p}) = -\frac{1}{\pi}\mathrm{Im}\,G^{(A,B,C)}_{k,\psi}(\omega,\vec{p})\,. \tag{4.19}$$

[10] It is worth pointing out that $G_{k,\psi}(\omega,\vec{p})$ is not to confuse with the regulated propagator $D_\psi = (\Gamma^{(2)}_k + R_k)^{-1}$ occurring in the flow of the Euclidean two-point function, cf. Fig. 4.1. It is the inverse of the full scale-dependent retarded two-point function $\Gamma^{(2)}_{k,\psi}$ in Eq. (4.8).

From Eq. (4.16) we then find

$$\rho_{\Lambda,\psi}(\omega,\vec{p}) = \mathrm{sgn}(\omega)(\gamma_0\omega + i\vec{\gamma}\vec{p} + h\sigma)\delta(\omega^2 - \vec{p}^2 - h^2\sigma^2)\,. \tag{4.20}$$

for the quark spectral function in the UV. By definition $\rho^{(C)}_{k,\psi}(\omega,\vec{p})$ is even, while $\rho^{(A)}_{k,\psi}(\omega,\vec{p})$ and $\rho^{(B)}_{k,\psi}(\omega,\vec{p})$ are odd with respect to the frequency ω

$$\begin{aligned}
\rho^{(C)}_{k,\psi}(-\omega,\vec{p}) &= \rho^{(C)}_{k,\psi}(\omega,\vec{p})\,,\\
\rho^{(A)}_{k,\psi}(-\omega,\vec{p}) &= -\rho^{(A)}_{k,\psi}(\omega,\vec{p})\,,\\
\rho^{(B)}_{k,\psi}(-\omega,\vec{p}) &= -\rho^{(B)}_{k,\psi}(\omega,\vec{p})\,.
\end{aligned} \tag{4.21}$$

As a first simplification let us only study quark spectral functions at vanishing external spatial momentum $\vec{p}=0$, which then gives $G^{(A)}_{k,\psi}(\omega,0)\equiv 0$ and $\rho^{(A)}_{k,\psi}(\omega,0)\equiv 0$. The quark propagator can then further be decomposed using the projectors on positive/negative energies

$$\Lambda_\pm = (1\pm\gamma_0)/2 \tag{4.22}$$

which of course obey the properties $\Lambda_\pm\Lambda_\pm = \Lambda_\pm$, $\Lambda_\pm\Lambda_\mp = 0$ and $\Lambda_+ + \Lambda_- = 1$, giving

$$G_{k,\psi}(\omega) = G^+_k(\omega)\Lambda_+ + G^-_k(\omega)\Lambda_-\,. \tag{4.23}$$

Where the individual components are obtained through

$$G^\pm_k(\omega) = \frac{1}{2}\mathrm{tr}\left(G_{k,\psi}(\omega)\Lambda_\pm\right). \tag{4.24}$$

Consequently the corresponding quark and anti-quark spectral functions are given by

$$\rho^\pm_k(\omega) = \mp\frac{1}{\pi}\mathrm{Im}\,G^\pm_k(\omega)\,, \tag{4.25}$$

where the sign on the right-hand side has been chosen such as to give an even symmetry relation with respect to ω between the quark and anti-quark spectral function

$$\rho^+_k(-\omega) = \rho^-_k(\omega)\,. \tag{4.26}$$

Expressed in terms of the dressing functions B_k and C_k they take the form

$$\rho^+_k(\omega) = \frac{1}{\pi}\frac{\mathrm{Im}\,C_k - \mathrm{Im}\,B_k}{(\mathrm{Re}\,C_k - \mathrm{Re}\,B_k)^2 + (\mathrm{Im}\,C_k - \mathrm{Im}\,B_k)^2}\,, \tag{4.27}$$

$$\rho^-_k(\omega) = \frac{1}{\pi}\frac{\mathrm{Im}\,C_k + \mathrm{Im}\,B_k}{(\mathrm{Re}\,C_k + \mathrm{Re}\,B_k)^2 + (\mathrm{Im}\,C_k + \mathrm{Im}\,B_k)^2}\,. \tag{4.28}$$

Finally we can relate the quark and anti-quark spectral function back to $\rho^{(B)}_k(\omega)$ and $\rho^{(C)}_k(\omega)$ from earlier

$$\begin{aligned}
\rho^{(B)}_{k,\psi}(\omega) &= \frac{1}{2}\Big(\rho^+_k(\omega) - \rho^-_k(\omega)\Big)\,,\\
\rho^{(C)}_{k,\psi}(\omega) &= \frac{1}{2}\Big(\rho^+_k(\omega) + \rho^-_k(\omega)\Big)\,.
\end{aligned} \tag{4.29}$$

4.1.3. Numerical results for quark spectral functions

Let us now discuss results for the scale dependent curvature masses which are defined in Eqs. (4.4) since those are used as an input to solve the flow of the quark two-point functions in Fig. 4.1 later on. The results are obtained by solving the flow equation in Eq. (4.2) and evaluating the respective scale-dependent masses. Generally, an important distinction should be made when calculating curvature masses at the scale-dependent minimum $\sigma_{0,k}$ compared to at the IR minimum σ_0, which of course is independent of the scale k. Only if evaluated at the global minimum of the effective potential U_k do the so-called curvature masses in Eqs. (4.4) represent particle masses in the usual sense.

In Fig. 4.2 we plotted the curvature masses for pions, sigma-meson and quarks. The solutions were obtained on a grid, each evaluated at the IR minimum σ_0 (solid lines) and at the scale-dependent minimum $\sigma_{0,k}$ (dotted lines). Additionally we show masses obtained from a fourth order Taylor calculation (dashed lines).

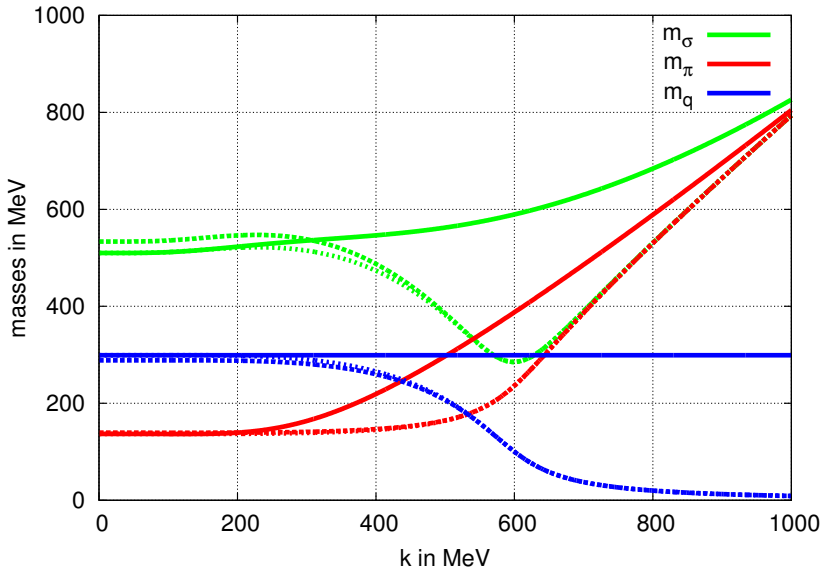

Figure 4.2.: Shown are euclidean (curvature) masses of the pion, sigma and quark, as a function of the RG scale k. The solid lines correspond to solutions from the grid evaluated at the IR minimum σ_0. The dotted lines correspond to grid-solutions evaluated at the k-dependent minimum $\sigma_{0,k}$ and dashed lines to a 4th order Taylor calculation.

At the UV scale of $k = 1000$ MeV the meson masses in either case are degenerate as expected, since the RG flow starts out with a symmetric potential, cp. Eq. (4.5). Going away from the UV the solutions evaluated at $\sigma_{0,k}$ and the fourth order Taylor solutions are basically lying on top of each other, which makes sense since the Taylor method by definition uses a scale dependent minimum. For the scale dependent (and Taylor) solutions the masses of the pion and sigma-meson remain degenerate up to the chiral symmetry breaking scale of roughly 600 MeV. In the same region the quark mass starts rising up from zero in the UV, as compared to the solution evaluated at the IR minimum which gives a constant quark mass of

$h\sigma_0$. Now turning to Fig. 4.3, which shows a close-up version of Fig. 4.2, focussing on the scales below the chiral symmetry breaking scale of 600 MeV. It can be seen that the solutions evaluated at $\sigma_{0,k}$ approach the solutions evaluated at σ_0 in the IR, as they should, since $\lim_{k\to 0} \sigma_{0,k} = \sigma_0$. Also the Taylor solutions show a minor discrepancy in the IR, which is due to slightly different parameters used in this method.

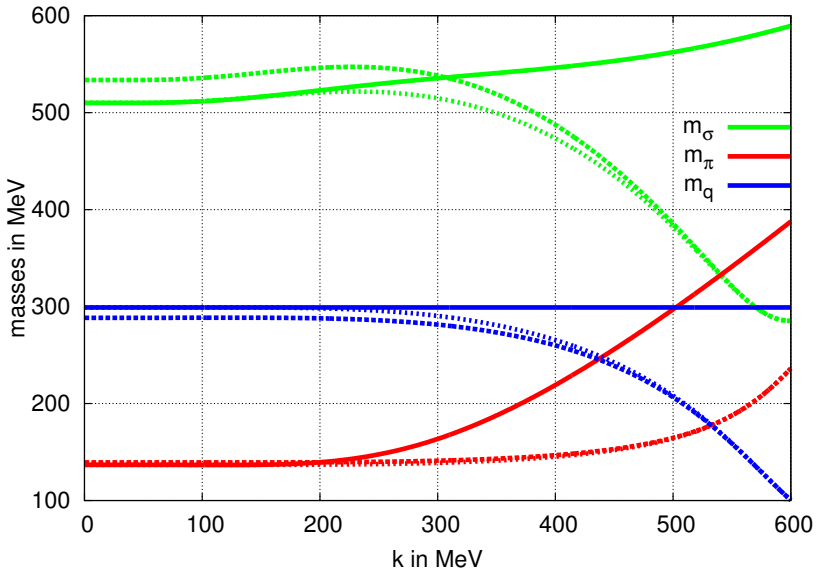

Figure 4.3.: Close-up version of Fig. 4.2. Solid lines again correspond to solutions evaluated at the IR minimum σ_0, dotted lines to grid-solutions evaluated at $\sigma_{0,k}$ and dashed lines to a Taylor calculation.

When studying the RG flow of the quark two-point functions we will still solve them at σ_0, after all they agree in the IR, where the effective average action in the FRG approaches the full quantum action (up to truncation effects), hence all the relevant physics is taken into account. Still if we want to interpret the behavior of the scale-dependent curvature masses throughout the RG flow, we can always evaluate them at the scale dependent minimum $\sigma_{0,k}$ as done here in Figs. 4.2 and 4.3.

As already mentioned before, in this section we consider vanishing temperature and chemical potential, as well as a zero external spatial momentum $\vec{p} = 0$. In this setup the dressing functions $B_k(\omega)$ and $C_k(\omega)$ are the only remaining non-trivial quantities. Those are calculated from the RG flow of the full scale dependent quark two-point function which is analytically continued to real frequencies ω and projected onto the respective Dirac structures as described in Eq. (4.12). The flow equations $\partial_k B_k(\omega)$ and $\partial_k C_k(\omega)$ can then be numerically integrated using the scale-dependent effective potential as an input. Since the RG flow of the two-point function does not couple different points in the σ-grid, we evaluate it at the IR minimum σ_0 throughout.

In Fig. 4.4 we show the real parts of the dressing functions $B_k(\omega)$ and $C_k(\omega)$ in the IR. Already from these figures several interesting features can be observed.

Since the quark pole mass is defined by the pole of the quark propagator, it can be obtained from the real parts of the dressing functions $\mathrm{Re}\, B_k(\omega)$ and $\mathrm{Re}\, C_k(\omega)$ by solving $\mathrm{Re}\, B_k(m_{\mathrm{pole}}) = \mathrm{Re}\, C_k(m_{\mathrm{pole}})$, as can for example be seen from Eqs. (4.15). This anyway can directly be read off of Fig. 4.4 and in this case it is around 380 MeV. The discrepancy between the pole and screening masses in LPA approaches will be discussed shortly.

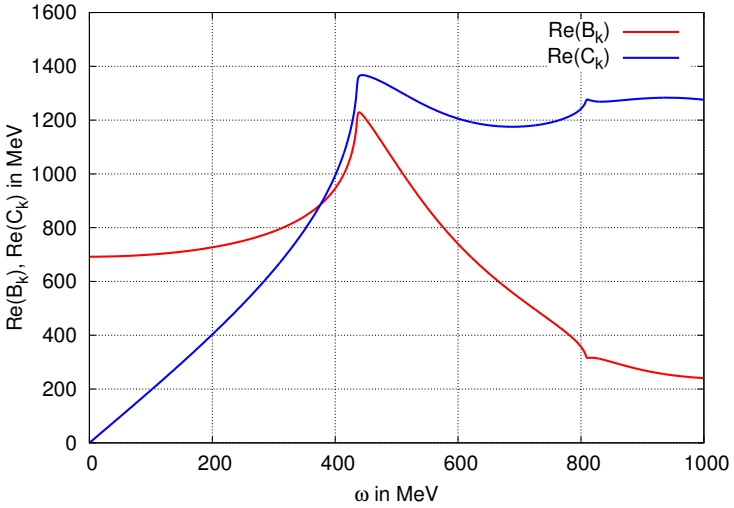

Figure 4.4.: Shown are the real parts of the dressing functions $B_k(\omega)$ and $C_k(\omega)$ as a function of the real frequency ω in the IR.

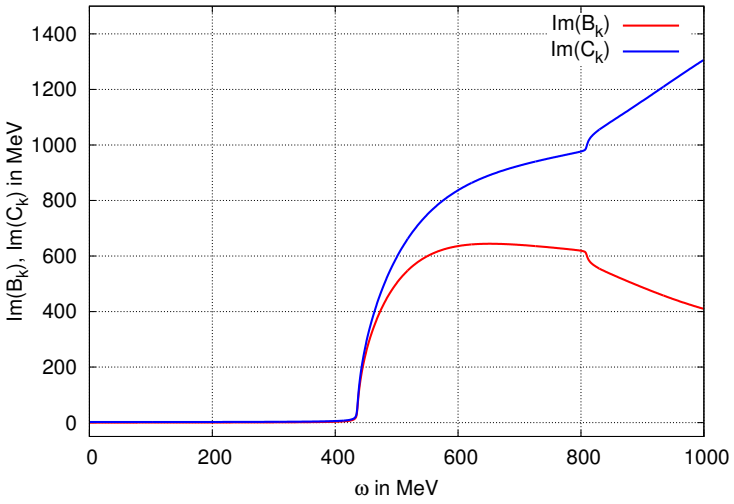

Figure 4.5.: Shown are the imaginary parts of the dressing functions $B_k(\omega)$ and $C_k(\omega)$ as a function of the real frequency ω in the IR.

Also we want to note that $\mathrm{Re}\, C_k(\omega)$ in the region of low ω already significantly deviates from its UV form $\mathrm{Re}\, C_\Lambda(\omega) = \omega$ having a much steeper slope, for larger ω it then shows a distinct non-trivial behavior. In Fig. 4.5 we show the corresponding

plot for the imaginary parts of the dressings $\mathrm{Im}\, B_k(\omega)$ and $\mathrm{Im}\, C_k(\omega)$. In this case both dressing remain zero up to a frequency of 440 MeV, where a first threshold opens up, which will later of course also show up and further be discussed in the context of the spectral functions $\rho_k^{\pm}(\omega)$ and $\rho_k^{(C)}(\omega)$.

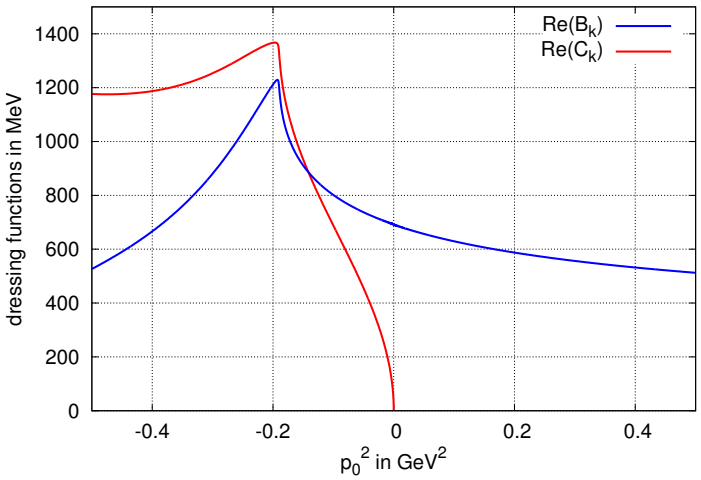

Figure 4.6.: The real parts of the dressings B_k and C_k as a function of p_0^2. Negative p_0^2 correspond to Minkowski space-time, positive p_0^2 to Euclidean solutions. The position of the quark pole mass can be read of for $\mathrm{Re}\, B_k(m_{\mathrm{pole}}) = \mathrm{Re}\, C_k(m_{\mathrm{pole}})$.

But let us now come to Fig. 4.6, where the real parts of B_k and C_k are plotted over p_0^2. This means that for negative p_0^2 we recover the results from Fig. 4.4, since $p_0^2 < 0$ corresponds to solutions in Minkowski space-time with a real frequency $\omega = ip_0$.

On the other hand for $p_0^2 > 0$ we solved the Euclidean analogues of $\partial_k B_k$, i.e. the non-continued imaginary time flow equations for the dressing B_k. B_k for large positive p_0^2 actually tends towards $m_\psi = h\sigma_0 \simeq 299$ MeV, which just reflects the UV value of $B_\Lambda = h\sigma_0$. In the UV all loop contributions to B_k vanish and $B_k(p_0^2)$ approaches the Euclidean (grid-) quark mass m_ψ.

As mentioned above, the form of the dressing functions $B_k(\omega)$ and $C_k(\omega)$ already gives quite some insight to the main features of our model. Going back to the diagrammatic representation of the flow of the quark two-point function in Fig. 4.1 we can read off the possible particle processes, e.g. the ones including pions and quarks are

$$\psi^* \;\rightarrow\; \psi + \pi \quad \text{for} \quad \omega \geq \epsilon_\psi + \epsilon_\pi \,, \tag{4.30}$$

$$\bar{\psi}^* \;\rightarrow\; \bar{\psi} + \pi \quad \text{for} \quad \omega \geq \epsilon_\psi + \epsilon_\pi \tag{4.31}$$

where for example ψ^* stands for an off-shell quark with energy ω, which may decay into an on-shell quark and pion with energies ϵ_ψ and ϵ_π, respectively. This very process gives rise to the first threshold clearly visible in Fig. 4.5 as well as in Figs. 4.7 and 4.8 which show the actual quark spectral functions $\rho_k^{\pm}(\omega)$ in Fig. 4.7

and $\rho^{(B,C)}_{k,\psi}(\omega)$ in Fig. 4.8. In our case the threshold opens up at at roughly 440 MeV in good agreement with $\omega = m_\psi + m_\pi = 437$ MeV and (with $m_\psi = 299$ MeV $m_\pi = 138$ MeV for the parameters used here). Analogous to the pion processes the processes involving sigma-mesons look like

$$\psi^* \rightarrow \psi + \sigma \quad \text{for} \quad \omega \geq \epsilon_\psi + \epsilon_\sigma \,, \tag{4.32}$$

$$\bar{\psi}^* \rightarrow \bar{\psi} + \sigma \quad \text{for} \quad \omega \geq \epsilon_\psi + \epsilon_\sigma \,. \tag{4.33}$$

In this case the same principles apply for the excited quark being able to decay into an on-shell quark and a sigma-meson this time. This process, anyway, is also clearly visible in Fig. 4.5 as well as Figs. 4.7 and 4.8, opening up at about 800 MeV, also in good agreement with $\omega = m_\psi + m_\sigma = 808$ MeV, with a sigma-mass of $m_\sigma = 509$ MeV and again $m_\psi = 299$ MeV.

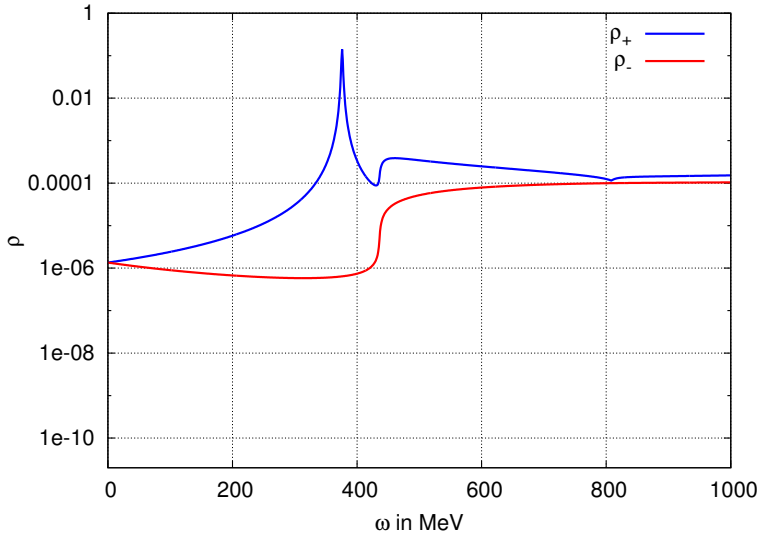

Figure 4.7.: The spectral functions for quarks (ρ_+) and antiquarks (ρ_-) as a function of the frequency ω.

Coming now in more detail to the form of the quark and anti-quark spectral functions $\rho^\pm_k(\omega)$ in Fig. 4.7, one can see a clear peak around a pole mass of about 380 MeV in the quark spectral function $\rho^+_k(\omega)$. This one-particle peak at positive frequencies is not appearing in $\rho^-_k(\omega)$, as expected. The corresponding plot for negative frequencies ω may easily be reconstructed by using the symmetry relation

$$\rho^+_k(-\omega) = \rho^-_k(\omega) \,. \tag{4.34}$$

At this point it is worth noting that the calculations shown here are all performed at a finite value of $\epsilon = 1$ MeV, which can clearly be seen by the finite width and height of the single-particle peaks in Figs. 4.7 and 4.8. Anyway, all the main features like the position of the pole mass and particle thresholds can still be extracted from the finite ϵ spectral functions. The corresponding $\epsilon = 0$ spectral functions will only be used later on in Sec.4.1.4 in the context of sum rules for the quark propagator.

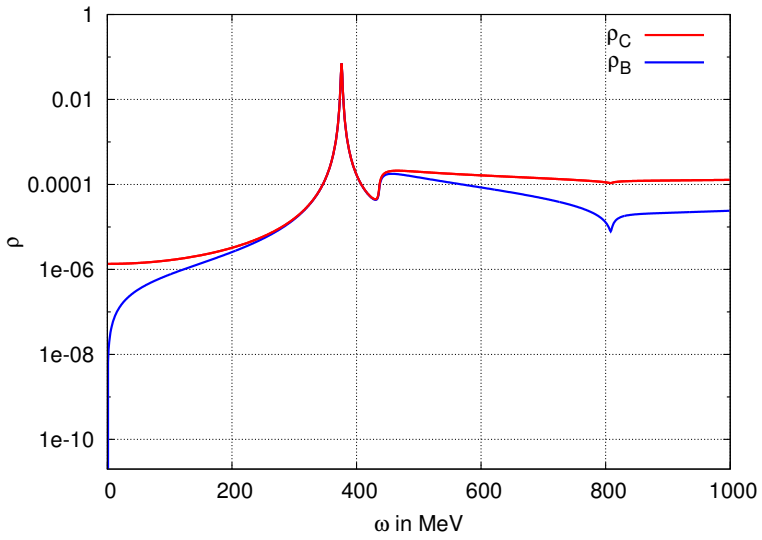

Figure 4.8.: The spectral functions ρ_C and ρ_B as a function of the frequency ω.

A convenient consistency check for our calculations is the following inequality that holds for $\rho^{(B)}_{k,\psi}$ and $\rho^{(C)}_{k,\psi}$

$$\rho^{(B)}_{k,\psi} \leq \rho^{(C)}_{k,\psi}(\omega) \,, \tag{4.35}$$

which follows directly from Eqs. 4.29. This inequality, as can be seen from Fig. 4.8 is numerically fulfilled to satisfactory degree. Coming back to the discussion about pole masses obtained from RG calculations in local potential approximation, it is known that for example the pion curvature mass can deviate from its pole mass by about 30% [75, 84, 87], where the pole mass typically lies lower than the curvature mass. We observe a similar discrepancy when comparing quark pole masses obtained from the RG flow of the full scale dependent quark two-point function. Yet, conversely the quark pole mass, in our case $m_{\psi,\text{pole}} = 380$ MeV, lies above its curvature mass of $m_\psi = 299$ MeV which is used as an input to solve the scale dependent two-point flow equation. Thus, a discrepancy of about 38%, which in our case is also accounted for as an effect of the LPA truncation. To fully resolve this issue a higher order truncation would have to be implemented, which we attempt for the Euclidean system in the Sec. 4.2.

4.1.4. Sum rules

For deriving sum rules we need to take the $\epsilon \to 0$ limit in the definition of the full scale dependent retarded two-point function, Eq. (4.7). This limit can be performed analytically for the imaginary parts of the two point functions by rewriting the loop function using Dirac-Sokhotsky identities, Eqs.(C.14). This method is explained in detail in Ref.[87] in the context of meson spectral functions.

From the Lehmann representation of the retarded propagator

$$G_{k,\psi}(\omega, \vec{p}) = -\int_{-\infty}^{\infty} d\omega' \frac{\rho_{k,\psi}(\omega', \vec{p})}{\omega' - \omega - i\epsilon} \tag{4.36}$$

we can derive various sum rules for the spectral functions. Taking the limit $\epsilon \to 0$ and considering vanishing external momenta $\vec{p} = 0$ the Lehmann representation in Eq. (4.36) takes the form

$$G_\psi(\omega) = \int_{-\infty}^{\infty} d\omega' \, \frac{\rho_\psi(\omega')}{\omega - \omega'} \,. \tag{4.37}$$

This will be the basic form which we will derive our sum rules from by expanding for small and large ω. For large ω, this leads to

$$\begin{aligned} G_\psi(\omega) &= \int_{-\infty}^{\infty} d\omega' \, \frac{\rho_\psi(\omega')}{\omega - \omega'} = \int_{-\infty}^{\infty} d\omega' \, \frac{\rho_\psi(\omega')}{\omega} \left(1 + \frac{\omega'}{\omega} + \cdots\right) \\ &= \gamma_0 \frac{1}{\omega} \int_{-\infty}^{\infty} d\omega' \rho_\psi^{(C)}(\omega') + \frac{1}{\omega^2} \int_{-\infty}^{\infty} d\omega' \, \omega' \rho_\psi^{(B)}(\omega') \, + \, \mathcal{O}(1/\omega^3) \,, \end{aligned} \tag{4.38}$$

where we have used that $\rho_\psi^{(C)}(\omega)$ is an even function, consequently its odd moments vanish. The same of course holds for the even moments of the odd function $\rho_\psi^{(B)}(\omega)$. The leading order in the large ω expansion therefore gives

$$\int_{-\infty}^{\infty} d\omega \, \rho_\psi^{(B)}(\omega) = 0 \,, \tag{4.39}$$

$$\int_{-\infty}^{\infty} d\omega \, \rho_\psi^{(C)}(\omega) = \lim_{\omega\to\infty} \omega G_\psi^{(C)}(\omega) = \lim_{\omega\to\infty} Z^{-1}(\omega^2) \,. \tag{4.40}$$

The integral of the spectral density in a renormalizable field theory commonly diverges logarithmically. The right-hand side is then given by a formally ultraviolet divergent field renormalization constant. In our case anyway, the flow of the quark two-point function vanishes for $\omega \to \infty$. By consistency with the UV initial conditions Eq. (4.11) we can still deduce the leading-order sum rule for $\rho_{k,\psi}^{(C)}(\omega)$, which is given by

$$\int_{-\infty}^{\infty} d\omega \, \rho_{k,\psi}^{(C)}(\omega) = 1. \tag{4.41}$$

Since the quark spectral function at the UV scale Λ is given by

$$\rho_{\Lambda,\psi}^{(C)}(\omega) = Z_\Lambda(\delta(\omega - m_{\psi,\Lambda}) + \delta(\omega + m_{\psi,\Lambda})) \tag{4.42}$$

with $Z_\Lambda = 1/2$, the leading order sum rule for $\rho_{k,\psi}^{(C)}(\omega)$ in the UV is even fulfilled exactly. During the RG flow possible continuum processes open up due to interactions induced by fluctuations down to the RG scale k. This leads to the weight of the single-particle contributions being reduced in favor of contributions from the continuum. Still the k-dependence of the sum rule (4.41) throughout the flow gives us valuable insight and will be used as a consistency check for our procedure.

In general we evaluate all discussed sum rules numerically up to the UV cutoff Λ using the $\epsilon = 0$ spectral functions. For the quark spectral function in the IR this gives

$$\int_{-\Lambda}^{\Lambda} d\omega \, \rho_{k=0,\psi}^{(C)}(\omega) \approx 0.993 \,. \tag{4.43}$$

The delta functions from the single-particle contributions to the spectral function have been included explicitly, by evaluating at the scale dependent pole mass $m_{\psi,k}$

$$\rho_{k,\psi}^{(C),\text{pole}}(\omega) = Z_k(\delta(\omega - m_{\psi,k}) + \delta(\omega + m_{\psi,k})). \tag{4.44}$$

The residue Z_k is calculated d by

$$Z_k = \frac{1}{2}\left|1 - \partial_\omega B_k(\omega)|_{m_{\psi,k}}\right|^{-1}. \tag{4.45}$$

For the numerically evaluated residue we find $2Z_{k=0} \approx 0.51$ which means that roughly half of the sum rule stems from the single-(anti)particle contributions. The other half is contributed by the continuum. Since the leading order sum rule is nothing else but a normalization condition for the spectral function $\rho_{k=0,\psi}^{(C)}(\omega)$, the high degree to which it is fulfilled numerically lets us conclude that our functional RG framework is consistent, in the sense that it keeps the norm intact.

Going to next-to-leading order we find the large ω expansion in Eq. (4.38) corresponds to the energy-weighted sum rules for the quark propagator,

$$\int_{-\infty}^{\infty} d\omega\, \omega\, \rho_\psi^{(C)}(\omega) = 0\,, \tag{4.46}$$

$$\begin{aligned}\int_{-\infty}^{\infty} d\omega\, \omega\, \rho_\psi^{(B)}(\omega) &= \lim_{\omega\to\infty} \omega^2\, \frac{1}{4}\text{tr}\; G_\psi(\omega) \\ &= \lim_{\omega\to\infty} \omega^2\, G^{(B)}(\omega) = \lim_{\omega\to\infty} \frac{B(\omega)}{Z^2(\omega^2)}\,.\end{aligned} \tag{4.47}$$

By the same arguments as before, the RG flow of the two-point function vanishes in the limit $\omega \to \infty$ leaving again only the UV contributions in Eqs. (4.10) and (4.11). Using this we find for the energy-weighted sum rule

$$\int_{-\infty}^{\infty} d\omega\, \omega\, \rho_{k,\psi}^{(B)}(\omega) = \lim_{\omega\to\infty} B_k(\omega) = m_{\psi,\Lambda}\,. \tag{4.48}$$

For the parameters used here we had $m_{\psi,\Lambda} = h\sigma_0 = 299$ MeV for the quark mass in the UV[11]. We again also evaluated this energy-weighted integral over $\rho^{(B)}(\omega)$ in the IR as well, giving

$$\int_{-\infty}^{\infty} d\omega\, \omega\, \rho_{k=0,\psi}^{(B)}(\omega) = 314.9 \text{ MeV}\,. \tag{4.49}$$

The sum rule in the IR is thus slightly violated within an error of ~ 5 %.

The leading-order sum rule (4.40) for $\rho_\psi^{(C)}(\omega)$ and the next-to-leading-order sum rule (4.47) for $\rho_\psi^{(B)}(\omega)$ are completely governed by the perturbative behavior of the quark propagator only. Contributions from higher ω-orders to the quark propagator are suppressed for $\omega \to \infty$ by powers of $1/\omega^2$, since the corresponding higher moments of the spectral functions diverge in the UV. Those contributions would have to be obtained from an operator product expansion (OPE).

[11] Recall that the quark mass $m_{\psi,k}$ used in a grid approach is actually independent of the scale k.

Conversely negative moments of the quark spectral function will show a more and more rapid convergence in the UV. Assuming there do not appear any massless contributions to the quark spectral function there will be no IR divergences either.

To obtain the aforementioned negative moments of the quark spectral function one expands Eq. (4.37) in a similar way, but for small ω

$$\begin{aligned} G_\psi(\omega) &= -\int_{-\infty}^{\infty} d\omega' \, \frac{\rho_\psi(\omega')}{\omega'} \left(1 + \frac{\omega}{\omega'} + \cdots\right) \\ &= -\int_{-\infty}^{\infty} d\omega' \, \frac{\rho_\psi^{(B)}(\omega')}{\omega'} - \gamma_0 \, \omega \int_{-\infty}^{\infty} d\omega' \, \frac{\rho_\psi^{(C)}(\omega')}{\omega'^2} + \mathcal{O}(\omega^2) \,, \end{aligned} \tag{4.50}$$

where we have again used that the even moments of $\rho_\psi^{(B)}(\omega)$ and the odd moments of $\rho_\psi^{(C)}(\omega)$ vanish. This gives us for the leading-order sum rule

$$\int_{-\infty}^{\infty} d\omega \, \frac{\rho_\psi^{(B)}(\omega)}{\omega} = -G_\psi(0) = \frac{1}{B(0)} \,, \tag{4.51}$$

and for the next-to-leading-order sum rule

$$\begin{aligned} \int_{-\infty}^{\infty} d\omega \, \frac{\rho_\psi^{(C)}(\omega)}{\omega^2} &= -\lim_{\omega \to 0} \frac{1}{4} \, \frac{\text{tr} \, \big(\gamma_0 G_\psi(\omega)\big)}{\omega} \\ &= -\lim_{\omega \to 0} \frac{G_\psi^{(C)}(\omega)}{\omega} = \frac{Z(0)}{B^2(0)} \,. \end{aligned} \tag{4.52}$$

Evaluating the leading-order sum rule numerically for our spectral function $\rho_\psi^{(B)}(\omega)$ in the IR gives

$$\int_{-\infty}^{\infty} d\omega \, \frac{\rho_{k=0,\psi}^{(B)}(\omega)}{\omega} = 1.45 \cdot 10^{-3} \text{ MeV}^{-1} \,, \tag{4.53}$$

compared to the IR value of $\frac{1}{B_{k=0}(0)} \approx 1.447 \cdot 10^{-3} \text{ MeV}^{-1}$ the sum rule is in reasonable agreement with the numerically evaluated integral. For completeness the corresponding UV value is $1/B_{k=\Lambda}(0) = 1/m_{\psi,k=\Lambda} \approx 3.34 \cdot 10^{-3} \text{ MeV}^{-1}$.

In the same way we find for the next-to-leading-order sum rule for $\rho_\psi^{(C)}(\omega)$ in the IR

$$\int_{-\infty}^{\infty} d\omega \, \frac{\rho_{k=0,\psi}^{(C)}(\omega)}{\omega^2} = 4.048 \cdot 10^{-6} \text{ MeV}^{-2} \,, \tag{4.54}$$

which is also in good agreement with $\frac{Z_k(0)}{B_{k=0}^2(0)} \approx 4.058 \cdot 10^{-6} \text{ MeV}^{-2}$.

4.2. Quark Matter beyond LPA

In this section we use the chiral quark-meson model for two light quark flavors to model strongly interacting matter. We want to study the phase structure at finite temperature and chemical potential and we want to do so by adapting a truncation commonly known as LPA'. In this truncation not only the effective potential U_k is scale dependent but also flow equations for the wave function renormalization factors are solved, which modify the momentum dependent part of the respective two-point functions.

4.2.1. Going beyond LPA

RG flow of the effective potential U_k

Starting from the Euclidean Lagrangian of the quark-meson model including wave function renormalization factors $Z_{\phi,k}$ and $Z_{F,k}$

$$\begin{aligned}\mathcal{L} =& Z_{F,k}\bar{\psi}\left(\gamma_\mu\partial^\mu + h(\sigma + i\vec{\tau}\vec{\pi}\gamma^5)\right)\psi \\ &+ \frac{1}{2}Z_{\phi,k}\left(\partial_\mu\phi\right)^2 + \frac{1}{8}Y_{\phi,k}\left(\partial_\mu\phi^2\right)^2 + U_k(\phi^2) - c\sigma\,,\end{aligned} \tag{4.55}$$

where in the mesonic part of the Lagrangian we used a $O(4)$ invariant ansatz to $\mathcal{O}(\partial^2)$, which we in detail elaborate on in App. C.5. This ansatz allows for a non-vanishing vacuum expectation value of the sigma field without breaking $O(4)$ invariance in the RG flow, which in this ansatz is controlled by the term proportional to $Y_{\phi,k}$.

The RG flow of the effective potential can be calculated similarly to the LPA case, see App. C.2 for a detailed derivation, and is given by

$$\begin{aligned}\partial_k U_k =& \frac{k^4}{60\pi^2}\left[\frac{\left(1+2n_B(E_k^\sigma)\right)(5Z_{\sigma,k}+k\partial_k Z_{\sigma,k})}{E_k^\sigma Z_{\sigma,k}}\right] \\ &+ \frac{k^4}{60\pi^2}\left[\frac{(N_f^2-1)\left(1+2n_B(E_k^\pi)\right)(5Z_{\pi,k}+k\partial_k Z_{\pi,k})}{E_k^\pi Z_{\pi,k}}\right] \\ &- \frac{N_c N_f k^4}{12\pi^2}\left[\frac{\left(1-n_F(E_k^\psi-\mu)-n_F(E_k^\psi+\mu)\right)(4Z_{F,k}+k\partial_k Z_{F,k})}{E_k^\psi Z_{F,k}}\right],\end{aligned} \tag{4.56}$$

where the terms $k\partial_k Z_{(\pi,\sigma,F),k}$ are closely related to the bosonic and fermionic anomalous dimensions

$$\eta_{(\pi,\sigma,F)} = -k\partial_k \ln(Z_{(\pi,\sigma,F),k})\,. \tag{4.57}$$

In the limit $Z_{\pi,k} = Z_{\sigma,k} = Z_{F,k} = 1$ (consequently $\eta_{(\pi,\sigma,F)} = 0$) we recover the LPA flow equation from Eq. (4.2). Additionally we introduced separate wave function renormalization factors for the pion and sigma fields

$$\begin{aligned}Z_{\pi,k} &= Z_{\phi,k}\,, \\ Z_{\sigma,k} &= Z_{\pi,k} + \sigma^2 Y_{\phi,k}\,,\end{aligned} \tag{4.58}$$

as well as the LPA' scale dependent single-quasiparticle energies

$$\begin{aligned} E_k^{\pi} &= \sqrt{k^2 + \frac{m_{\pi}^2}{Z_{\pi,k}}}\,, \\ E_k^{\sigma} &= \sqrt{k^2 + \frac{m_{\sigma}^2}{Z_{\sigma,k}}}\,, \\ E_k^{\psi} &= \sqrt{k^2 + \frac{(h\sigma)^2}{Z_{F,k}^2}}\,, \end{aligned} \tag{4.59}$$

which are the straightforward generalizations of the ones in Eqs. (4.3) and the (non-renormalized) curvature masses are identical to the ones in Eqs. (4.4) and let us define the renormalized particle masses

$$\begin{aligned} M_{\pi} &= \frac{m_{\pi}}{\sqrt{Z_{\pi,k}}}\,, \\ M_{\sigma} &= \frac{m_{\sigma}}{\sqrt{Z_{\sigma,k}}}\,, \\ M_{\psi} &= \frac{m_{\psi}}{Z_{F,k}}\,. \end{aligned} \tag{4.60}$$

Flow equation for Z_π and Z_σ

From the Lagrangian in Eq. (4.55), more specifically its momentum space representation, we get the following diagrammatic flow equations for the pion and sigma two-point functions by functional differentiation of the full Wetterich equation, Eq. (2.4).

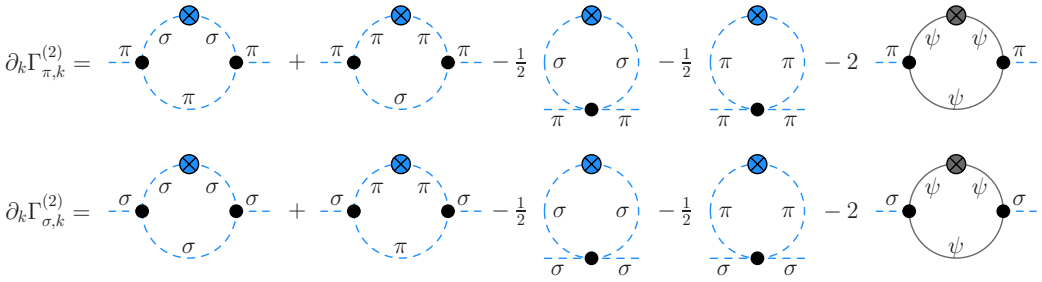

Figure 4.9.: Diagrammatic representation of the RG flow of the pion and sigma two-point functions.

From these two-point flow equations we extract the flow equations of the bosonic wave function renormalization factors by the following projection

$$\begin{aligned} \partial_k Z_{\pi,k} &= \left(\frac{1}{2} \frac{\partial^2}{\partial \vec{p}^2} \partial_k \Gamma^{(2)}_{\pi,k} \right) \Bigg|_{\vec{p}=0}\,, \\ \partial_k Z_{\sigma,k} &= \left(\frac{1}{2} \frac{\partial^2}{\partial \vec{p}^2} \partial_k \Gamma^{(2)}_{\sigma,k} \right) \Bigg|_{\vec{p}=0}\,. \end{aligned} \tag{4.61}$$

Since the tadpole diagrams in Fig. 4.9 are momentum independent they do not contribute to the flow equations of $Z_{\pi,\sigma}$.

Flow equation for $Z_{F,k}$

For the fermionic renormalization factor $Z_{F,k}$ we recover the following four mixed loops we have already seen in Sec. 4.1.

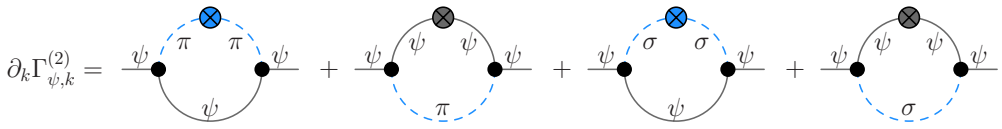

Figure 4.10.: Diagrammatic representation of the RG flow of the quark two-point function.

The flow equation for the fermionic wave function renormalization factor is obtained in a very much similar fashion than before giving

$$\partial_k Z_{F,k} = \frac{-i}{8 N_c N_f} \left(\frac{\partial^2}{\partial \vec{p}^2} \not{p} \partial_k \Gamma^{(2)}_{F,k} \right) \Bigg|_{\vec{p}=0} . \tag{4.62}$$

For the exact equations for $\partial_k Z_{(\pi,\sigma),k}$ and $\partial_k Z_{F,k}$ we want to refer the reader to App. C.2, where they are given in full length with a more detailed derivation.

4.2.2. Splitting of π and σ

Since we have chosen an $O(4)$ symmetric ansatz to $\mathcal{O}(\partial^2)$ for the bosonic part of our action, the question arises of how to include the pair of bosonic renormalization factors in our iteration procedure, c.f. Sec. 3.4, to solve the closed system of equations for the effective potential U_k and the renormalization factors $\partial_k Z_{(\pi,\sigma),k}$ without breaking $O(4)$-symmetry explicitly. It becomes very clear from the definition of $Z_{\pi,k}$ and $Z_{\sigma,k}$ that is not feasible to solve both of them field-independently at the IR minimum of the potential σ_0.

$$\begin{aligned} Z_{\pi,k} &= Z_{\phi,k} \ , \\ Z_{\sigma,k} &= Z_{\pi,k} + \sigma_0^2 Y_{\phi,k} \ , \end{aligned} \tag{4.63}$$

Choosing $Z_{\pi,k}$ field-independent would right away lead to a finite splitting between $Z_{\pi,k}$ and $Z_{\sigma,k}$ consequently breaking $O(4)$-symmetry explicitly already in the UV, which is solely due to the finite value of σ_0.

On the other hand solving $Z_{\pi,k}$ field-independently and considering the scale dependent minimum $\sigma_{0,k}$ when calculating $Z_{\sigma,k}$ one does not break $O(4)$-symmetry until the effective potential develops a non trivial minimum in the RG flow. This is shown in Fig.4.11 where we plotted solutions for both $Z_{\pi,k}$ and $Z_{\sigma,k}$ as a function of the normalized scale $\frac{k}{\Lambda}$.

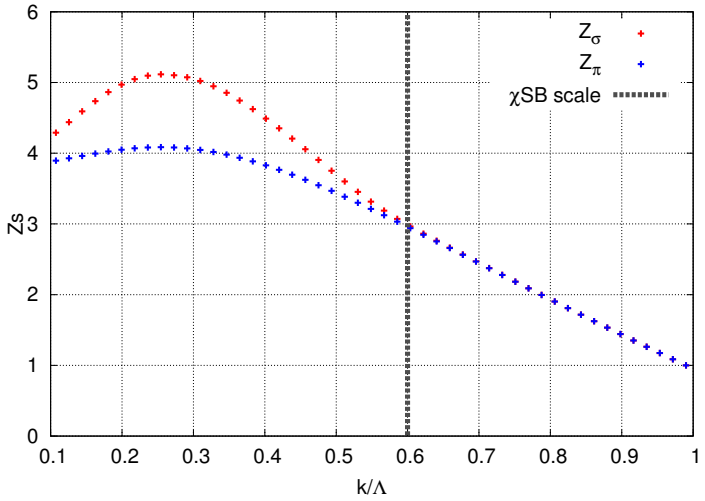

Figure 4.11.: Wave function renormalization factors $Z_{\sigma,k}$ and $Z_{\pi,k}$ as a function of the normalized scale $\frac{k}{\Lambda}$.

It can clearly be seen that $Z_{\pi,k}$ and $Z_{\sigma,k}$ remain degenerate from the UV up until a chiral symmetry breaking scale of about 600 MeV. This behavior resembles what we have seen in Fig. 4.2 in Sec. 4.1, which boils down to the two situations being very similar in the sense that they both tackle the question of how to solve two-point flow equations with the scale dependent effective potential as an input.

Going further beneath the chiral symmetry breaking scale $Z_{\pi,k}$ and $Z_{\sigma,k}$ develop a clear splitting which stays finite also in the IR. In the following we want to study

this model at finite temperature and chemical potential in two different truncations. Truncation I considers the scale dependence of the potential U_k and the wave function renormalization factors $Z_{\pi,k}$, $Z_{\sigma,k}$ and $Z_{F,k}$. In truncation II we will set $Z_{F,k} = \text{const} = 1$.

4.2.3. Truncation I

In Fig. 4.12 we can see the phase diagram of the chiral quark-meson model where aside from a scale dependent potential U_k the wave function renormalization factors $Z_{\pi,k}$, $Z_{\sigma,k}$ and $Z_{F,k}$ are included. We have plotted the renormalized chiral condensate $\tilde{\sigma}$ as function of temperature T and chemical potential μ. The chiral condensate is plotted as a heat map where the yellow sector corresponds to broken chiral symmetry whereas the blue sector indicates chiral symmetry restoration.

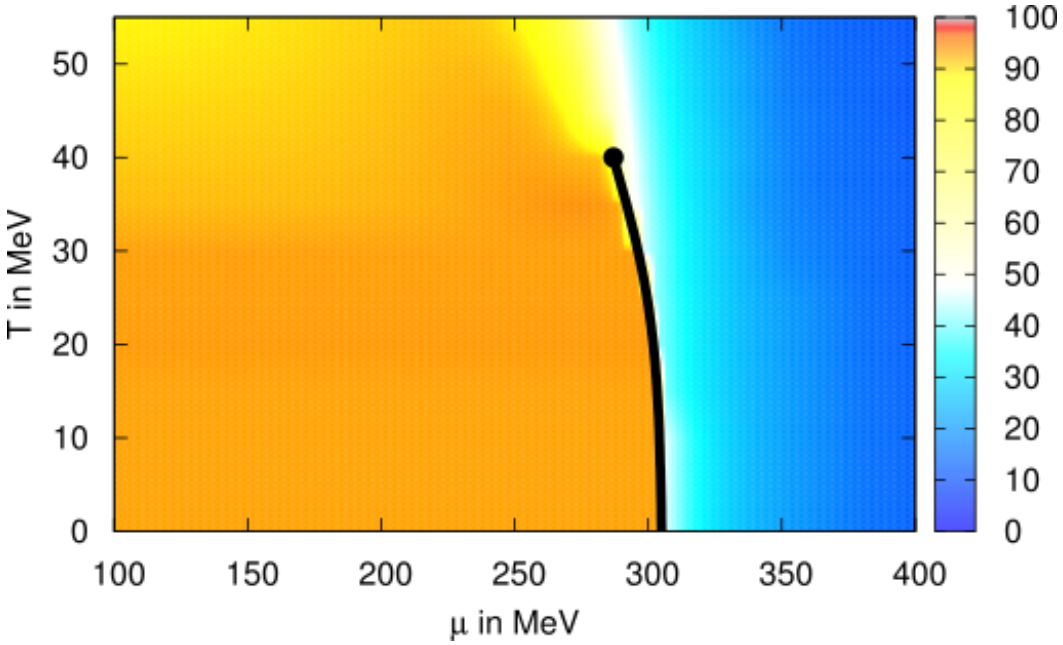

Figure 4.12.: Phase diagram including $Z_{\pi,k}$, $Z_{\sigma,k}$ and $Z_{F,k}$. Plotted is the chiral condensate $\tilde{\sigma}_0$ as a function of temperature T and chemical potential μ (color contour). Also shown is the first order chiral critical line ending in an critical endpoint (black solid point).

Also shown in Fig. 4.12 is the first order chiral critical line (black line) ending in a critical endpoint indicated by a solid black point. We find slightly unbound quark matter in this case, since the renormalized quark mass was fixed to reproduce $M_\psi = 300$ MeV and the first order critical line crosses the μ-axis at about 306 MeV. The critical endpoint lets us read off values for the critical temperature and chemical potential, which in this case are $T_c = 40$ MeV and $\mu_c = 280$ MeV. These values should only be understood as a rough estimate, since this study is more aimed at exploring the phase structure, form and existence of a critical line beyond LPA, than giving quantitative predictions of the CEP's position. In Fig. 4.13 we show the corresponding solutions for the wave function renormalization factors $Z_{\pi,k}$, $Z_{\sigma,k}$

and $Z_{F,k}$ as a function of the chemical potential μ at $T = 0$.

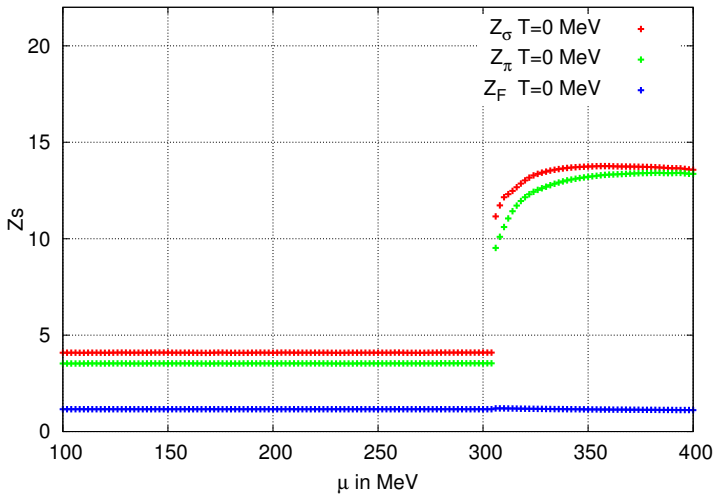

Figure 4.13.: Solutions of $Z_{\pi,k}$, $Z_{\sigma,k}$ and $Z_{F,k}$ as a function of the chemical potential μ at $T = 0$ in the IR.

In the vacuum at $T = \mu = 0$ the wave function renormalization factors each start with their respective vacuum values and remain constant until the first order phase transition, reflecting the Silver-Blaze property of QCD, cf. App. B.2. The bosonic renormalization factors $Z_{\pi,k}$ and $Z_{\sigma,k}$ show a considerable increase after the first order phase transition increasing by more than a factor of two. In the large μ regime they become degenerate again which reflects the way we include the splitting between $Z_{\pi,k}$ and $Z_{\sigma,k}$, cf. Eq. (4.63), which is proportional to the chiral condensate, hence vanishes towards chiral restoration giving $Z_{\pi,k} = Z_{\sigma,k}$ for large μ. The fermionic renormalization factor $Z_{F,k}$ is almost constant throughout at roughly $Z_{F,k} = 1.1$, for large μ slowly approaching $Z_{F,k} = 1$, which makes it a reasonable approximation to set it to $Z_{F,k} = \text{const} = 1$ from the beginning. We will now study the model in this truncation, and also apply the same approximation later on in the parity-doublet model beyond LPA, see Sec. 5.2.4.

4.2.4. Truncation II

In Fig. 4.14 we show the phase diagram of the chiral quark-meson model similar to Fig. 4.12, this time considering scale dependence of $Z_{\pi,k}$, $Z_{\sigma,k}$ only. Plotted is, as before, the renormalized chiral condensate $\tilde{\sigma}$ as a function of temperature T and chemical potential μ, where the heat map corresponds to the magnitude of the chiral condensate, yellow standing for large $\tilde{\sigma}$ (chirally broken phase) and blue for small $\tilde{\sigma}$, hence the chirally restored phase. We again find unbound quark matter, in this case the first order chiral critical line starts on the μ-axis at about 340 MeV.

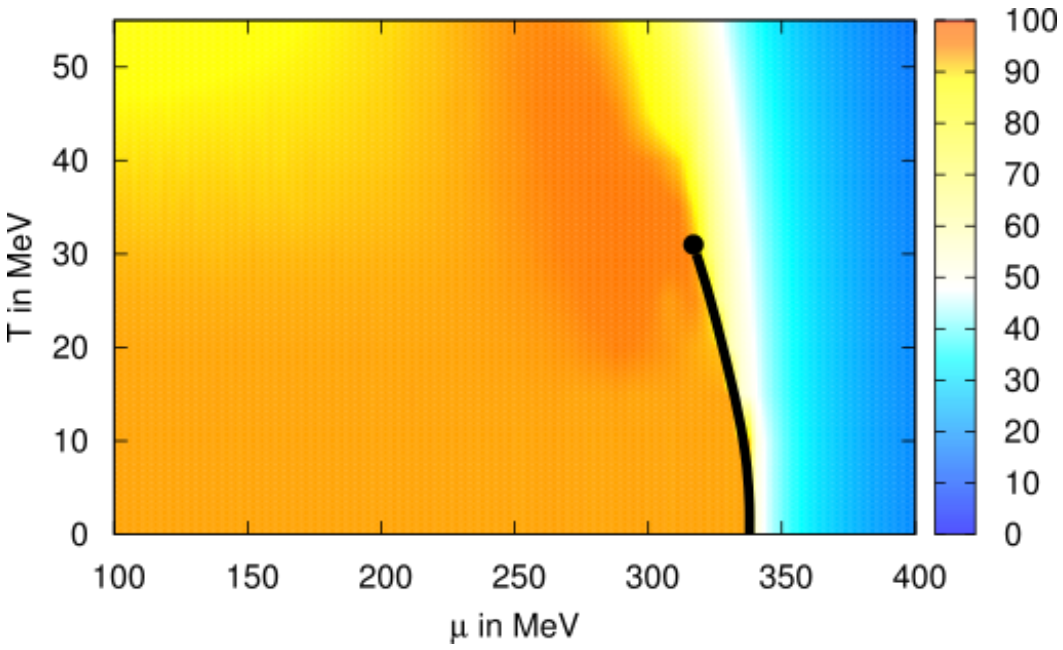

Figure 4.14.: Phase diagram including $Z_{\pi,k}$, $Z_{\sigma,k}$ and $Z_{F,k} = \text{const} = 1$. Plotted is the chiral condensate $\tilde{\sigma}_0$ as a function of temperature T and chemical potential μ (color contour). Also shown is the first order chiral critical line ending in an critical endpoint (black solid point).

The critical endpoint is located $T_c = 30$ MeV and $\mu_c = 310$ MeV, where these values are again only to be understood as a qualitative prognosis. In Fig. 4.15 we plotted the wave function renormalization factors $Z_{\pi,k}$, $Z_{\sigma,k}$ and $Z_{F,k}$ as function of the chemical potential μ at vanishing temperature. $Z_{F,k} = \text{const} = 1$ is just shown as a reference. As before, $Z_{\pi,k}$ and $Z_{\sigma,k}$ start with their respective vacuum values (with $Z_{\pi,k} < Z_{\sigma,k}$) and remain constant up until the first order phase transition, again consistent with the Silver-Blaze property. After the first order transition both $Z_{\pi,k}$ and $Z_{\sigma,k}$ (discontinuously) increase considerably and become degenerate for large μ.

The situation changes for higher temperatures, as shown in Fig. 4.16, where we plotted the corresponding solutions for $T = 55$ MeV, hence beyond the critical point. It can be seen, that the μ dependence gets smoothened making the discontinuity become a smooth crossover. Still at large mu $Z_{\pi,k}$ and $Z_{\sigma,k}$ become degenerate, again consistent with chiral symmetry restoration. Interestingly for $T = 55$ MeV $Z_{\pi,k} > Z_{\sigma,k}$ in the vacuum and $Z_{\sigma,k}$ becomes larger than $Z_{\pi,k}$ only from about 180 MeV on.

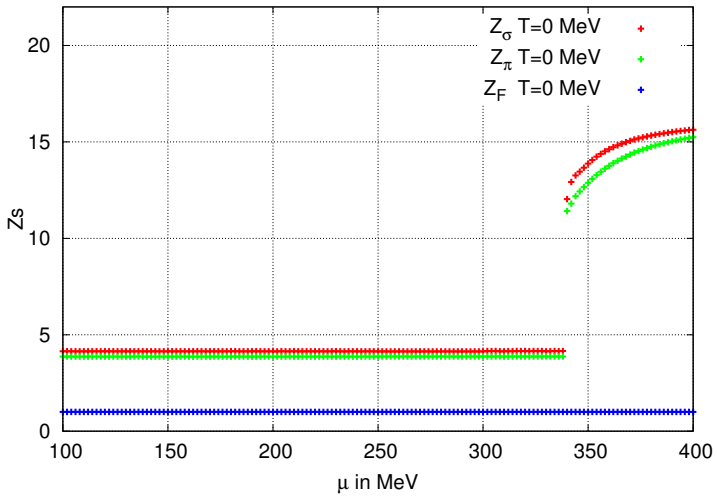

Figure 4.15.: Solutions of $Z_{\pi,k}$, $Z_{\sigma,k}$ and $Z_{F,k}$ = const = 1 as a function of the chemical potential μ at $T = 0$.

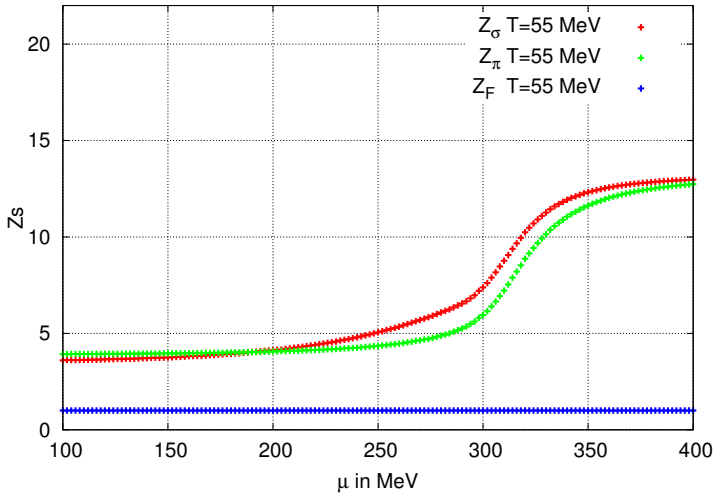

Figure 4.16.: Solutions of $Z_{\pi,k}$, $Z_{\sigma,k}$ and $Z_{F,k}$ = const = 1 as a function of the chemical potential μ at $T = 55$ MeV.

We now want to come to the μ-dependence of the masses of the pion and sigma meson, as well as the quark. In Fig. 4.17 the renormalized masses are shown as a function of the chemical potential μ. The quark mass is fixed to reproduce a value of $M_\psi = 300$ MeV in the vacuum. Furthermore we considered a physical pion mass of $M_\pi = 140$ MeV and a mass of the sigma meson of $M_\sigma = 500$ MeV. The quark mass remains constant up to the first order phase transition where it discontinuously drops to a value of ~ 100 MeV and then tends towards $M_\psi \to 0$ as chiral symmetry gets restored for high μ.

Similar to the behavior of the quark, the mesons remain constant until the first order chiral phase transition, yet again in agreement with the Silver-Blaze property. After the first order phase transition the sigma mass discontinuously jumps below the pion mass and towards higher μ approaches the pion mass from below until they eventually become degenerate, as expected from chiral partners in the chirally restored phase.

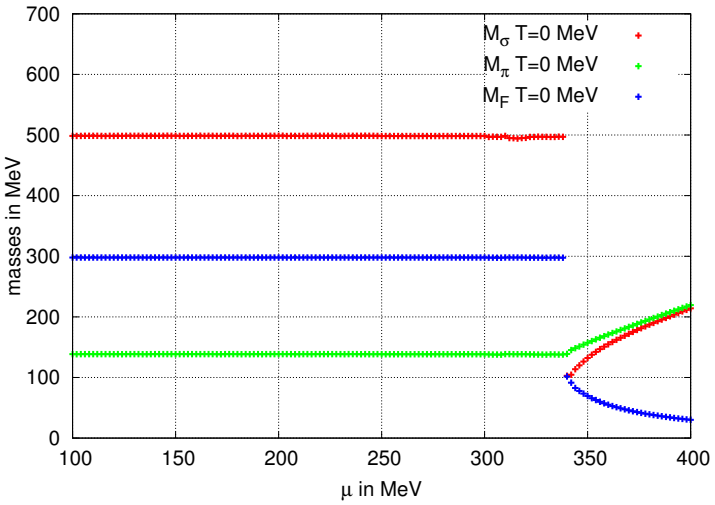

Figure 4.17.: Masses of the mesons (σ, π) and the quark as a function of chemical potential μ at $T = 0$.

For a higher temperature of $T = 55$ MeV beyond the critical temperature of $T_c = 30$ MeV, we plotted the meson and quark masses as a function of the chemical potential μ in Fig. 4.18. In analogy to Fig. 4.16, it can be observed that the inclusion of finite temperatures tends to smoothen all discontinuities rendering all observables to have a continuous μ-dependence. At $\mu = 0$ the quark mass still starts with its vacuum value of $M_\psi = 300$ MeV, but directly begins decreasing and continuously approaches $M_\psi \to 0$ for large μ.

For the meson masses M_π and M_σ the situation is very similar. Both start with their respective vacuum values $M_\pi = 140$ MeV and $M_\sigma = 500$ MeV. While the pion mass still remains almost constant up to a value of $\mu \approx 300$ MeV, where it starts increasing continuously, the sigma meson begins to decrease already starting from $\mu = 0$. At the same value of $\mu \approx 300$ MeV M_σ becomes smaller as M_π and from then on approaches the pion mass from below giving $M_\sigma \to M_\pi$ for large μ, again consistent with the sigma meson and the pion being chiral partners, which become

degenerate in the chirally restored phase.

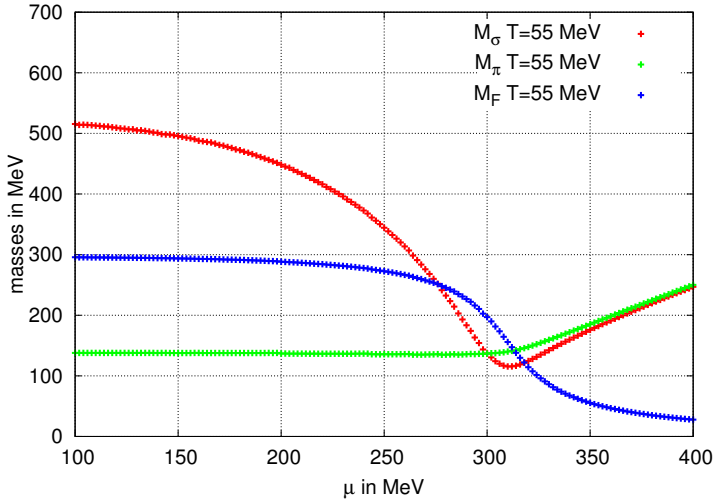

Figure 4.18.: Masses of the mesons (σ, π) and the quark as a function of chemical potential μ at $T = 55$ MeV.

Now coming back to the discussion from Sec. 3.2.2 about slopes of critical lines, we want to take another look at both Fig. 4.12 and Fig. 4.14.

Revisiting the Clausius-Clapeyron equation [174] in the following form

$$\frac{\mathrm{d}T_c}{\mathrm{d}\mu_c} = -\frac{\Delta n}{\Delta s}\,, \tag{4.64}$$

which connects the slope of the critical line with the change in number density Δn and in entropy density Δs. Since we have an increase in the number density $\Delta n > 0$ in the first order chiral transition and the entropy density per particle is expected to increase, for an order-disorder transition, also the discontinuity in the entropy density is expected to be positive. Anyway, here we find $\Delta s > 0$ directly from the slope of the critical lines in Figs. 4.12 and 4.14, which actually makes it irrelevant to distinguish between entropy per particle and entropy density in this case. This is the typical behavior seen in mean-field studies of the chiral first order line [35] and in contrast to FRG calculations in local potential approximation which typically give $\frac{dT_c}{d\mu_c} > 0$, hence $\Delta s < 0$, see e.g. [73, 75, 76, 82].

This lets us conclude that in the chiral quark-meson model with two light quark flavors in a beyond LPA truncation as applied here, the inclusion of the scale dependent bosonic wave function renormalization factors $Z_{\pi,k}$ and $Z_{\sigma,k}$[12] has the tendency to give critical first order lines with $\frac{dT_c}{d\mu_c} < 0$.

[12] Since the results for $\frac{dT_c}{d\mu_c}$ are identical in truncation II (with $Z_{F,k} = \text{const} = 1$), $Z_{F,k}$ does not seem to be of importance for this effect.

5

Nuclear Matter Results

After having phenomenologically motivated and constructed the parity-doublet (or mirror) model in Sec. 3.1.4, we want to focus on its FRG treatment in the following. We will briefly go through the needed steps to derive the RG flow equation for the local potential U_k and afterwards present a few results.

5.1. Fluctuations in the Parity-doublet Model

The starting point of the following considerations is the fermionic part of the Euclidean Lagrangian of the parity-doublet model, cf. Eq.(3.15),

$$\begin{aligned}\mathcal{L}_F =&\bar{N}_1\big(\partial\!\!\!/ - \mu_B\gamma_0 + h_1(\sigma + \mathrm{i}\gamma_5\vec{\tau}\vec{\pi}) + \mathrm{i}h_v\gamma^\mu\omega_\mu\big)N_1 \\ &+ \bar{N}_2\big(\partial\!\!\!/ - \mu_B\gamma_0 + h_2(\sigma - \mathrm{i}\gamma_5\vec{\tau}\vec{\pi}) + \mathrm{i}h_v\gamma^\mu\omega_\mu\big)N_2 \\ &+ m_0(\bar{N}_1\gamma_5 N_2 - \bar{N}_2\gamma_5 N_1).\end{aligned} \tag{5.1}$$

For calculating the fermionic flow of the effective potential we set the bosonic fields to their expectation values, leading to the following inverse baryon propagator in momentum space

$$S_0^{-1} = \begin{pmatrix} -\mathrm{i}p\!\!\!/ + h_1\sigma - \tilde{\mu}_B & m_0\gamma_5 \\ -m_0\gamma_5 & -\mathrm{i}p\!\!\!/ + h_2\sigma - \tilde{\mu}_B \end{pmatrix}. \tag{5.2}$$

Here we assumed vanishing spatial expectation values for the ω-field, as one would expect in the rest-frame of an isotropic thermal medium. Furthermore we introduced a shifted baryon chemical potential $\tilde{\mu}_B = \mu_B - \mathrm{i}h_v\omega_0$ which takes a non-vanishing expectation value of ω_0 into account. To calculate the thermodynamic grand potential one has to evaluate the following determinant

$$\begin{aligned}\det\gamma_0 S_0^{-1} =& \big[m_0^4 + 2m_0^2(-(\mu + \mathrm{i}p_0)^2 + \vec{p}^2 + h_1h_2\sigma^2) \\ &+((\tilde{\mu}_B + \mathrm{i}p_0)^2 - \vec{p}^2 - h_1^2\sigma^2)((\tilde{\mu}_B + \mathrm{i}p_0)^2 - \vec{p}^2 - h_2^2\sigma^2)\big]^2 \\ \equiv& \left((p_0 - \mathrm{i}\tilde{\mu}_B)^4 + \alpha_p\,(p_0 - \mathrm{i}\tilde{\mu}_B)^2 + \beta_p\right)^2\end{aligned} \tag{5.3}$$

with

$$\begin{aligned}\alpha_p &= 2m_0^2 + 2\vec{p}^{\,2} + h_1^2\sigma^2 + h_2^2\sigma^2,\\ \beta_p &= \frac{\alpha_p^2}{4} - \frac{1}{4}(h_1 - h_2)^2\sigma^2(4m_0^2 + (h_1 + h_2)^2\sigma^2)\,.\end{aligned} \tag{5.4}$$

This determinant's zeros $m_\pm = \mathrm{i}p_0$ (at vanishing 3-momentum $\vec{p} = 0$ and chemical potential $\tilde{\mu}_B = 0$) give the mean-field baryon masses, which look like

$$m_\pm = \frac{1}{2}\left(\pm(h_1 - h_2)\sigma + \sqrt{4m_0^2 + (h_1 + h_2)^2\sigma^2}\right)\,. \tag{5.5}$$

In the case of restored chiral symmetry $\sigma = 0$ the baryons become degenerate with mass m_0, as expected. Now the mean-field grand potential can be evaluated for a sharp momentum cutoff, leading to

$$\Omega = \Omega_q + V_\mathrm{M} = -T\sum_{p_0}\int\frac{\mathrm{d}^3p}{(2\pi)^3}\mathrm{Tr}\log S_0^{-1} + V_\mathrm{M} \tag{5.6}$$

with

$$\begin{aligned}\Omega_q &= -2N_f\sum_\pm\int\frac{\mathrm{d}^3p}{(2\pi)^3}\log\left(\cosh\left(\frac{\epsilon_p^\pm + \tilde{\mu}_B}{2T}\right)\right)\\ &= -2N_f\sum_\pm\int\frac{\mathrm{d}^3p}{(2\pi)^3}\left[\frac{|\epsilon_p^\pm + \tilde{\mu}_B|}{2} + \frac{|\epsilon_p^\pm - \tilde{\mu}_B|}{2}\right.\\ &\left. + T\log\left(1 + e^{-\frac{|\epsilon_p^\pm + \tilde{\mu}_B|}{T}}\right) + T\log\left(1 + e^{-\frac{|\epsilon_p^\pm - \tilde{\mu}_B|}{T}}\right)\right].\end{aligned} \tag{5.7}$$

Here the single-(quasi)particle energies of the form

$$\epsilon_p^\pm = \sqrt{\frac{\alpha_p}{2} \pm \sqrt{\frac{\alpha_p^2}{4} - \beta_p}}\,, \tag{5.8}$$

were used. Setting $m_0 = 0$ one recovers $\epsilon_p^\pm = \sqrt{\vec{p}^{\,2} + m_\pm^2}$, the usual expression for a single fermion species. Furthermore, in this case the expression for the fermionic grand potential also reduces to a sum of two quark-meson models, with $m_+ = h_1\sigma$ and $m_- = h_2\sigma$ being the respective Yukawa-like masses. N_f in this case represents the number of isodoublets under consideration, namely one nucleon isodoublet for protons and neutrons (p, n) and another one for their heavier parity partners, hence $N_f = 2$. Calculations in the mean-field approximation can in general be improved by including both fermionic and mesonic fluctuations, which is done here within the framework of the FRG.

Revisiting Sec. 2.3, we saw that the evolution of the effective average action Γ_k with the RG scale k is described by the exact flow equation

$$\partial_k\Gamma_k = \tfrac{1}{2}\,\mathrm{Tr}\left[\frac{1}{\Gamma_k^{(2)} + R_k}\partial_k R_k\right], \tag{5.9}$$

where, as before, $\Gamma_k^{(2)}$ is the second functional derivative of the effective average action and the trace runs over all inner indices and includes a momentum integration. For evaluating the right-hand side of Eq.(5.9) we chose an ansatz in local potential approximation (LPA), where only the effective potential U_k is scale-dependent.

$$\Gamma_k = \mathcal{L}|_{U \to U_k} \tag{5.10}$$

Starting with a bare potential as given in Eq. (3.17), the flow of the potential can be split up into a fermionic and a bosonic part

$$\partial_k U_k = \partial_k U_{k,F} + \partial_k U_{k,B} \,. \tag{5.11}$$

For both the fermionic and the bosonic contributions to the RG flow we used the $3d$-analogues of the LPA-optimized regulators, cf. [183]. This regulator choice guarantees, that the arising Matsubara sums can be evaluated analytically. The fermionic part can then be obtained, similar to the quark-meson-diquark model for two-color QCD in [75],

$$\begin{aligned}
\partial_k U_{k,F} &= -\frac{N_f k^4}{6\pi^2} \sum_{\pm} \frac{\epsilon_k^{\pm}(1 - n_F(\epsilon_k^{\mp} + \tilde{\mu}_B)) - \epsilon_k^{\pm} n_F(\epsilon_k^{\mp} + \tilde{\mu}_B)}{\epsilon_k^{\mp} \epsilon_k^{\pm}} \\
&= -\frac{N_f k^4}{6\pi^2} \sum_{\pm} \left[\frac{2(k^2 + m_0^2 - \epsilon_k^{\pm 2}) + (h_1^2 + h_2^2)\sigma^2}{(\epsilon_k^{\mp 2} - \epsilon_k^{\pm 2})\epsilon_k^{\pm}} \right. \\
&\left. \times \left(\tanh\left(\tfrac{\epsilon_k^{\pm} + \tilde{\mu}_B}{2T} \right) + \tanh\left(\tfrac{\epsilon_k^{\pm} - \tilde{\mu}_B}{2T} \right) \right) \right],
\end{aligned} \tag{5.12}$$

where in the first line the fermionic occupation numbers $n_F(E)$ appear, see App. C.1.1 for details. We also again made use of single-quasiparticle energies $\epsilon_k^{\pm}$, as defined in Eq. (5.8), here evaluated at $\vec{p}^2 = k^2$. Analogous to the mean-field approximation, we recover the sum of two quark-meson model RG flow contributions to the local potential, when setting $m_0 = 0$ in Eq. (5.12), compare e.g. [73]. The bosonic contribution is indeed identical to the corresponding expression in 2 flavor chiral quark-meson models in LPA [73], again using the $3d$ LPA-optimized Litim regulator, giving

$$\begin{aligned}
\partial_k U_{k,B} &= \frac{k^4}{12\pi^2} \left[\frac{1 + 2n_B(\epsilon_k^{\sigma})}{\epsilon_k^{\sigma}} + \frac{(N_f^2 - 1)(1 + 2n_B(\epsilon_k^{\pi}))}{\epsilon_k^{\pi}} \right] \\
&= \frac{k^4}{12\pi^2} \left[\frac{1}{\epsilon_k^{\sigma}} \coth\left(\frac{\epsilon_k^{\sigma}}{2T} \right) + \frac{3}{\epsilon_k^{\pi}} \coth\left(\frac{\epsilon_k^{\pi}}{2T} \right) \right],
\end{aligned} \tag{5.13}$$

where this time bosonic occupation numbers appear, and we again made use of the mesonic single-quasiparticle energies

$$\begin{aligned}
\epsilon_k^{\sigma} &= \sqrt{k^2 + m_{\sigma}^2} \,, \\
\epsilon_k^{\pi} &= \sqrt{k^2 + m_{\pi}^2} \,,
\end{aligned} \tag{5.14}$$

and the respective curvature masses

$$\begin{aligned}
m_{\sigma} &= \sqrt{2U_k' + 4U_k'' \phi^2} \,, \\
m_{\pi} &= \sqrt{2U_k'} \,,
\end{aligned} \tag{5.15}$$

which are calculated from the derivatives of the effective potential $U_k' = \frac{\partial}{\partial\phi^2}U_k$ and $U_k'' = \frac{\partial^2}{\partial\phi^2\partial\phi^2}U_k$ with respect to the invariant ϕ^2.

5.2. Parity-doublet model in LPA

Let us first present results for the parity-doublet model in the extended mean-field approximation, where only the fermionic contribution to the RG-flow of the effective potential is taken into account.

The minus sign of the fermionic loop in the flow equation, cf. Eq. (2.67), has the general feature of always driving the σ-field away from zero towards the broken phase. In contrast mesonic fluctuations have the tendency to drive the system towards symmetry restoration. This is why in purely mesonic $O(n)$-models [84] the UV potential has to be fixed to start deep in the broken phase in order to end up at $\bar{\sigma}_0 = f_\pi$ in the IR. In quark-meson models the UV potential typically starts out in the restored phase and the fermionic fluctuations govern the IR potential to end up at $\bar{\sigma}_0 = f_\pi$.

In the parity-doublet model, however, the fermionic contribution to the flow as compared to a quark-meson model is smaller and therefore the integrated fermionic flow decreases more quickly. This is due to the nucleon masses starting out with a comparatively large invariant mass term m_0 and further increase with σ, cf. Eq. (5.5), through contributions generated during the flow. Starting the flow at a UV cutoff $\Lambda = 1$ GeV the nucleon fluctuations get suppressed rapidly with an emerging non-trivial minimum in the σ-direction. Therefore we start the flow with a small negative mass term already in the UV potential, i.e. just in the broken phase. With a fixed IR minimum of the effective potential at $\bar{\sigma}_0 = f_\pi$ we found the need of introducing a small $\lambda_6\phi^6$ term in the UV potential in order to get sufficiently small curvature masses for the σ meson of around 500 MeV. The introduction of the λ_6 term can be avoided by starting at a higher UV scale Λ, which we have verified.

5.2.1. Extended mean-field results at finite μ and $T = 0$

Our eMF results for the chiral condensate $\bar{\sigma}$ at $T = 0$ as a function of baryon chemical potential μ_B for $m_0 = 820$ MeV in the vicinity of the liquid-gas transition of nuclear matter are shown in Fig. 5.1.

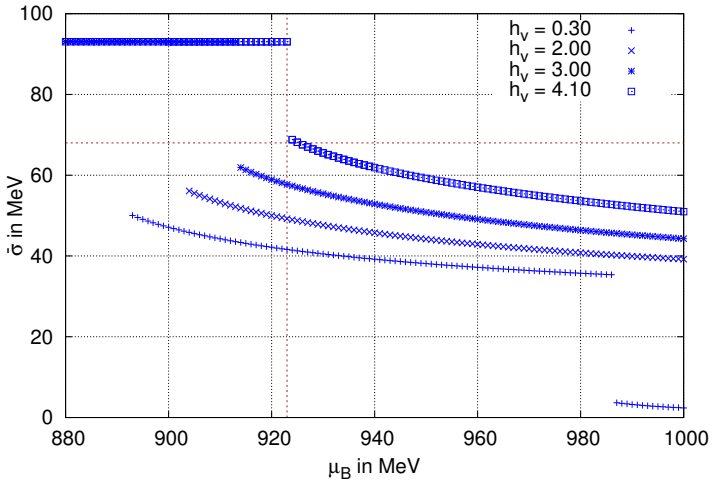

Figure 5.1.: The chiral condensate for $m_0 = 820$ MeV as a function of μ_B is shown for different values of the vector meson coupling h_v focussing on the nuclear matter transition only. Larger values of h_v shift the nuclear matter transition towards larger chemical potentials. Realistic values for the binding energy per nucleon (vertical dotted line), in-medium condensate (horizontal dotted line) and saturation density of nuclear matter are reproduced for $h_v = 4.1$.

The different curves correspond to different values of the vector coupling h_v. It can be seen that the discontinuity of $\bar{\sigma}(\mu_B)$, i.e. the position of the nuclear matter transition gets shifted to larger μ_B with increasing h_v as expected from the repulsive nature of the isoscalar vector meson ω. The red, dashed, horizontal and vertical lines indicate the position of the realistic in-medium condensate $\bar{\sigma}(n_0) \simeq 69$ MeV and a critical chemical potential $\mu_B^c = (939 - 16)$ MeV$= 923$ MeV which corresponds to a nuclear matter saturation density of $n_0 \simeq 0.16$ fm^{-3} and a nucleon-sigma term of $\sigma_N \simeq 36$ MeV, cf. Eq. (3.22). These nuclear matter properties are realized for the parameter set with $h_v = 4.10$.

To get a better understanding of how the first order transition gets shifted by including a repulsive vector meson it is worthwhile to take a look at the corresponding solutions of the ω-gap equation, discussed in detail in App. B.3.

In Fig. 5.2 the solutions (as resulting shifts in chemical potential) $\Delta\mu_B = \mathrm{i}h_v\bar{\omega}_0$ are shown as a function of $\bar{\sigma}$. The solutions of the ω-gap equation are shown for different values of h_v and were all calculated at $\mu_B = 892$ MeV corresponding to the unshifted nuclear matter transition.

In order to achieve a shift of the first order transition in $\bar{\sigma}(\mu_B)$ it is necessary to have a non-zero $\Delta\mu_B = \mathrm{i}h_v\bar{\omega}_0$ for $\bar{\sigma}$ values larger than the in-medium condensate at

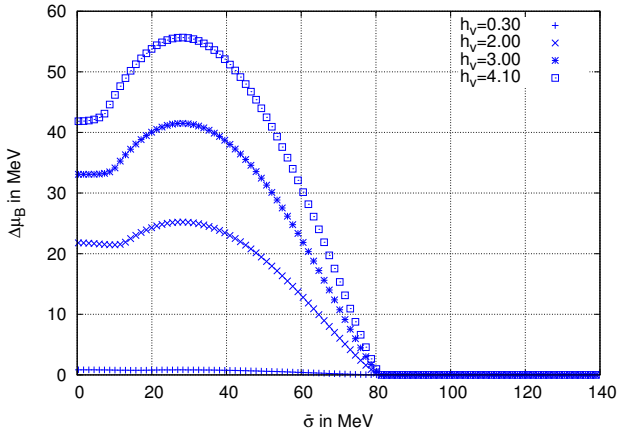

Figure 5.2.: Solutions $\Delta\mu_B = \mathrm{i}h_v\bar{\omega}_0$ of the ω-gap equation at $m_0 = 820$ MeV and $\mu_B = 892$ MeV. $\Delta\mu_B$ is shown as a function of the chiral condensate $\bar{\sigma}$ and for different values of the vector meson coupling h_v.

saturation density, $\bar{\sigma}(n_0)$. This leads to a shift towards larger μ_B^c and at the same time weakens the first order transition. For the parameters used in Fig. 5.1 $\bar{\sigma}(n_0)$ is between 50 MeV and 69 MeV. We would also like to point out that the bifurcation point in the solutions of the ω-gap equation stays put at $\bar{\sigma}_b \simeq 80$ MeV, meaning $\Delta\mu_B(\bar{\sigma}(n_0))$ stays zero for $\bar{\sigma} \geq \bar{\sigma}_b$, independent of the size of the vector coupling h_v. This makes it impossible to shift μ_B^c any further as soon as $\bar{\sigma}(n_0)$ reaches $\bar{\sigma}_b$.

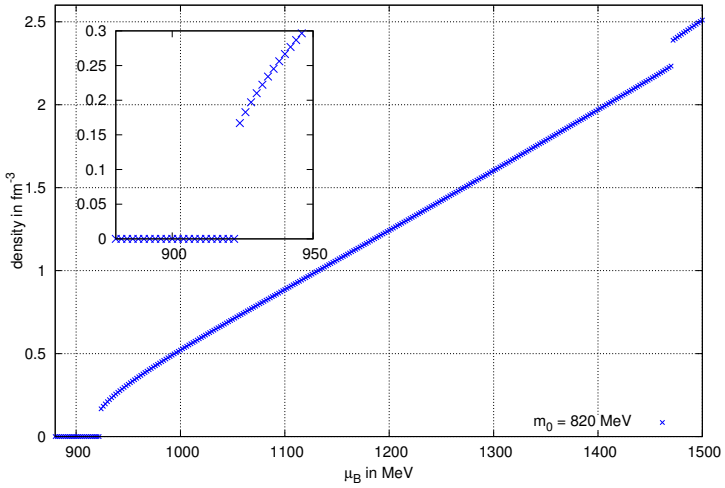

Figure 5.3.: The nucleon number density for $m_0 = 820$ MeV and $h_v = 4.1$ as a function of μ_B. The density has a discontinuity at $\mu_B^c = 923$ MeV jumping to a density of $n(\mu_B^c) = n_0 \simeq 0.16$ fm^{-3} (see insert).

As explained in detail in in App. (B.3) the solutions of the ω gap equation give convenient access to the baryon number density $n(\mu_B)$, cf. Eq. (B.14). In Fig. 5.3

we show the baryon number density as a function of baryon chemical potential for the parameter set $m_0 = 820$ MeV and $h_v = 4.10$, that reproduces nuclear matter properties to satisfying level in our eMF description. It can be observed, that at first the density remains zero until it jumps discontinuously to $n_0 \simeq 0.16$ fm^{-3}. This discontinuity occurs at $\mu_B^c = 939 - 16 = 923$ MeV, giving a correct description of the nuclear matter transition from the vacuum ($n_B = 0$) to phenomenologically correct nuclear matter. In contrast to Fig. 5.1 we now also show a second discontinuity in

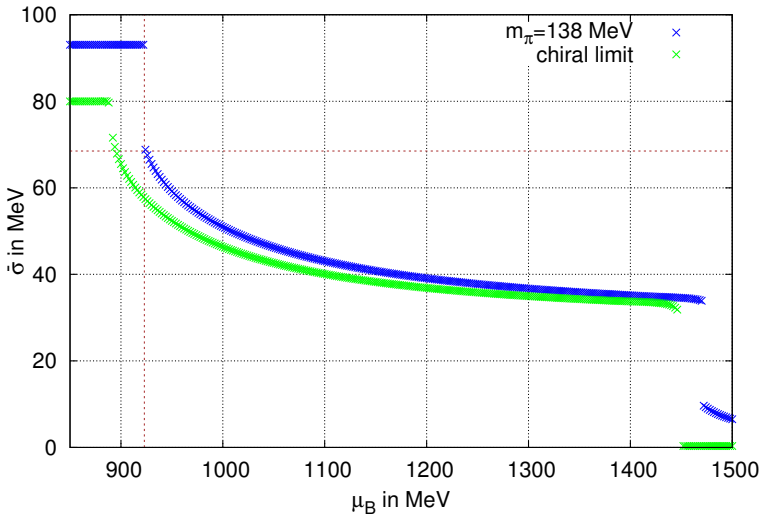

Figure 5.4.: The chiral condensate as a function of μ_B for both the nuclear matter and chiral phase transition of the model. Results for physical pion mass and in the chiral limit are shown.

the high density regime at about $\mu_B \simeq 1472$ MeV. Since this transition occurs at roughly 13.7 times nuclear matter saturation density it is hardly relevant for the equation of state of nuclear matter in neutron stars. As will be seen in Sec. 5.2.2, when including mesonic fluctuations in the FRG flow, both transitions seen in the parity-doublet model will be brought closer together thus bringing the second transition into a more relevant region.

Furthermore, studying the nature of the two transitions leads to identifying the first transition, as already mentioned, as the liquid-gas transition of nuclear matter, whereas the second transition within the high-density phase is indeed identified as the chiral transition of the model.

This is demonstrated in detail in Fig. 5.4 which again shows the chiral condensate as a function of the baryon chemical μ_B potential, similar to Fig. 5.1, but over a larger interval in chemical potential. The blue curve shows the chiral condensate for the parameter set which reproduces nuclear matter properties with a pion mass fixed to its physical value of $m_\pi = 138$ MeV. The green line corresponds to solutions using the exact same parameters but in the chiral limit, meaning that the explicit chiral symmetry-breaking term c was taken to zero, resulting in a vanishing pion mass. The fact that for the second transition the chiral condensate drops to exactly

zero in the chiral limit, whereas after the first transition the in-medium condensate still remains finite, lets us identify the second transition as the chiral first-order phase transition of the model.

Moreover, we can extract the nuclear matter properties of the transition in the chiral limit, $\bar{\sigma}_0 \simeq 80$ MeV, $E_b \simeq 47$ MeV, $n_0 \simeq 0.064$ fm^{-3} and $\bar{\sigma}(n_0) \simeq 0.89\,\bar{\sigma}_0$.

The corresponding masses of the nucleons and their respective parity partners are shown in Fig. 5.5, again as a function of baryon chemical potential μ_B. Results both for physical pion masses as well as in the chiral limit are shown. Worth pointing out is that both nucleon masses become exactly degenerate in the chirally restored phase. In contrast to that, the nucleons' mass splitting for physical pion masses first remains finite after chiral phase transition and then smoothly tends towards zero giving $m_\pm \to m_0$.

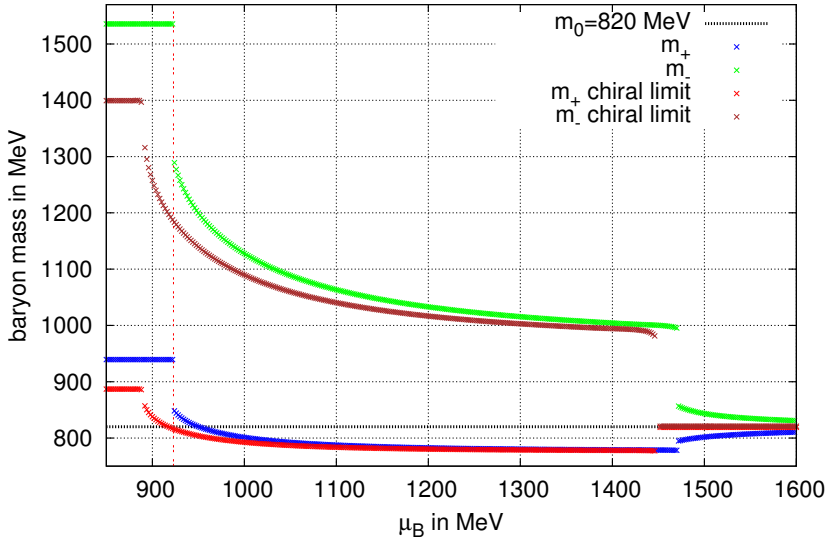

Figure 5.5.: Masses of the nucleons and their parity partners for $m_0 = 820$ MeV as a function of μ_B. Results for physical pion mass $m_\pi = 138$ Mev as well as in the chiral limit ($c \to 0$) are shown. The horizontal dashed line indicates the position of the chirally invariant mass parameter m_0.

This verifies the mechanism through which chiral restoration is realized in models like the parity-doublet model. Rather than being driven into a massless Lee-Wick phase, with vanishing nucleon masses, the nucleons become degenerate in the chirally restored phase, confirming results from lattice QCD simulations [143–145], as mentioned in Sec. 3.1.3.

5.2.2. Full FRG results at finite μ and $T = 0$

To improve the eMF truncation from Sec. 5.2.1, where only contributions from the fermionic part of the RG flow where considered, we want to include collective mesonic excitations as per Eq. (5.13). The full flow equation is then discretized and solved on a grid in field space [73].

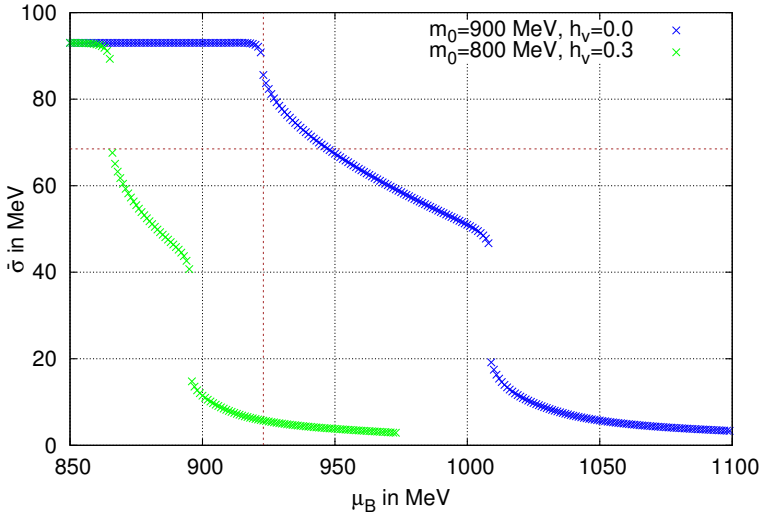

Figure 5.6.: The chiral condensate as a function of μ_B for the nuclear matter and the chiral phase transition with $m_0 = 800$ MeV and $m_0 = 900$ MeV. Parameters have been fixed to the in-medium condensate (horizontal dotted line) for $m_0 = 800$ MeV, and to the binding energy per nucleon (vertical dotted line) for $m_0 = 900$ MeV.

Results for the value of the chiral condensate $\bar{\sigma}$ for two different parameter sets are shown in Fig. 5.6. The chiral condensate is shown as a function of baryon chemical potential μ_B, where the two distinct data sets correspond to one with $m_0 = 800$ MeV and vector coupling $h_v = 0.3$, which reproduces the phenomenologically correct in-medium condensate $\bar{\sigma}(n_0) \simeq 69$ MeV and the second one with $m_0 = 900$ MeV and $h_v = 0$, fixed to reproduce the physical binding energy per nucleon $E_B = 16$ MeV. For both data sets the remaining parameters were adjusted to give physical values for the pion and baryon masses. As a first observation it should be mentioned, that the existence of two distinct discontinuities in the chiral condensate remains robust when including mesonic fluctuations going beyond the extended mean-field approximation, compare eg. Fig. 5.4. As indicated by the two dotted red lines in Fig. 5.6 one can either reproduce the phenomenologically correct in-medium condensate (horizontal red line) or the correct binding energy (vertical red line), but not both simultaneously. Using the same sets of parameters as in Fig. 5.6 the corresponding masses of the nucleons and their parity partners are shown in Fig. 5.7. The behavior is similar to the eMF case shown in Fig. 5.5. Both nucleon species tend towards their respective value of m_0 beyond the chiral transition. For the case of the nucleon this happens from below m_0, whereas the heavier parity partners are coming from above m_0. In general one can observe that the (nuclear matter) liquid-gas transition and the chiral transition of the model show the tendency to be

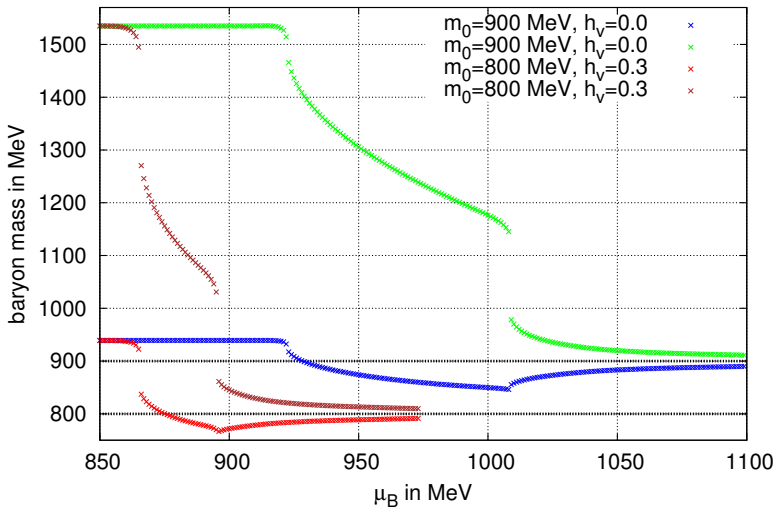

Figure 5.7.: Masses of the nucleons and their parity partners at $m_0 = 800$ MeV and 900 MeV with physical pion masses. The same two sets of parameters as in Fig. 5.6 have been used.

closer together as compared to the eMF calculations from Sec. 5.2.1.

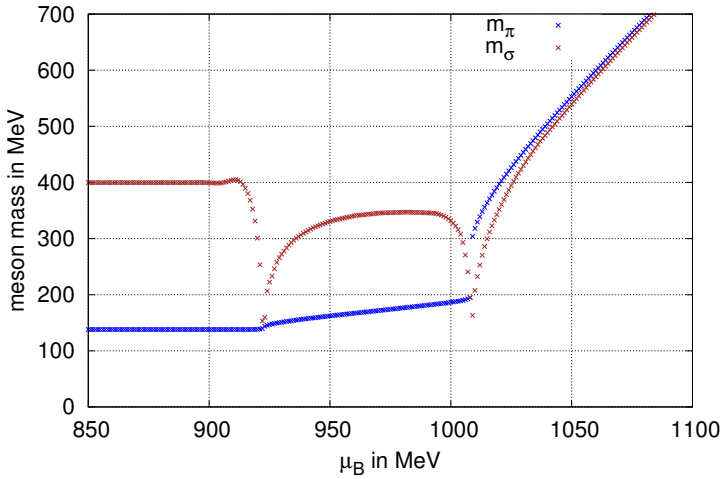

Figure 5.8.: Masses of the scalar and pseudoscalar mesons (σ, π) for $m_0 = 900$ MeV.

For completeness, it is also worthwhile taking a look at the behavior of the meson masses, which are depicted for the parameter set with $m_0 = 900$ MeV in Fig 5.8. Plotted are the masses of the scalar and pseudoscalar mesons (σ, π) as a function of baryon chemical potential μ_B. For low μ_B both the sigma meson and the pion start at their respective vacuum values remaining constant until the first transition, reflecting the Silver-Blaze property. The parameters were chosen such as to realize a physical pion mass of $m_\pi = 138$ MeV, whereas the sigma mass for this particular

data set comes out to be $\sim$ 400 MeV, which is still within an acceptable range. An interesting feature that can be observed here is that the mass of the pion only reacts weakly following the first transition, whereas a clear discontinuity can be recognized at the chiral phase transition. This agrees with the comparably weak nuclear matter transition observed for $m_0 = 900$ MeV in Fig. 5.6. The sigma meson shows a distinct non-trivial behavior already in the nuclear phase with two clear cusps at the positions of the two phase transitions. For large μ_B both mesons become degenerate indicating chiral symmetry restoration.

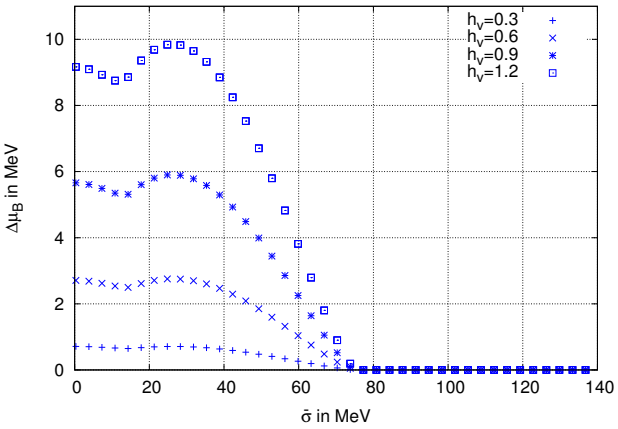

Figure 5.9.: Solutions $\Delta\mu_B = \mathrm{i}h_v\bar{\omega}_0$ of the ω-gap equation at $m_0 = 800$ MeV. $\Delta\mu_B$ is shown as a function of the chiral condensate $\bar{\sigma}$ and for different values of the vector meson coupling h_v.

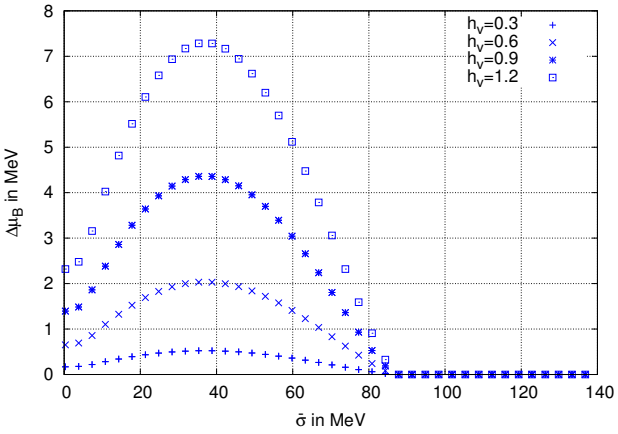

Figure 5.10.: Solutions $\Delta\mu_B = \mathrm{i}h_v\bar{\omega}_0$ of the ω-gap equation at $m_0 = 900$ MeV . $\Delta\mu_B$ is shown as a function of the chiral condensate $\bar{\sigma}$ and for different values of the vector meson coupling h_v.

In contrast to calculations in mean-field and eMF approximations the inclusion of a repulsive vector interaction does not show an effect on the position of the

nuclear matter transition when collective mesonic excitations are included. This becomes clear from Figs. 5.9 and 5.10, where the solutions of the ω-gap equation, cf. Eq. (B.9), are shown as resulting shifts in baryon chemical potential $\Delta\mu_B = \mathrm{i}h_v\bar{\omega}_0$ as a function of the chiral condensate $\bar{\sigma}$ for different values of the vector coupling h_v, similar to Fig. 5.2 in the eMF case from Sec. 5.2.1. The same parameter sets as in Fig. 5.6 were used, corresponding again to values of the chirally invariant coupling parameter $m_0 = 800$ MeV and $m_0 = 900$ MeV. For both m_0 values the bifurcation points, in Figs. 5.9 and 5.10, are close to or smaller than the in-medium condensate $\bar{\sigma}(n_0)$ at saturation density, leading to regions of non-zero $\Delta\mu_B = \mathrm{i}h_v\bar{\omega}_0$ which do not sufficiently overlap with the minimum of the effective potential in σ-direction. This makes the repulsive vector interaction ineffective, compared to eMF calculations, since increasing values of the vector coupling h_v do only change the effective potential away from the minimum, whereas the grand potential which is evaluated at $\bar{\sigma}_0$ (on both sides of the transition) basically remains unchanged. This implication can also be further affirmed by Figs. 5.11 and 5.12, which show the baryon number density $n(\mu_B)$ as a function of baryon chemical potential for the two aforementioned parameter sets.

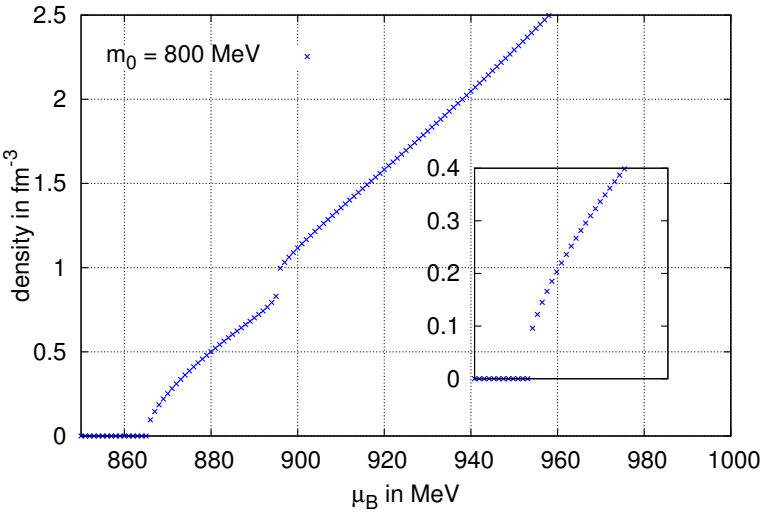

Figure 5.11.: Baryon number density $n(\mu_B)$ as a function of baryon chemical potential. Shown is a close-up view for the data set with $m_0 = 800$ MeV.

For $m_0 = 800$ MeV (and $h_v = 0.3$) one can still identify two distinct discontinuities in the density at the the positions of the two phase transitions, cf. Fig. 5.6, albeit taking a closer look at Fig. 5.11 we see that the saturation density in this case is about $n_0 \simeq 0.098$ fm^{-3} which is 40 % lower than the physical value of 0.16 fm^{-3}, even though this particular parameter set realizes a physical in-medium condensate. The discrepancy in the density cannot be further improved through higher vector couplings, by the same arguments as before, confirming that a crucial part of the baryon number density stems from the (non-vanishing) expectation value of the repulsive vector meson ω.

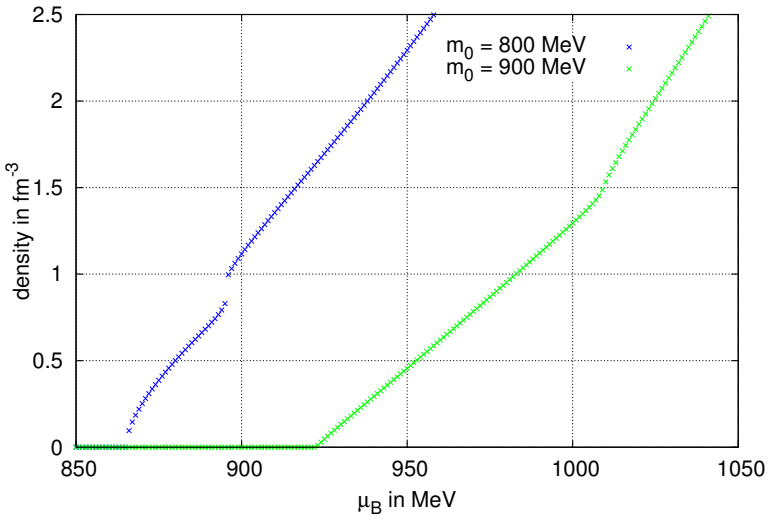

Figure 5.12.: Baryon number density $n(\mu_B)$ as a function of baryon chemical potential. Shown are both the data set with $m_0 = 800$ MeV and $m_0 = 900$ MeV, respectively.

In the case with $m_0 = 900$ MeV, compare Fig.5.12, this effect can be seen in greater detail, since the discontinuities in the baryon number density even become negligibly small, only appearing to be kinks in the density. This shows that the missing density contributions from the repulsive vector meson play a crucial role in realizing phenomenologically acceptable nuclear matter properties, which in contrast to the eMF case, including the full RG flow is only possible within separate parameter sets.

5.2.3. Full FRG results at finite μ and T

Both Sec. 5.2.2 and Sec. 5.2.1 were concerned with studying the parity-doublet model at vanishing temperatures. Since we are using an Euclidean approach, the RG flow equations for the effective potential are already formulated for finite temperatures (and of course baryon chemical potential), which makes it in principle straightforward to calculate the phase diagram once the model parameters are fixed for zero temperature. In the following we discuss phase diagrams of the parity-doublet model obtained in the (T, μ_B)-plane for the full RG flow, meaning including fermionic as well as mesonic contributions to the flow equation as in Sec. 5.2.2. Since we have seen that the inclusion of a repulsive vector-meson interaction is negligible for full RG considerations, we neglect those in the following, i.e. we set $h_v = 0$. From the phase diagrams it is possible to extract critical temperatures for both the nuclear matter $T_c^{(n)}$ and the chiral transition $T_c^{(\chi)}$, which should be understood as qualitative estimates of the critical temperatures, following from the zero-temperature fixed model, not as quantitative precise predictions of the latter.

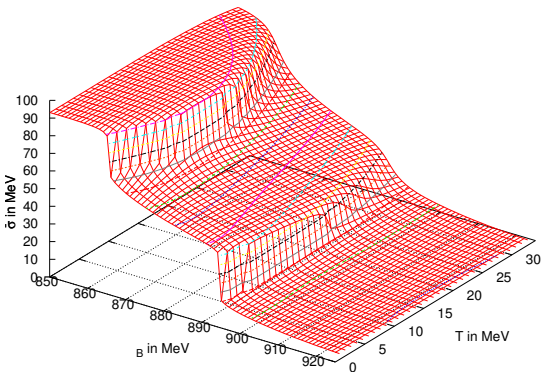

Figure 5.13.: $m_0 = 800$ MeV

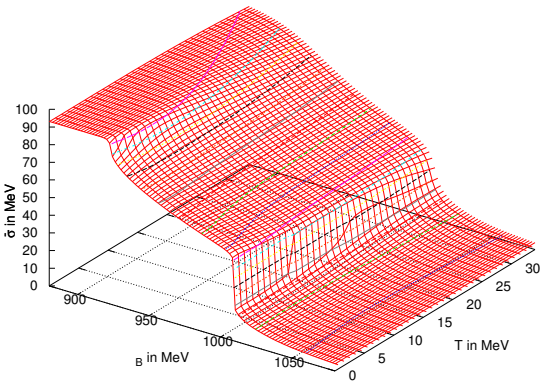

Figure 5.14.: $m_0 = 900$ MeV

For the finite temperature calculations the parameter sets from Fig. 5.6, setting $h_v = 0$ in both cases, were used. In Figs. 5.13 and 5.14 the resulting chiral condensates $\bar{\sigma}$ are shown as a function of temperature T and baryon chemical potential μ_B. As one would expect including finite temperature affects both the nuclear matter transitions and the chiral transition of the model in the same way, namely weakening both first order transitions until they eventually become continuous transitions for sufficiently high temperatures.

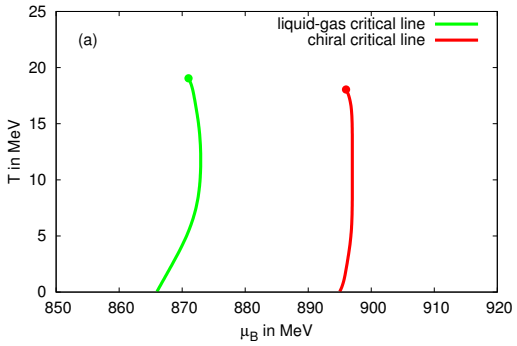

Figure 5.15.: First order critical lines for the nuclear matter and chiral transition for $m_0 = 800$ MeV.

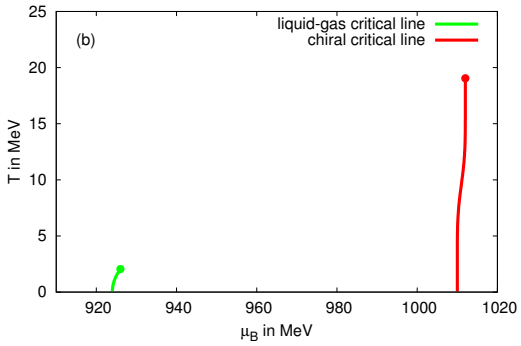

Figure 5.16.: First order critical lines for the nuclear matter and chiral transition for $m_0 = 900$ MeV.

In Figs. 5.15 and 5.16 the first order critical lines are plotted in the μ_B-T plane both for the nuclear matter and the chiral transition and for both data sets. For the parameter set with $m_0 = 800$ MeV in Fig. 5.15 the position of the critical endpoint (CEP) of the liquid-gas transition of nuclear matter can be estimated to be $T_c^{(n)} \sim 19$ MeV and $\mu_B^{c(n)} \simeq 871$ MeV. Furthermore the chiral CEP is around $T_c^{(\chi)} \sim 18$ MeV and $\mu_B^{c(\chi)} \simeq 896$ MeV. Taking another glance at Fig. 5.14 we see that in this case the nuclear matter transition is much weaker than for $m_0 = 800$ MeV, cf. Fig. 5.15, which is also reflected in a much shorter nuclear matter critical line in the corresponding Fig. 5.16. Consequently in this case the nuclear matter transition becomes continuous already at a much lower temperature of roughly $T_c^{(n)} \simeq 2$ MeV and a chemical potential value of $\mu_B^{c(n)} \simeq 925$ MeV. The chiral CEP can be estimated to be around $T_c^{(\chi)} \sim 19$ MeV and $\mu_B^{c(\chi)} \simeq 1012$ MeV. Notably the nuclear matter critical endpoints seem to be located at slightly higher chemical potential values compared to their zero temperature transitions at $\mu_B^{c(n)} \simeq 866$ MeV and $\mu_B^{c(\chi)} \simeq 895$ MeV for $m_0 = 800$ MeV, and $\mu_B^{c(n)} \simeq 923$ MeV and $\mu_B^{c(\chi)} \simeq 1015$ MeV for $m_0 = 900$ MeV. Conversely the chiral first-order critical lines appear to almost follow lines of constant μ_B, which is more pronounced for the $m_0 = 900$ MeV parameter set.

Picking up on the discussions from Sec. 3.2.2 we want to take a closer look at the slopes of the first order critical lines in Figs. 5.15 and 5.16. In general the slope of the first-order lines in the (T, μ_B)-plane obeys a Clausius-Clapeyron equation [174]

$$\frac{\mathrm{d}T_c}{\mathrm{d}\mu_c} = -\frac{\Delta n}{\Delta s}\,. \tag{5.16}$$

Going across the first-order critical lines in positive μ_B-direction we have an increase in the number density $\Delta n > 0$, for both the nuclear matter and the chiral transition line. As the entropy density per particle is expected to increase, for an order-disorder transition, with $\Delta n > 0$ one would also expect the discontinuity in the entropy density to be positive, hence giving $\Delta s > 0$. This behavior is typically seen in mean-field studies of the chiral first order line, see e.g. [35]. Including mesonic fluctuations and explicit chiral symmetry breaking we see from Fig. 5.16

that Δs for the chiral transition is very small here and could in the chiral limit well be positive. Furthermore it is interesting to mention, that depending on the magnitude of Δn across the liquid-gas transition actually also $\Delta s < 0$ is possible, since the entropy per particle decreases in such a transition. This is what we observe in the parity-doublet model, when both fermionic and bosonic fluctuations are taken into account, see Fig. 5.16. A similar effect is also seen in quark-meson model calculations with mesonic fluctuations where the mean-field chiral phase transition is turned into a transition to bound quark matter [31]. Another example is the relativistic analogue of a Chandrasekhar-Clogston transition with condensed pions at finite isospin chemical potential, which shows $\Delta s > 0$ at mean-field but turns into a phase transition with $\Delta s < 0$. A transition to such a so-called stable Sarma phase has been observed [77, 125], as soon as mesonic fluctuations are included. These implications let us conclude, that mesonic fluctuations (in LPA) in general tend to change the sign of Δs, even though it is fairly unusual to have $\Delta s < 0$ for the liquid-gas transition of nuclear matter in QCD. For example it has not been observed in chiral effective field theory (χEFT) calculations, see e.g. [184].

5.2.4. Towards a higher order truncation

Similar to the previous sections, covering the parity-doublet model within the so-called local potential approximation, meaning only including scale-dependency of the local potential U_k changing the ansatz for the effective average action Γ_k, we can include beyond LPA effects in a consistent way, very similar to the quark-meson considerations in Sec. 4.2.

Analogous to Sec. 4.2, let us introduce a slightly modified Lagrangian for the parity-doublet model

$$\begin{aligned}\mathcal{L} =& Z_{F,k}\bar{N}_1\big(\partial\!\!\!/ - \mu_B\gamma_0 + h_1(\sigma + \mathrm{i}\gamma_5\vec{\tau}\vec{\pi}) + \mathrm{i}h_v\gamma^\mu\omega_\mu\big)N_1 \\ &+ Z_{F,k}\bar{N}_2\big(\partial\!\!\!/ - \mu_B\gamma_0 + h_2(\sigma - \mathrm{i}\gamma_5\vec{\tau}\vec{\pi}) + \mathrm{i}h_v\gamma^\mu\omega_\mu\big)N_2 \\ &+ m_0(\bar{N}_1\gamma_5 N_2 - \bar{N}_2\gamma_5 N_1) \\ &+ \frac{1}{2}Z_{\phi,k}\partial_\mu\vec{\phi}\partial^\mu\vec{\phi} + U(\phi^2,\omega^2) - c\sigma\ ,\end{aligned} \tag{5.17}$$

now including a wave function renormalization factors $Z_{\phi,k}$ and $Z_{F,k}$, which modify the momentum dependent part of the two-point functions. As motivated in Sec. 4.2, we will for simplicity set $Z_{F,k} = 1$. The corresponding flow equation for the effective potential can be computed using a modified version of the $3d$-optimized Litim regulator, see App. C.4 for a detailed derivation.

$$\begin{aligned}\partial_k U_k =& -\frac{N_f k^4}{6\pi^2}\sum_{\pm}\frac{\epsilon_k^{\pm}(1 - n_F(\epsilon_k^{\mp} + \tilde{\mu}_B)) - \epsilon_k^{\pm} n_F(\epsilon_k^{\mp} + \tilde{\mu}_B)}{\epsilon_k^{\mp}\epsilon_k^{\pm}} \\ &+ \frac{k^4}{60\pi^2}\left[\frac{(1 + 2n_B(E_k^\sigma))(5Z_{\phi,k} + k\partial_k Z_{\phi,k})}{E_k^\sigma Z_{\phi,k}} + \right. \\ &\left. \frac{(N_f^2 - 1)(1 + 2n_B(E_k^\pi))(5Z_{\phi,k} + k\partial_k Z_{\phi,k})}{E_k^\pi Z_{\phi,k}}\right],\end{aligned} \tag{5.18}$$

where we introduced the renormalized scalar and pseudoscalar k-dependent single-quasiparticle energies

$$\begin{aligned} E_k^\pi &= \sqrt{k^2 + \frac{m_\pi^2}{Z_{\phi,k}}}\,, \\ E_k^\sigma &= \sqrt{k^2 + \frac{m_\sigma^2}{Z_{\phi,k}}}\,, \end{aligned} \tag{5.19}$$

which are the direct generalization of the LPA energies in Eq. (5.14) and use the LPA curvature masses from Eq. (5.15). The terms occurring in Eq. (5.18) are very similar to those in Eq. (5.13), the only difference is again directly related to the mesonic anomalous dimension $\eta_\phi = -k\partial_k \ln(Z_{\phi,k})$. In the limit $Z_{\phi,k} = 1$ we recover the full LPA RG flow equation for the LPA parity-doublet model, cf. Eqs. (5.12),(5.13).

The respective RG flow equation for $Z_{\phi,k}$ can again be calculated by taking two functional derivatives of the Wetterich equation (Fig. 2.4).

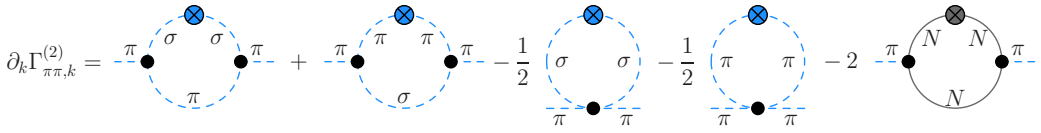

Figure 5.17.: Diagrammatic representation of the RG flow of the pion two-point function for the parity-doublet model beyond LPA.

From the RG flow equation in Fig. 5.17 the flow equation for $Z_{\phi,k}$ can be projected out in the following way

$$\partial_k Z_{\phi,k} = \left(\frac{1}{2} \frac{\partial^2}{\partial \vec{p}^2} \partial_k \Gamma^{(2)}_{\pi,k} \right) \Bigg|_{\vec{p}=0}\,, \tag{5.20}$$

where again the tadpole diagrams do not contribute because they are momentum independent. Explicit expressions for $\partial_k Z_{\phi,k}$ are also included in App. C.4.

Numerical results

Before we discuss some first results for the beyond LPA parity-doublet model let us briefly review the numerical procedure. We chose a UV cutoff scale of $\Lambda = 1700$ MeV which allowed for a symmetric potential at in the UV. Also to simplify finding suitable parameters, we only aimed at reproducing the physical nucleon mass and took the resulting parity partner mass as $m_+ = 1300$ MeV.

So the following considerations should be understood as qualitative study, only aiming at applying the LPA' procedure introduced in Sec. 4.2 to a parity doublet model including a nucleon and a heavier parity partner.

In Fig.5.18 we show results for the renormalized chiral condensate as a function of baryon chemical potential μ_B for different values of the chirally invariant mass parameter m_0. It can be seen that for small values of m_0, in this case $m_0 = 700$ MeV

it is possible to lose the two distinct first order phase transitions altogether. This is actually an effect that can be seen in eMF and RG calculations in LPA as well.

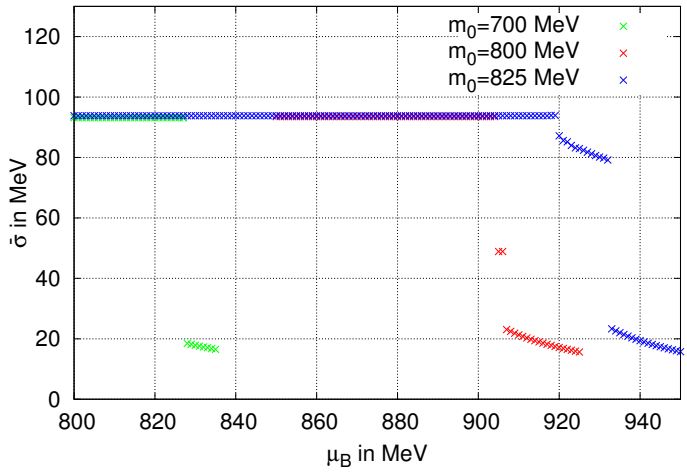

Figure 5.18.: Chiral condensate $\bar{\sigma}$ as a function of baryon chemical potential μ_B for different values of m_0 at $T = 0$.

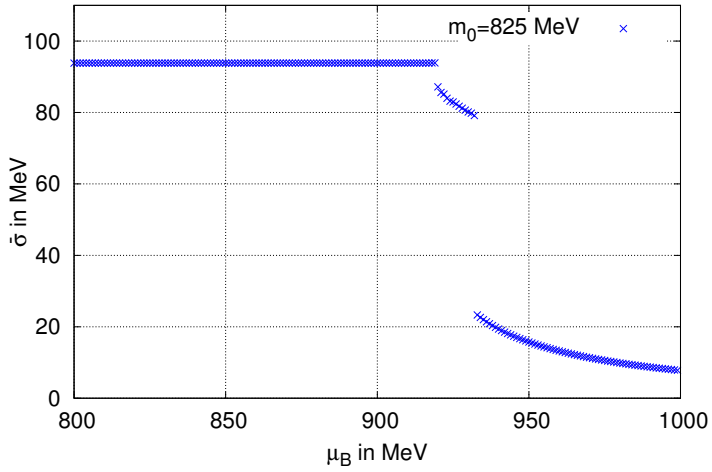

Figure 5.19.: Chiral condensate $\bar{\sigma}$ as a function of baryon chemical potential μ_B at $T = 0$.

If one chooses the mass parameter m_0 too small the two first order phase transitions get shifted so close together, that they basically appear as one. For $m_0 =$ 800 MeV we see an intermediate case where nuclear matter phase is very small and for $m_0 = 825$ MeV we roughly reproduce the binding energy of nuclear matter, with a nuclear matter transition at $\mu_B \approx 920$ MeV.

In Fig. 5.19 we show a more detailed view of the parameter set with $m_0 =$ 825 MeV. In this case the nuclear matter and the chiral transition of the model are

closer together then in the eMF calculations, compare for example Fig. 5.4, and even closer than in the LPA calculations, compare e.g. Fig. 5.6.

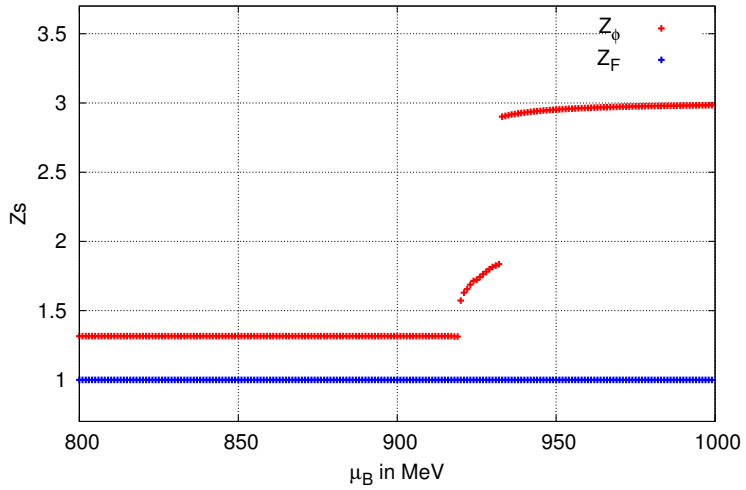

Figure 5.20.: Wave function renormalization factors $Z_{\phi,k}$ and $Z_{F,k}$ as a function of μ_B.

In Fig.5.20 the corresponding solutions for the wave function renormalization factors $Z_{\phi,k}$ and $Z_{F,k}$ are plotted as a function of μ_B, in our approximation $Z_{F,k} = \text{const} = 1$ and is just plotted as a reference. $Z_{\phi,k}$ stays constant up until the nuclear matter transition where it shows a discontinuity which is followed by an intermediate increase. At the chiral transition of the model $Z_{\phi,k}$ shows another discontinuity and afterwards saturates for larger μ_B.

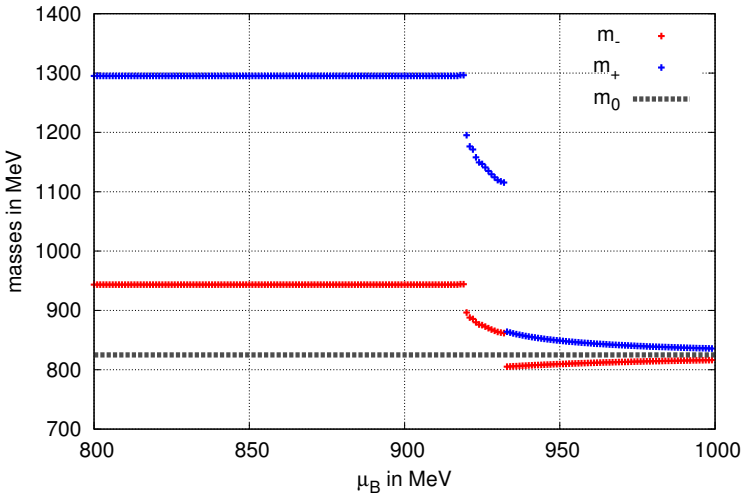

Figure 5.21.: Masses of the nucleons and their parity partners as a function of baryon chemical potential μ_B for $m_0 = 825$ MeV.

In Fig.5.21 we show the masses of the nucleons and their heavier parity part-

ners. The vacuum values for the nucleon mass in the vacuum is $m_- = 940$ MeV, whereas for the mass of the parity partner we have $m_+ = 1300$ MeV for the chosen parameters. The mass of the nucleon and its parity partner both show two distinct first order phase transitions. After the nuclear matter transition of the model, both masses are still different, whereas after the chiral phase transition they both approach the chirally invariant mass term $m_0 = 825$ MeV, where the nucleon approaches from below and the parity partner from above m_0. For large μ_B we again find $m_+ = m_- = m_0$, similar to the eMF and LPA calculations from Sec. 5.2.1 and Sec. 5.2.2. This behavior again reflects how chiral symmetry restoration for baryons is achieved in the parity-doublet model, namely by degenerate yet finite baryon masses in the chirally restored phase.

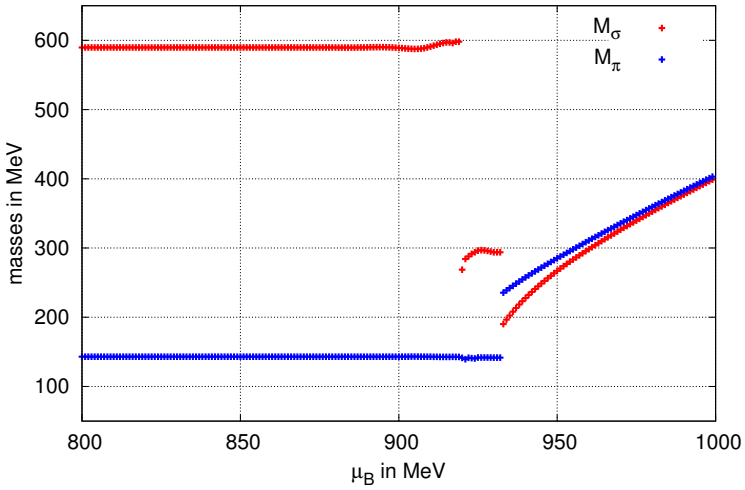

Figure 5.22.: Masses of the mesons $m_0 = 825$ MeV.

Let us close with discussing the μ_B-dependence of the masses of the scalar and pseudoscalar mesons of the model. The renormalized masses of sigma and pion are shown Fig. 5.22 as a function of μ_B, analogous to the LPA case in Fig. 5.8. The vacuum value for the pion mass is its physical value $M_\pi = 138$ MeV whereas the sigma mass for the chosen parameters comes out at $M_\sigma = 590$ MeV. Quite interestingly in the nuclear matter phase only the mass of the sigma-meson changes, while the pion mass barely reacts, much similar to Fig. 5.8, in the LPA parity-doublet model.

6
Conclusion

We have seen that the functional renormalization group is a very well suited framework to study the phase diagram of strongly interacting matter. We used a chiral quark-meson model to study the chiral phase transition as well as a parity-doublet model to study the liquid-gas transition of nuclear matter together with chiral symmetry restoration in the high baryon density regime.

In Chap. 4 we were concerned with the two-flavor chiral quark-meson model as a model for low-energy QCD. In Sec. 4.1 we extended the method of analytically continued RG flow equations for two-point functions, which has been used in the recent years to calculate meson spectral functions, to include also quark spectral functions. A similar method can in principle also be used to calculate baryon spectral functions. The crucial step in these calculations is a two-step analytic continuation procedure which allowed to extract RG flow equations for the full retarded quark two-point function. These two-point RG flow equations could be solved using the scale dependent effective potential in a local potential approximation as an input. Also the question of how to extract physical (curvature) masses from the scale dependent effective potential, was discussed by comparing solutions from a grid calculation to a fourth-order Taylor expansion. From the solutions for the retarded two-point function, i.e. its scale dependent Dirac dressing functions B_k and C_k, the full retarded propagator in the IR at $T = \mu = 0$ could be extracted. This allows to calculate vacuum spectral functions directly, which is an advantage compared to Bayesian methods which reconstruct spectral properties from the Euclidean propagator. Through the real parts of the dressings B_k and C_k we could calculate the quark pole mass, whereas the respective imaginary parts gave insight to the particle thresholds of the model. We then calculated quark and anti-quark spectral functions $\rho_\pm$ and their symmetric and antisymmetric combinations ρ_C and ρ_B, where ρ_C was the positive semi-definite spectral function. Furthermore we compared our calculated spectral functions (for $\epsilon \to 0$) with sum rules that can be directly derived from the Källén-Lehmann spectral representation of the retarded propagator, and

found them to be in good agreement. In the future these considerations could be extended to include finite temperature and chemical potential. Further extending the framework to include baryonic degrees of freedom, a long-term goal could be to eventually calculate in-medium nucleon spectral functions from the FRG.

In Sec. 4.2 we considered the two-flavor quark-meson model in a beyond LPA truncation including bosonic and fermionic wave function renormalization factors. We showed how the flow equation for effective potential U_k gets modified in this truncation and how we can extract flow equations for the wave function renormalizations by projection of the respective two-point flow equations. We calculated phase diagrams in this truncation and found that critical first order lines with $\frac{dT_c}{d\mu_c} < 0$, irrespective of whether a fermionic wave function renormalization is included.

In Chap. 5 we studied the phase diagram of strongly interacting matter in the vicinity of the nuclear matter liquid-gas transition. The crucial step here was to consider a chiral baryon-meson model that includes the nucleon isodoublet as well as a doublet of the nucleons' heavier parity partners. Such models are called parity-doublet (or mirror-) models and the unique feature of these models is the possibility to include a Dirac mass term (proportional to m_0) that does not break chiral symmetry. This is achieved by adapting a so-called mirror-assignment under chiral transformations for the two pairs of nucleons. Already on mean-field level this allows us to circumvent a transition to massless Lee-Wick matter, which usual chiral models for nuclear matter like the chiral Walecka model suffer from. For the parity-doublet model we showed how to treat it within the FRG framework by again choosing an ansatz for the effective action in local potential approximation. We calculated the flow equation for the effective potential U_k which lead to similar parts for the bosonic parts of the RG flow and a unique fermionic contribution which reduces to a sum of two ordinary quark-meson like contributions in the limit $m_0 \to 0$.

We first obtained results for the parity-doublet model in the so-called extended mean-field approximation, where only the fermion loop in the Wetterich equation is considered. This is known to be similar to standard mean-field calculations, but includes vacuum contributions in a more consistent way. In this approximation we calculated the cold and dense regime of the phase diagram and found bound nuclear matter with a binding energy of $E_B = 16$ MeV, indicated by a first order phase transition at $\mu_c = 939 - 16 = 923$ MeV. Furthermore we could realize a physical value for the in-medium condensate $\bar{\sigma}(n_0) \simeq 69$ MeV which corresponds to a nucleon-sigma term $\sigma_N \simeq 36$ MeV. Also the nuclear matter saturation density with a physical value of 0.16 fm^{-3} could be realized all within the same parameter set. To be able to realize these nuclear matter properties in their entirety, the inclusion of a repulsive vector interaction, described by a mean-field isoscalar vector meson ω, was crucial. Apart from a phenomenologically satisfying nuclear matter transition the model also showed a second first order phase transition, which we identified as the chiral transition of the model. In the extended mean-field approximation, anyway, this second transition appeared at such high values of the baryon chemical potential that it will hardly be relevant for the equation of state of e.g. neutron stars.

We then obtained results for the parity-doublet model also including mesonic fluctuations, hence including the full RG flow of the model. Here we found that the

appearance of two distinct first order transition remains robust. Nuclear matter properties could be realized in separate parameter sets, where we realized the right binding energy in one and a phenomenologically acceptable in medium condensate in the other. The inclusion of a isoscalar vector meson was ineffective in the full RG calculations, which was understood by studying the solutions of the ω-gap equation. The bifurcation points (where $\bar{\omega}_0(\sigma)$ becomes nonzero) did not sufficiently overlap with the minimum of the effective potential, which makes the vector meson ineffective in shifting the first order transition to larger densities. An interesting future endeavor could be to study how this situation changes once the ω is included as a fluctuating field inside the loops.

Studying the phase diagram at finite temperature and chemical potential, we found that both critical first order lines end in respective critical endpoints, which let us extract very rough estimates for the critical temperatures. $T_c^{(n)} \sim 2 - 19$ MeV for the nuclear matter transition and $T_c^{(\chi)} \sim 18 - 19$ MeV for chiral transition. It is worth noting that the slopes of the critical first order lines showed regions with $\frac{dT_c}{d\mu_c} > 0$, similar to the LPA quark-meson model.

Finally we considered the zero temperature parity-doublet model in a beyond LPA truncation and showed that it is in principle possible to include a heavy parity partner for the nucleon and apply the same method for the inclusion of a scale dependent bosonic wave function renormalization factor, as in Sec. 4.2. The results of the LPA' parity-doublet model are at the moment on a qualitative level and need further investigation to get to more quantitative predictions.

A

Notation and Conventions

A.1. Gamma Matrices

For the most part in our FRG calculations we work in Euclidean space-time, so we use Euclidean gamma matrices

$$\gamma^0 = \begin{pmatrix} 0 & \mathbb{1} \\ \mathbb{1} & 0 \end{pmatrix} \quad , \quad \gamma^i = \begin{pmatrix} 0 & i\sigma^i \\ -i\sigma^i & 0 \end{pmatrix}, \tag{A.1}$$

where σ^i are the Pauli matrices,

$$\sigma^1 = \begin{pmatrix} 0 & 1 \\ 1 & 0 \end{pmatrix} \quad , \quad \sigma^2 = \begin{pmatrix} 0 & -i \\ i & 0 \end{pmatrix} \quad , \quad \sigma^3 = \begin{pmatrix} 1 & 0 \\ 0 & -1 \end{pmatrix}, \tag{A.2}$$

The γ^μ are hermitian

$$\gamma^{\mu\dagger} = \gamma^\mu. \tag{A.3}$$

and fulfill the following algebra

$$\{\gamma^\mu, \gamma^\nu\} = 2\delta^{\mu\nu}\mathbb{1} \tag{A.4}$$

Additionally we define

$$\gamma^5 = \gamma^0\gamma^1\gamma^2\gamma^3. \tag{A.5}$$

Explicitly they look like

$$\gamma^0 = \begin{pmatrix} 0 & 0 & 1 & 0 \\ 0 & 0 & 0 & 1 \\ 1 & 0 & 0 & 0 \\ 0 & 1 & 0 & 0 \end{pmatrix}, \qquad \gamma^1 = \begin{pmatrix} 0 & 0 & 0 & \mathrm{i} \\ 0 & 0 & \mathrm{i} & 0 \\ 0 & -\mathrm{i} & 0 & 0 \\ -\mathrm{i} & 0 & 0 & 0 \end{pmatrix},$$
$$\gamma^2 = \begin{pmatrix} 0 & 0 & 0 & 1 \\ 0 & 0 & -1 & 0 \\ 0 & -1 & 0 & 0 \\ 1 & 0 & 0 & 0 \end{pmatrix}, \quad \gamma^3 = \begin{pmatrix} 0 & 0 & \mathrm{i} & 0 \\ 0 & 0 & 0 & -\mathrm{i} \\ -\mathrm{i} & 0 & 0 & 0 \\ 0 & \mathrm{i} & 0 & 0 \end{pmatrix}. \tag{A.6}$$

A.2. Conventions for Fourier Transforms and Functional Derivatives

The following conventions were used throughout this work

$$\int \frac{\mathrm{d}^4 p}{(2\pi)^4} = \int_p, \; \int \mathrm{d}^4 x = \int_x,$$
$$\phi(x) = \int_p \tilde{\phi}(p) e^{\mathrm{i}p(x-x')}, \; \int_x e^{\mathrm{i}(p+p')x} = (2\pi)^4 \delta^{(4)}(p+p').$$

The following small calculation is useful for calculating functional derivatives of 4-gradients of fields

$$\frac{\partial}{\partial \phi_a(x)} \partial_\mu \phi_b(x') = \frac{\partial}{\partial \phi_a(x)} \frac{\partial}{\partial x'^\mu} \phi_b(x') \tag{A.7}$$
$$= \delta_{ab} \partial_\mu \delta^{(4)}(x'-x) = \delta_{ab} \int_p (\mathrm{i}p_\mu) e^{\mathrm{i}p(x-x')}. \tag{A.8}$$

A.3. Matsubara Sums

In the Euclidean approach finite temperature is introduced by replacing

$$\int \frac{\mathrm{d}^4 p}{(2\pi)^4} \to T \sum_{p_0} \int \frac{\mathrm{d}^3 p}{(2\pi)^3}, \tag{A.9}$$

where the sum runs over bosonic or fermionic Matsubara frequencies

$$\omega_B = 2n\pi T, \tag{A.10}$$
$$\omega_F = 2(n+1)\pi T, \tag{A.11}$$

with $n \in \mathbb{Z}$.

B

General Considerations

B.1. Basics of Quantum Field Theory

We want to give a quick collection of important quantum field theory basics. For a field with bosonic and fermionic degrees of freedom and their respective sources

$$\varphi = \begin{pmatrix} \phi \\ \vdots \\ \psi \\ \vdots \\ \bar{\psi}^T \\ \vdots \end{pmatrix}, J = \begin{pmatrix} j \\ \vdots \\ \bar{\eta} \\ \vdots \\ \eta^T \\ \vdots \end{pmatrix}. \tag{B.1}$$

The Generating functional is given by

$$Z[J] = \int \mathcal{D}\varphi e^{-S[\varphi]+\int J^T\varphi} . \tag{B.2}$$

From the generating functional n-point functions can be calculated by

$$\langle \varphi_i(x_1) \dots \varphi_i(x_n) \rangle = \frac{1}{Z[J=0]} \frac{\delta^n Z[J]}{\delta J_i(x_1) \dots \delta J_i(x_n)}\bigg|_{J=0} . \tag{B.3}$$

The Schwinger functional is given by

$$W[J] = \ln Z[J] = \ln \Big(\int \mathcal{D}\varphi \mathrm{e}^{-S[\varphi]+\int J^T\varphi} \Big) . \tag{B.4}$$

The effective action, as the Legendre transform of the Schwinger functional takes the form

$$\Gamma[\varphi] = \sup_J \Big(\int J\varphi - W[J] \Big) . \tag{B.5}$$

The expectation value of the field can be calculated by

$$\frac{\delta W[J]}{\delta J_i(x)} = \frac{1}{Z[J_i(x)]} \int \mathcal{D}\varphi_i \varphi_i(x) \mathrm{e}^{-S[\varphi]+\int J^T \varphi} = \langle \varphi_i(x) \rangle \,. \tag{B.6}$$

The quantum equation of motion for the classical expectation value look like

$$\begin{aligned} \frac{\delta \Gamma}{\delta \varphi(x)} &= \left(\frac{\delta}{\delta \varphi(x)} \int J\varphi - \frac{\delta W[J]}{\delta \varphi(x)} \right) \Bigg|_{J=J_{sup}} \\ &= \left(J(x) + \int \frac{\delta J}{\delta \varphi(x)} \varphi - \int \frac{\delta W[J]}{\delta J} \frac{\delta J}{\delta \varphi(x)} \right) \Bigg|_{J=J_{sup}} \\ &= J_{sup}(x) \,. \end{aligned} \tag{B.7}$$

B.2. The Silver Blaze Property

The Silver Blaze property [185] is a general property of relativistic field theories at zero temperature. When degrees of freedom with a mass gap are coupled to a chemical potential the partition function and consequently all thermodynamic observables have to remain independent of the chemical potential μ as long as μ is below the mass of the lightest excitation in the spectrum. For a first order phase transition, which may occur before, the difference between the gap and the position of the first order phase transition is called binding energy.

B.3. Gap Equations for the Parity-doublet model in LPA

In order to extract the thermodynamic grand potential we need to minimize the resulting effective action $\int \mathrm{d}k \partial_k U_k(\sigma, \omega)$ in the direction of the σ field. Since the ω-meson is not included as a fluctuating field in our approximation it is included as a mean field in a stationary phase approximation resulting in a purely imaginary saddle point for the ω direction.

This means that we require vanishing partial derivatives of $U_k|_{k\to 0}$ with respect to σ and ω_0 when evaluated at the respective expectation values $\sigma = \bar{\sigma}$ and $\omega_0 = \bar{\omega}_0$. The respective gap equations take the form,

$$\frac{\partial}{\partial \sigma} \left(\int \mathrm{d}k \, \partial_k U_k \right) \Bigg|_{\sigma=\bar{\sigma}, \omega_0=\bar{\omega}_0} = c \,, \tag{B.8}$$

and

$$\frac{\partial}{\partial \omega_0} \left(\int \mathrm{d}k \, \partial_k U_k \right) \Bigg|_{\sigma=\bar{\sigma}, \omega_0=\bar{\omega}_0} = -m_\omega^2 \bar{\omega}_0 \,. \tag{B.9}$$

Eqs. (B.9) and (B.8) can also be seen as the defining equations for the expectation values of the meson fields $\bar{\sigma}$ and $\bar{\omega}_0$.

Since the ω-meson only affects the fermionic loop in the flow equation and does not mix with the σ direction, its gap equation can be extracted solely from the fermionic RG flow in Eq. (5.12). For deriving the gap equation for ω_0 it is worthwhile

using the following equivalence between partial derivatives with respect to ω_0 and derivatives with respect to the baryon chemical potential μ_B,

$$\frac{\partial}{\partial\omega_0} = -\mathrm{i}h_v \frac{\partial}{\partial\mu_B} \,. \tag{B.10}$$

For the zero temperature case, the gap equation for ω_0 can even be derived analytically in closed form by straightforward k-integration resulting in

$$\frac{\partial}{\partial\omega_0}\int \mathrm{d}k\, \partial_k U_k\Big|_{\bar\sigma,\bar\omega_0} = \mathrm{i}h_v \frac{4}{6\pi^2}\sum_{\pm} \frac{k_F^{\pm 4}\gamma^{\pm}(k_F^{\pm})}{|\partial_k \epsilon_k^{\pm}|_{k=k_F^{\pm}}|} \,, \tag{B.11}$$

with

$$\gamma^{\pm} = \frac{2(k^2 + m_0 - \epsilon_k^{\pm 2}) + \sigma^2(h_1^2 + h_2^2)}{\epsilon_k^{\pm}(\epsilon_k^{\mp 2} - \epsilon_k^{\pm 2})} \,. \tag{B.12}$$

Here, $k_F^{\pm}$ are the Fermi momenta defined by

$$\epsilon_k^{\pm}(k_F^{\pm}) = \tilde\mu_B. \tag{B.13}$$

Furthermore, Eq. (B.11) also allows for obtaining the baryon number density,

$$n_B = -\frac{\partial U_0}{\partial\mu_B} = \frac{1}{\mathrm{i}h_v}\frac{\partial}{\partial\omega_0}\int \mathrm{d}k\, \partial_k U_k\Big|_{\bar\sigma,\bar\omega_0} \,. \tag{B.14}$$

Using $n_b^{\pm}$ for The contributions to the number densities of nucleons and their parity partners we find,

$$n_B = \sum_{\pm} n_B^{\pm} = \frac{4}{6\pi^2}\sum_{\pm}\frac{k_F^{\pm 4}\gamma^{\pm}(k_F^{\pm})}{|\partial_k \epsilon_k^{\pm}|_{k=k_F^{\pm}}|} \,. \tag{B.15}$$

In contrast to the ω-gap equation which can be derived by direct k-integration, the solution of the gap equation for the σ-meson, Eq. (B.8), corresponds to keeping the field-dependence intact and numerically solving the full RG flow equation, which is then followed by a minimization in the σ direction.

In the finite temperature case the ω gap equation can no longer be integrated analytically in closed form, but has to be solved by numerically integrating over k on a ω grid and subsequently minimizing the result with respect to ω.

C

Explicit Expression for Flow Equations

All the inner traces in the various RG flow equations are performed using *FormTracer* [186], a *Mathematica* package that allows for a very efficient evaluation of high dimensional traces.

C.1. Quark-meson Model in LPA

C.1.1. Occupation numbers

The bosonic and fermionic occupation numbers occurring in the various flow equations are given by

$$n_B(x) = \frac{1}{e^{\frac{x}{T}} - 1} \quad , \quad n_F(x) = \frac{1}{e^{\frac{x}{T}} + 1} \, . \tag{C.1}$$

C.1.2. Regulators

We use the following 3-dimensional Litim regulators

$$R_{k,F}(\vec{p}) = -\mathrm{i}\vec{p}\cdot\vec{\gamma}(\sqrt{\tfrac{k^2}{\vec{p}^2}} - 1)\theta(k^2 - \vec{p}^2)\,, \tag{C.2}$$

$$R_{k,B}(\vec{p}) = (k^2 - \vec{q}^2)\theta(k^2 - \vec{p}^2)\,. \tag{C.3}$$

C.1.3. Flow of the effective potential

The sigma and pion loop in the Wetterich equation take the following form after inner traces and the loop integration have been performed

$$\mathcal{J}_\sigma + \mathcal{J}_\pi = \frac{k^4}{6\pi^2\left(k^2+m_\sigma^2+q_0^2\right)} \tag{C.4}$$

$$+\frac{k^4\left(N_f^2-1\right)}{6\pi^2\left(k^2+m_\pi^2+q_0^2\right)}\,. \tag{C.5}$$

This leaves the Matsubara sum, which can be performed analytically, giving

$$\partial_k U_{k,B} = \frac{k^4}{12\pi^2}\left[\frac{1+2n_B(\epsilon_k^\sigma)}{\epsilon_k^\sigma}+\frac{(N_f^2-1)(1+2n_B(\epsilon_k^\pi))}{\epsilon_k^\pi}\right]. \tag{C.6}$$

Analogous the fermion loop in the Wetterich equation for the effective potential gives after traces and loop integration

$$\mathcal{J}_\psi = -\frac{2k^4N_cN_f}{3\pi^2\left(k^2+m_\psi^2+(q_0+i\mu)^2\right)}\,. \tag{C.7}$$

After Matsubara sum the fermionic contribution to the potential flow reads

$$\partial_k U_{k,F} = -\frac{N_cN_fk^4}{3\pi^2}\left[\frac{1-n_F(\epsilon_k^\psi-\mu)-n_F(\epsilon_k^\psi+\mu)}{\epsilon_k^\psi}\right]. \tag{C.8}$$

C.1.4. Flow of dressings for spectral functions

The RG flow equations for the dressings B_k and C_k can directly be calculated by the projections in Eq. 4.12 applied to the two-point flow equation in Fig. 4.1. The first of the field indices indicates which field is being regulated. Explicit expressions are given in the following.

$$\begin{aligned}
&\partial_k B_{k,\sigma\psi}(\omega) = \\
&\frac{h^2k^4m_\psi N_cN_f}{24\pi^2}\Bigg(\frac{-n_F(\epsilon_k^\psi)-\epsilon_k^\sigma n_B'(\epsilon_k^\sigma)-(-n_B(\epsilon_k^\sigma)-1)}{\epsilon_k^\psi(\epsilon_k^\sigma)^3(-\epsilon_k^\psi-\epsilon_k^\sigma+\omega)} \\
&+\frac{n_F(\epsilon_k^\psi)-\epsilon_k^\sigma n_B'(\epsilon_k^\sigma)+n_B(\epsilon_k^\sigma)}{\epsilon_k^\psi(\epsilon_k^\sigma)^3(-\epsilon_k^\psi+\epsilon_k^\sigma+\omega)} \\
&+\frac{-(1-n_F(\epsilon_k^\psi))+\epsilon_k^\sigma n_B'(\epsilon_k^\sigma)-n_B(\epsilon_k^\sigma)}{\epsilon_k^\psi(\epsilon_k^\sigma)^3(\epsilon_k^\psi+\epsilon_k^\sigma+\omega)} \\
&+\frac{(1-n_F(\epsilon_k^\psi))+\epsilon_k^\sigma n_B'(\epsilon_k^\sigma)+(-n_B(\epsilon_k^\sigma)-1)}{\epsilon_k^\psi(\epsilon_k^\sigma)^3(\epsilon_k^\psi-\epsilon_k^\sigma+\omega)} \\
&+\frac{-(1-n_F(\epsilon_k^\psi))-(-n_B(\epsilon_k^\sigma)-1)}{\epsilon_k^\psi(\epsilon_k^\sigma)^2(\epsilon_k^\psi-\epsilon_k^\sigma+\omega)^2}+\frac{-(1-n_F(\epsilon_k^\psi))-n_B(\epsilon_k^\sigma)}{\epsilon_k^\psi(\epsilon_k^\sigma)^2(\epsilon_k^\psi+\epsilon_k^\sigma+\omega)^2} \\
&+\frac{n_F(\epsilon_k^\psi)+(-n_B(\epsilon_k^\sigma)-1)}{\epsilon_k^\psi(\epsilon_k^\sigma)^2(-\epsilon_k^\psi-\epsilon_k^\sigma+\omega)^2}+\frac{n_F(\epsilon_k^\psi)+n_B(\epsilon_k^\sigma)}{\epsilon_k^\psi(\epsilon_k^\sigma)^2(-\epsilon_k^\psi+\epsilon_k^\sigma+\omega)^2}\Bigg)
\end{aligned}$$

$$\partial_k C_{k,\sigma\psi}(\omega) = \tag{C.9}$$
$$\frac{h^2k^4N_cN_f}{24\pi^2}\Bigg(\frac{-n_F(\epsilon_k^\psi)+\epsilon_k^\sigma n_B'(\epsilon_k^\sigma)-n_B(\epsilon_k^\sigma)}{(\epsilon_k^\sigma)^3(\epsilon_k^\psi-\epsilon_k^\sigma+\omega)}$$
$$+\frac{-n_F(\epsilon_k^\psi)+\epsilon_k^\sigma n_B'(\epsilon_k^\sigma)-n_B(\epsilon_k^\sigma)}{(\epsilon_k^\sigma)^3(-\epsilon_k^\psi+\epsilon_k^\sigma+\omega)}$$
$$+\frac{n_F(\epsilon_k^\psi)+\epsilon_k^\sigma n_B'(\epsilon_k^\sigma)-n_B(\epsilon_k^\sigma)-1}{(\epsilon_k^\sigma)^3(-\epsilon_k^\psi-\epsilon_k^\sigma+\omega)}+\frac{n_F(\epsilon_k^\psi)+\epsilon_k^\sigma n_B'(\epsilon_k^\sigma)-n_B(\epsilon_k^\sigma)-1}{(\epsilon_k^\sigma)^3(\epsilon_k^\psi+\epsilon_k^\sigma+\omega)}$$
$$+\frac{-n_F(\epsilon_k^\psi)-n_B(\epsilon_k^\sigma)}{(\epsilon_k^\sigma)^2(-\epsilon_k^\psi+\epsilon_k^\sigma+\omega)^2}+\frac{-n_F(\epsilon_k^\psi)+n_B(\epsilon_k^\sigma)+1}{(\epsilon_k^\sigma)^2(-\epsilon_k^\psi-\epsilon_k^\sigma+\omega)^2}$$
$$+\frac{n_F(\epsilon_k^\psi)-n_B(\epsilon_k^\sigma)-1}{(\epsilon_k^\sigma)^2(\epsilon_k^\psi+\epsilon_k^\sigma+\omega)^2}+\frac{n_F(\epsilon_k^\psi)+n_B(\epsilon_k^\sigma)}{(\epsilon_k^\sigma)^2(\epsilon_k^\psi-\epsilon_k^\sigma+\omega)^2}\Bigg)$$

$$\partial_k B_{k,\pi\psi}(\omega) = \frac{h^2k^4m_\psi N_c(N_f-1)^2(N_f+1)^2}{36\pi^2}\Bigg(\tag{C.10}$$
$$+\frac{-\epsilon_k^\pi n_B'(\epsilon_k^\pi)+n_B(\epsilon_k^\pi)-n_F(\epsilon_k^\psi)+1}{(\epsilon_k^\pi)^3\epsilon_k^\psi(\epsilon_k^\pi+\epsilon_k^\psi+\omega)}+\frac{-\epsilon_k^\pi n_B'(\epsilon_k^\pi)+n_B(\epsilon_k^\pi)+n_F(\epsilon_k^\psi)}{(\epsilon_k^\pi)^3\epsilon_k^\psi(-\epsilon_k^\pi+\epsilon_k^\psi+\omega)}$$
$$+\frac{\epsilon_k^\pi n_B'(\epsilon_k^\pi)-n_B(\epsilon_k^\pi)-n_F(\epsilon_k^\psi)}{(\epsilon_k^\pi)^3\epsilon_k^\psi(\epsilon_k^\pi-\epsilon_k^\psi+\omega)}+\frac{\epsilon_k^\pi n_B'(\epsilon_k^\pi)-n_B(\epsilon_k^\pi)+n_F(\epsilon_k^\psi)-1}{(\epsilon_k^\pi)^3\epsilon_k^\psi(-\epsilon_k^\pi-\epsilon_k^\psi+\omega)}$$
$$+\frac{-n_B(\epsilon_k^\pi)-n_F(\epsilon_k^\psi)}{(\epsilon_k^\pi)^2\epsilon_k^\psi(\epsilon_k^\pi-\epsilon_k^\psi+\omega)^2}+\frac{-n_B(\epsilon_k^\pi)-n_F(\epsilon_k^\psi)}{(\epsilon_k^\pi)^2\epsilon_k^\psi(-\epsilon_k^\pi+\epsilon_k^\psi+\omega)^2}$$
$$+\frac{n_B(\epsilon_k^\pi)-n_F(\epsilon_k^\psi)+1}{(\epsilon_k^\pi)^2\epsilon_k^\psi(-\epsilon_k^\pi-\epsilon_k^\psi+\omega)^2}+\frac{n_B(\epsilon_k^\pi)-n_F(\epsilon_k^\psi)+1}{(\epsilon_k^\pi)^2\epsilon_k^\psi(\epsilon_k^\pi+\epsilon_k^\psi+\omega)^2}\Bigg)$$

$$\partial_k C_{k,\pi\psi}(\omega) = \frac{h^2k^4N_c(N_f-1)^2(N_f+1)^2}{36\pi^2}\Bigg(\tag{C.11}$$
$$\frac{\epsilon_k^\pi n_B'(\epsilon_k^\pi)-n_B(\epsilon_k^\pi)-n_F(\epsilon_k^\psi)}{(\epsilon_k^\pi)^3(\epsilon_k^\pi-\epsilon_k^\psi+\omega)}+\frac{\epsilon_k^\pi n_B'(\epsilon_k^\pi)-n_B(\epsilon_k^\pi)-n_F(\epsilon_k^\psi)}{(\epsilon_k^\pi)^3(-\epsilon_k^\pi+\epsilon_k^\psi+\omega)}$$
$$+\frac{\epsilon_k^\pi n_B'(\epsilon_k^\pi)-n_B(\epsilon_k^\pi)+n_F(\epsilon_k^\psi)-1}{(\epsilon_k^\pi)^3(-\epsilon_k^\pi-\epsilon_k^\psi+\omega)}+\frac{\epsilon_k^\pi n_B'(\epsilon_k^\pi)-n_B(\epsilon_k^\pi)+n_F(\epsilon_k^\psi)-1}{(\epsilon_k^\pi)^3(\epsilon_k^\pi+\epsilon_k^\psi+\omega)}$$
$$+\frac{-n_B(\epsilon_k^\pi)-n_F(\epsilon_k^\psi)}{(\epsilon_k^\pi)^2(\epsilon_k^\pi-\epsilon_k^\psi+\omega)^2}+\frac{n_B(\epsilon_k^\pi)-n_F(\epsilon_k^\psi)+1}{(\epsilon_k^\pi)^2(-\epsilon_k^\pi-\epsilon_k^\psi+\omega)^2}$$
$$+\frac{-n_B(\epsilon_k^\pi)+n_F(\epsilon_k^\psi)-1}{(\epsilon_k^\pi)^2(\epsilon_k^\pi+\epsilon_k^\psi+\omega)^2}+\frac{n_B(\epsilon_k^\pi)+n_F(\epsilon_k^\psi)}{(\epsilon_k^\pi)^2(-\epsilon_k^\pi+\epsilon_k^\psi+\omega)^2}\Bigg)$$

$$\partial_k B_{k,\psi\sigma}(\omega) = \frac{h^2 k^4 m_\psi N_c N_f}{24\pi^2}\Bigg(\tag{C.12}$$
$$\frac{-\epsilon_k^\psi n_F'(\epsilon_k^\psi) + n_F(\epsilon_k^\psi) - n_B(\epsilon_k^\sigma) - 1}{(\epsilon_k^\psi)^3\epsilon_k^\sigma(\epsilon_k^\psi + \epsilon_k^\sigma + \omega)} + \frac{-\epsilon_k^\psi n_F'(\epsilon_k^\psi) + n_F(\epsilon_k^\psi) + n_B(\epsilon_k^\sigma)}{(\epsilon_k^\psi)^3\epsilon_k^\sigma(-\epsilon_k^\psi + \epsilon_k^\sigma + \omega)}$$
$$+\frac{\epsilon_k^\psi n_F'(\epsilon_k^\psi) - n_F(\epsilon_k^\psi) - n_B(\epsilon_k^\sigma)}{(\epsilon_k^\psi)^3\epsilon_k^\sigma(\epsilon_k^\psi - \epsilon_k^\sigma + \omega)} + \frac{\epsilon_k^\psi n_F'(\epsilon_k^\psi) - n_F(\epsilon_k^\psi) + n_B(\epsilon_k^\sigma) + 1}{(\epsilon_k^\psi)^3\epsilon_k^\sigma(-\epsilon_k^\psi - \epsilon_k^\sigma + \omega)}$$
$$+\frac{-n_F(\epsilon_k^\psi) - n_B(\epsilon_k^\sigma)}{(\epsilon_k^\psi)^2\epsilon_k^\sigma(\epsilon_k^\psi - \epsilon_k^\sigma + \omega)^2} + \frac{-n_F(\epsilon_k^\psi) - n_B(\epsilon_k^\sigma)}{(\epsilon_k^\psi)^2\epsilon_k^\sigma(-\epsilon_k^\psi + \epsilon_k^\sigma + \omega)^2}$$
$$+\frac{n_F(\epsilon_k^\psi) - n_B(\epsilon_k^\sigma) - 1}{(\epsilon_k^\psi)^2\epsilon_k^\sigma(-\epsilon_k^\psi - \epsilon_k^\sigma + \omega)^2} + \frac{n_F(\epsilon_k^\psi) - n_B(\epsilon_k^\sigma) - 1}{(\epsilon_k^\psi)^2\epsilon_k^\sigma(\epsilon_k^\psi + \epsilon_k^\sigma + \omega)^2}\Bigg)$$

$$\partial_k C_{k,\psi\sigma}(\omega) = \frac{h^2 k^4 N_c N_f}{24\pi^2}\Bigg($$
$$-\frac{n_F(\epsilon_k^\psi) + n_B(\epsilon_k^\sigma)}{\epsilon_k^\psi\epsilon_k^\sigma(\epsilon_k^\psi - \epsilon_k^\sigma + \omega)^2} + \frac{-n_F(\epsilon_k^\psi) + n_B(\epsilon_k^\sigma) + 1}{\epsilon_k^\psi\epsilon_k^\sigma(-\epsilon_k^\psi - \epsilon_k^\sigma + \omega)^2}$$
$$+\frac{n_F(\epsilon_k^\psi) - n_B(\epsilon_k^\sigma) - 1}{\epsilon_k^\psi\epsilon_k^\sigma(\epsilon_k^\psi + \epsilon_k^\sigma + \omega)^2} + \frac{n_F(\epsilon_k^\psi) + n_B(\epsilon_k^\sigma)}{\epsilon_k^\psi\epsilon_k^\sigma(-\epsilon_k^\psi + \epsilon_k^\sigma + \omega)^2}$$
$$-\frac{n_F'(\epsilon_k^\psi)}{\epsilon_k^\psi\epsilon_k^\sigma(-\epsilon_k^\psi - \epsilon_k^\sigma + \omega)} + \frac{n_F'(\epsilon_k^\psi)}{\epsilon_k^\psi\epsilon_k^\sigma(\epsilon_k^\psi - \epsilon_k^\sigma + \omega)}$$
$$+\frac{n_F'(\epsilon_k^\psi)}{\epsilon_k^\psi\epsilon_k^\sigma(-\epsilon_k^\psi + \epsilon_k^\sigma + \omega)} - \frac{n_F'(\epsilon_k^\psi)}{\epsilon_k^\psi\epsilon_k^\sigma(\epsilon_k^\psi + \epsilon_k^\sigma + \omega)}\Bigg)$$

$$\partial_k B_{k,\psi\pi}(\omega) = \frac{h^2 k^4 m_\psi N_c (N_f-1)^2(N_f+1)^2}{36\pi^2}\Bigg(\tag{C.13}$$
$$+\frac{-n_B(\epsilon_k^\pi) - \epsilon_k^\psi n_F'(\epsilon_k^\psi) + n_F(\epsilon_k^\psi) - 1}{\epsilon_k^\pi(\epsilon_k^\psi)^3(-\epsilon_k^\pi - \epsilon_k^\psi + \omega)} + \frac{n_B(\epsilon_k^\pi) - \epsilon_k^\psi n_F'(\epsilon_k^\psi) + n_F(\epsilon_k^\psi)}{\epsilon_k^\pi(\epsilon_k^\psi)^3(-\epsilon_k^\pi + \epsilon_k^\psi + \omega)}$$
$$+\frac{-n_B(\epsilon_k^\pi) + \epsilon_k^\psi n_F'(\epsilon_k^\psi) - n_F(\epsilon_k^\psi)}{\epsilon_k^\pi(\epsilon_k^\psi)^3(\epsilon_k^\pi - \epsilon_k^\psi + \omega)} + \frac{n_B(\epsilon_k^\pi) + \epsilon_k^\psi n_F'(\epsilon_k^\psi) - n_F(\epsilon_k^\psi) + 1}{\epsilon_k^\pi(\epsilon_k^\psi)^3(\epsilon_k^\pi + \epsilon_k^\psi + \omega)}$$
$$+\frac{n_B(\epsilon_k^\pi) - n_F(\epsilon_k^\psi) + 1}{\epsilon_k^\pi(\epsilon_k^\psi)^2(-\epsilon_k^\pi - \epsilon_k^\psi + \omega)^2} + \frac{n_B(\epsilon_k^\pi) - n_F(\epsilon_k^\psi) + 1}{\epsilon_k^\pi(\epsilon_k^\psi)^2(\epsilon_k^\pi + \epsilon_k^\psi + \omega)^2}$$
$$+\frac{n_B(\epsilon_k^\pi) + n_F(\epsilon_k^\psi)}{\epsilon_k^\pi(\epsilon_k^\psi)^2(\epsilon_k^\pi - \epsilon_k^\psi + \omega)^2} + \frac{n_B(\epsilon_k^\pi) + n_F(\epsilon_k^\psi)}{\epsilon_k^\pi(\epsilon_k^\psi)^2(-\epsilon_k^\pi + \epsilon_k^\psi + \omega)^2}\Bigg)$$

$$\partial_k C_{k,\psi\pi}(\omega) = \frac{h^2 k^4 N_c (N_f-1)^2 (N_f+1)^2}{36\pi^2}\Bigg($$
$$\frac{-n_B(\epsilon_k^\pi) - n_F(\epsilon_k^\psi)}{\epsilon_k^\pi \epsilon_k^\psi(-\epsilon_k^\pi + \epsilon_k^\psi + \omega)^2} + \frac{n_B(\epsilon_k^\pi) - n_F(\epsilon_k^\psi) + 1}{\epsilon_k^\pi \epsilon_k^\psi(-\epsilon_k^\pi - \epsilon_k^\psi + \omega)^2}$$
$$+\frac{-n_B(\epsilon_k^\pi) + n_F(\epsilon_k^\psi) - 1}{\epsilon_k^\pi \epsilon_k^\psi(\epsilon_k^\pi + \epsilon_k^\psi + \omega)^2} + \frac{n_B(\epsilon_k^\pi) + n_F(\epsilon_k^\psi)}{\epsilon_k^\pi \epsilon_k^\psi(\epsilon_k^\pi - \epsilon_k^\psi + \omega)^2}$$
$$-\frac{n_F'(\epsilon_k^\psi)}{\epsilon_k^\pi \epsilon_k^\psi(-\epsilon_k^\pi - \epsilon_k^\psi + \omega)} + \frac{n_F'(\epsilon_k^\psi)}{\epsilon_k^\pi \epsilon_k^\psi(\epsilon_k^\pi - \epsilon_k^\psi + \omega)}$$
$$+\frac{n_F'(\epsilon_k^\psi)}{\epsilon_k^\pi \epsilon_k^\psi(-\epsilon_k^\pi + \epsilon_k^\psi + \omega)} - \frac{n_F'(\epsilon_k^\psi)}{\epsilon_k^\pi \epsilon_k^\psi(\epsilon_k^\pi + \epsilon_k^\psi + \omega)}\Bigg)$$

Dirac-Sokhotsky identities

The following identities are useful when taking the $\epsilon \to 0$ in the imaginary parts of the retarded two-point functions

$$\begin{aligned}\lim_{\epsilon\to 0} \mathrm{Im}\frac{1}{\omega + i\epsilon \pm E_\alpha \pm E_\beta} &\to -\pi\delta(\omega \pm E_\alpha \pm E_\beta),\\ \lim_{\epsilon\to 0} \mathrm{Im}\frac{1}{(\omega + i\epsilon \pm E_\alpha \pm E_\beta)^2} &\to \pi\delta'(\omega \pm E_\alpha \pm E_\beta).\end{aligned} \tag{C.14}$$

C.2. Quark-meson Model in LPA'

C.2.1. Regulators

We use the following 3-dimensional LPA' modified Litim regulators

$$R_{k,F}(\vec{p}) = -\mathrm{i}Z_{F,k}\vec{p}\cdot\vec{\gamma}\left(\sqrt{\tfrac{k^2}{\vec{p}^2}} - 1\right)\theta(k^2 - \vec{p}^2)\,, \tag{C.15}$$
$$R_{k,B}(\vec{p}) = Z_{\sigma/\pi,k}(k^2 - \vec{q}^2)\theta(k^2 - \vec{p}^2)\,. \tag{C.16}$$

C.2.2. Flow of the effective potential

The LPA' modified bosonic loops in the Wetterich equation before Matsubara summation look like

$$\mathcal{J}_\sigma + \mathcal{J}_\pi = \frac{k^4(\sigma_0^2(kY_{\phi,k}' + 5Y_{\phi,k}) + kZ_{\phi,k}' + 5Z_{\phi,k})}{30\pi^2((k^2+q_0^2)(\sigma_0^2 Y_{\phi,k} + Z_{\phi,k}) + m_\sigma^2)} \tag{C.17}$$
$$+\frac{k^4(N_f^2-1)(kZ_{\phi,k}' + 5Z_{\phi,k})}{30\pi^2((k^2+q_0^2)Z_{\phi,k} + m_\pi^2)}\,. \tag{C.18}$$

The bosonic contribution to the flow of the effective potential, after performing the Matsubara sum look like

$$\begin{aligned}\partial_k U_{k,B} = &\frac{k^4}{60\pi^2}\left[\frac{\big(1+2n_B(E_k^\sigma)\big)(5Z_{\sigma,k}+k\partial_k Z_{\sigma,k})}{E_k^\sigma Z_{\sigma,k}}\right] \\ &+\frac{k^4}{60\pi^2}\left[\frac{(N_f^2-1)\big(1+2n_B(E_k^\pi)\big)(5Z_{\pi,k}+k\partial_k Z_{\pi,k})}{E_k^\pi Z_{\pi,k}}\right].\end{aligned} \tag{C.19}$$

In a similar manner the fermion loop in LPA' looks like

$$\mathcal{J}_\psi \;=\; -\frac{k^4 N_c N_f Z_{F,k}(kZ'_{F,k}+4Z_{F,k})}{6\pi^2(m_\psi^2+Z_{F,k}^2(k^2+(q_0+i\mu)^2))}\,. \tag{C.20}$$

Performing the analytic Matsubara sum gives

$$\partial_k U_{k,F} = -\frac{N_c N_f k^4}{12\pi^2}\left[\frac{\big(1-n_F(E_k^\psi-\mu)-n_F(E_k^\psi+\mu)\big)(4Z_{F,k}+k\partial_k Z_{F,k})}{E_k^\psi Z_{F,k}}\right]. \tag{C.21}$$

C.2.3. Flow of wave function renormalization factors

The flow equations for the wave function renormalization factors can be extracted from the projections in Eq. 4.61 and Eq. 4.62 applied to the flow of the two-point functions in Fig. 4.9 and Fig. 4.10. Here the first of the external field indices refers to the regulated field.

$$\begin{aligned}&(\partial_k Z_\pi)_{\sigma,\pi} = \\ &\frac{2k^4(N_f^2-1)\sigma_0^2(U_k'')^2)Z_{\phi,k}(\sigma_0^2 Y_{\phi,k}+Z_{\phi,k})}{3\pi^2(E_k^\pi)^3(E_k^\sigma)^3\left(Z_{\phi,k}\left(m_\pi^2-m_\sigma^2\right)+m_\pi^2\sigma_0^2 Y_{\phi,k}\right)^3}\times \\ &\Bigg(Z_{\phi,k}\Big(-2(E_k^\pi)^3 n_B(E_k^\sigma)(-4k^2Z_{\phi,k}+m_\pi^2-5m_\sigma^2) \\ &+2(E_k^\pi)^3E_k^\sigma m_\pi^2 n'_B(E_k^\sigma)-2(E_k^\pi)^3E_k^\sigma m_\sigma^2 n'_B(E_k^\sigma)+4(E_k^\pi)^3k^2Z_{\phi,k} \\ &+(E_k^\pi)^3(-m_\pi^2)+5(E_k^\pi)^3m_\sigma^2-2(E_k^\sigma)^3n_B(E_k^\pi)(\\ &4k^2Z_{\phi,k}+5m_\pi^2-m_\sigma^2)+2E_k^\pi(E_k^\sigma)^3m_\pi^2n'_B(E_k^\pi) \\ &-2E_k^\pi(E_k^\sigma)^3m_\sigma^2n'_B(E_k^\pi)-4(E_k^\sigma)^3k^2Z_{\phi,k}-5(E_k^\sigma)^3m_\pi^2+(E_k^\sigma)^3m_\sigma^2\Big) \\ &+\sigma_0^2Y_{\phi,k}\Big(-2(E_k^\pi)^3n_B(E_k^\sigma)(m_\pi^2-4k^2Z_{\phi,k})+2(E_k^\pi)^3E_k^\sigma m_\pi^2n'_B(E_k^\sigma) \\ &+4(E_k^\pi)^3k^2Z_{\phi,k}+(E_k^\pi)^3(-m_\pi^2) \\ &-2(E_k^\sigma)^3n_B(E_k^\pi)(4k^2Z_{\phi,k}+5m_\pi^2)+2E_k^\pi(E_k^\sigma)^3m_\pi^2n'_B(E_k^\pi) \\ &-4(E_k^\sigma)^3k^2Z_{\phi,k}-5(E_k^\sigma)^3m_\pi^2\Big)\Bigg)\end{aligned} \tag{C.22}$$

$$
\begin{aligned}
&(\partial_k Z_\pi)_{\pi,\sigma} = \\
&\frac{2k^4\left(N_f^2-1\right)\sigma_0^2(U_k'')^2 Z_{\phi,k}\left(\sigma_0^2 Y_{\phi,k}+Z_{\phi,k}\right)}{3\pi^2(E_k^\pi)^3(E_k^\sigma)^3\left(Z_{\phi,k}\left(m_\pi^2-m_\sigma^2\right)+m_\pi^2\sigma_0^2 Y\right)^3}\times \\
&\Bigg(\sigma_0^2 Y_{\phi,k}\Big(-2(E_k^\pi)^3 n_B(E_k^\sigma)\left(m_\pi^2-4k^2 Z_{\phi,k}\right)+2(E_k^\pi)^3 E_k^\sigma m_\pi^2 n_B'(E_k^\sigma) \\
&+4(E_k^\pi)^3 k^2 Z_{\phi,k}+(E_k^\pi)^3\left(-m_\pi^2\right)-2(E_k^\sigma)^3 n_B(E_k^\pi)\left(4k^2 Z_{\phi,k}+5m_\pi^2\right) \\
&+2E_k^\pi(E_k^\sigma)^3 m_\pi^2 n_B'(E_k^\pi)-4(E_k^\sigma)^3 k^2 Z_{\phi,k}-5(E_k^\sigma)^3 m_\pi^2\Big)+ \\
&Z_{\phi,k}\Big(-2(E_k^\pi)^3 n_B(E_k^\sigma)\left(-4k^2 Z_{\phi,k}+m_\pi^2-5m_\sigma^2\right)+2(E_k^\pi)^3 E_k^\sigma m_\pi^2 n_B'(E_k^\sigma) \\
&-2(E_k^\pi)^3 E_k^\sigma m_\sigma^2 n_B'(E_k^\sigma)+4(E_k^\pi)^3 k^2 Z_{\phi,k}+(E_k^\pi)^3\left(-m_\pi^2\right)+5(E_k^\pi)^3 m_\sigma^2 \\
&-2(E_k^\sigma)^3 n_B(E_k^\pi)\left(4k^2 Z_{\phi,k}+5m_\pi^2-m_\sigma^2\right)+2E_k^\pi(E_k^\sigma)^3 m_\pi^2 n_B'(E_k^\pi) \\
&-2E_k^\pi(E_k^\sigma)^3 m_\sigma^2 n_B'(E_k^\pi)-4(E_k^\sigma)^3 k^2 Z_{\phi,k}-5(E_k^\sigma)^3 m_\pi^2+(E_k^\sigma)^3 m_\sigma^2\Big)\Bigg)
\end{aligned}
\tag{C.23}
$$

$$
\begin{aligned}
&(\partial_k Z_\pi)_F = \\
&\frac{h^2 k^2 N_c\left(N_f^2-1\right)}{18\pi^2(E_k^\psi)^5 Z_{F,k}^7}\times \\
&\Bigg(k^5 Z_{F,k}^4 Z_{F,k}' n_F''(E_k^\psi+\mu)+2k^4 Z_{F,k}^5 n_F''(E_k^\psi+\mu)+k^3 m_\psi^2 Z_{F,k}^2 Z_{F,k}' n_F''(E_k^\psi+\mu) \\
&-E_k^\psi k^3 Z_{F,k}^4 Z_{F,k}' n_F'(E_k^\psi+\mu)+k^3 Z_{F,k}^4 n_F(E_k^\psi+\mu) Z_{F,k}'+2k^2 m_\psi^2 Z_{F,k}^3 n_F''(E_k^\psi+\mu) \\
&-3E_k^\psi k^2 Z_{F,k}^5 n_F'(E_k^\psi+\mu)+3k^2 Z_{F,k}^5 n_F(E_k^\psi+\mu)+2E_k^\psi k m_\psi^2 Z_{F,k}^2 Z_{F,k}' n_F'(E_k^\psi+\mu) \\
&+3E_k^\psi m_\psi^2 Z_{F,k}^3 n_F'(E_k^\psi+\mu)-2k m_\psi^2 Z_{F,k}^2 n_F(E_k^\psi+\mu) Z_{F,k}'-3m_\psi^2 Z_{F,k}^3 n_F(E_k^\psi+\mu)\Bigg) \\
&-\frac{h^2 k^2 N_c\left(N_f^2-1\right)}{18\pi^2(E_k^\psi)^5 Z_{F,k}^7}\times \\
&\Bigg(k^5\left(-Z_{F,k}^4\right) Z_{F,k}' n_F''(E_k^\psi-\mu)-2k^4 Z_{F,k}^5 n_F''(E_k^\psi-\mu)-k^3 m_\psi^2 Z_{F,k}^2 Z_{F,k}' n_F''(E_k^\psi-\mu) \\
&+E_k^\psi k^3 Z_{F,k}^4 Z_{F,k}' n_F'(E_k^\psi-\mu)+k^3 Z_{F,k}^4(1-n_F(E_k^\psi-\mu))Z_{F,k}'-2k^2 m_\psi^2 Z_{F,k}^3 n_F''(E_k^\psi-\mu) \\
&+3E_k^\psi k^2 Z_{F,k}^5 n_F'(E_k^\psi-\mu)+3k^2 Z_{F,k}^5(1-n_F(E_k^\psi-\mu))-2E_k^\psi k m_\psi^2 Z_{F,k}^2 Z_{F,k}' n_F'(E_k^\psi-\mu) \\
&-3E_k^\psi m_\psi^2 Z_{F,k}^3 n_F'(E_k^\psi-\mu)-2k m_\psi^2 Z_{F,k}^2(1-n_F(E_k^\psi-\mu))Z_{F,k}' \\
&-3m_\psi^2 Z_{F,k}^3(1-n_F(E_k^\psi-\mu))\Bigg)
\end{aligned}
\tag{C.24}
$$

$$
\begin{aligned}
&(\partial_k Z_\sigma)_\sigma = \qquad \text{(C.25)}\\
&-\frac{k^4\left(2\sigma_0^3 U_k^{(3)}+3\sigma_0 U_k''\right)^2}{36\pi^2 (E_k^\sigma)^7\left(\sigma_0^2 Y_{\phi,k}+Z_{\phi,k}\right)^3}\times\\
&\left(\sigma_0^2 Y_{\phi,k}\left(-2E_k^\sigma k^2 n_B^{(3)}(E_k^\sigma)+12k^2 n_B''(E_k^\sigma)-30E_k^\sigma n_B'(E_k^\sigma)+30n_B(E_k^\sigma)+15\right)\right.\\
&+Z_{\phi,k}\left(-2E_k^\sigma k^2 n_B^{(3)}(E_k^\sigma)+12k^2 n_B''(E_k^\sigma)-30E_k^\sigma n_B'(E_k^\sigma)+30n_B(E_k^\sigma)+15\right)\\
&\left.+2m_\sigma\left(6n_B''(E_k^\sigma)-E_k^\sigma n_B^{(3)}(E_k^\sigma)\right)\right)
\end{aligned}
$$

$$
\begin{aligned}
&(\partial_k Z_\sigma)_\pi = \qquad \text{(C.26)}\\
&\frac{k^4\left(N_f^2-1\right)\sigma_0 (U_k'')^2}{36\pi^2 (E_k^\pi)^7 Z_{\phi,k}^3}\times\\
&\left(Z_{\phi,k}\left(2E_k^\pi k^2 n_B^{(3)}(E_k^\pi)-12k^2 n_B''(E_k^\pi)+30E_k^\pi n_B'(E_k^\pi)-30n_B(E_k^\pi)-15\right)\right.\\
&\left.+2m_\pi^2\left(E_k^\pi n_B^{(3)}(E_k^\pi)-6n_B''(E_k^\pi)\right)\right)
\end{aligned}
$$

$$
\begin{aligned}
(\partial_k Z_\sigma)_F = {} & \frac{h^2 k^2 N_c N_f}{36\pi^2 (E_k^\psi)^7 Z_{F,k}^9} \times \\
& \Big(3k^7 Z_{F,k}^6 Z'_{F,k} n''_F(E_k^\psi + \mu) + 6k^6 Z_{F,k}^7 n''_F(E_k^\psi + \mu) + 6k^5 m_\psi^2 Z_{F,k}^4 Z'_{F,k} n''_F(E_k^\psi + \mu) \\
& - 3E_k^\psi k^5 Z_{F,k}^6 Z'_{F,k} n'_F(E_k^\psi + \mu) + 3k^5 Z_{F,k}^6 n_F(E_k^\psi + \mu) Z'_{F,k} \\
& + E_k^\psi k^4 m_\psi^2 Z_{F,k}^5 n_F^{(3)}(E_k^\psi + \mu) + 6k^4 m_\psi^2 Z_{F,k}^5 n''_F(E_k^\psi + \mu) \\
& - 9E_k^\psi k^4 Z_{F,k}^7 n'_F(E_k^\psi + \mu) + 9k^4 Z_{F,k}^7 n_F(E_k^\psi + \mu) + 3k^3 m_\psi^4 Z_{F,k}^2 Z'_{F,k} n''_F(E_k^\psi + \mu) \\
& + 3E_k^\psi k^3 m_\psi^2 Z_{F,k}^4 Z'_{F,k} n'_F(E_k^\psi + \mu) - 3k^3 m_\psi^2 Z_{F,k}^4 n_F(E_k^\psi + \mu) Z'_{F,k} \\
& + E_k^\psi k^2 m_\psi^4 Z_{F,k}^3 n_F^{(3)}(E_k^\psi + \mu) + 15E_k^\psi k^2 m_\psi^2 Z_{F,k}^5 n'_F(E_k^\psi + \mu) \\
& - 15k^2 m_\psi^2 Z_{F,k}^5 n_F(E_k^\psi + \mu) + 6E_k^\psi k m_\psi^4 Z_{F,k}^2 Z'_{F,k} n'_F(E_k^\psi + \mu) \\
& + 9E_k^\psi m_\psi^4 Z_{F,k}^3 n'_F(E_k^\psi + \mu) - 6k m_\psi^4 Z_{F,k}^2 n_F(E_k^\psi + \mu) Z'_{F,k} - 9m_\psi^4 Z_{F,k}^3 n_F(E_k^\psi + \mu) \Big) \\
& - \frac{h^2 k^2 N_c N_f}{36\pi^2 (E_k^\psi)^7 Z_{F,k}^9} \times \\
& \Big(- 3k^7 Z_{F,k}^6 Z'_{F,k} n''_F(E_k^\psi - \mu) - 6k^6 Z_{F,k}^7 n''_F(E_k^\psi - \mu) - 6k^5 m_\psi^2 Z_{F,k}^4 Z'_{F,k} n''_F(E_k^\psi - \mu) \\
& + 3E_k^\psi k^5 Z_{F,k}^6 Z'_{F,k} n'_F(E_k^\psi - \mu) + 3k^5 Z_{F,k}^6 (1 - n_F(E_k^\psi - \mu)) Z'_{F,k} \\
& - E_k^\psi k^4 m_\psi^2 Z_{F,k}^5 n_F^{(3)}(E_k^\psi - \mu) - 6k^4 m_\psi^2 Z_{F,k}^5 n''_F(E_k^\psi - \mu) \\
& + 9E_k^\psi k^4 Z_{F,k}^7 n'_F(E_k^\psi - \mu) + 9k^4 Z_{F,k}^7 (1 - n_F(E_k^\psi - \mu)) - 3k^3 m_\psi^4 Z_{F,k}^2 Z'_{F,k} n''_F(E_k^\psi - \mu) \\
& - 3E_k^\psi k^3 m_\psi^2 Z_{F,k}^4 Z'_{F,k} n'_F(E_k^\psi - \mu) - 3k^3 m_\psi^2 Z_{F,k}^4 (1 - n_F(E_k^\psi - \mu)) Z'_{F,k} \\
& - E_k^\psi k^2 m_\psi^4 Z_{F,k}^3 n_F^{(3)}(E_k^\psi - \mu) - 15E_k^\psi k^2 m_\psi^2 Z_{F,k}^5 n'_F(E_k^\psi - \mu) \\
& - 15k^2 m_\psi^2 Z_{F,k}^5 (1 - n_F(E_k^\psi - \mu)) - 6E_k^\psi k m_\psi^4 Z_{F,k}^2 Z'_{F,k} n'_F(E_k^\psi - \mu) \\
& - 9E_k^\psi m_\psi^4 Z_{F,k}^3 n'_F(E_k^\psi - \mu) - 6k m_\psi^4 Z_{F,k}^2 (1 - n_F(E_k^\psi - \mu)) Z'_{F,k} \\
& - 9m_\psi^4 Z_{F,k}^3 (1 - n_F(E_k^\psi - \mu)) \Big)
\end{aligned}
$$

The flow equations for the fermionic wave function renormalizations are left out here for brevity, they can be calculated analogously.

C.3. Parity-doublet Model in LPA

C.3.1. Regulators

We use the following 3-dimensional Litim regulators

$$R_{k,F}(\vec{p}) = -\mathrm{i}\vec{p}\cdot\vec{\gamma}(\sqrt{\tfrac{k^2}{\vec{p}^2}}-1)\theta(k^2-\vec{p}^2)\,, \tag{C.27}$$

$$R_{k,B}(\vec{p}) = (k^2-\vec{q}^2)\theta(k^2-\vec{p}^2)\,. \tag{C.28}$$

C.3.2. Flow of the effective potential

The bosonic loop contributions before taking the Matsubara sum look like

$$\begin{aligned}\mathcal{J}_\sigma+\mathcal{J}_\pi &= \frac{k^4}{6\pi^2\left(k^2+m_\sigma^2+q_0^2\right)} &\text{(C.29)}\\ &\quad+\frac{k^4\left(N_f^2-1\right)}{6\pi^2\left(k^2+m_\pi^2+q_0^2\right)}\,. &\text{(C.30)}\end{aligned}$$

Performing the analytic Matsubara sum yields

$$\begin{aligned}\partial_k U_{k,B} &= \frac{k^4}{12\pi^2}\left[\frac{1+2n_B(\epsilon_k^\sigma)}{\epsilon_k^\sigma}+\frac{(N_f^2-1)(1+2n_B(\epsilon_k^\pi))}{\epsilon_k^\pi}\right]\\ &= \frac{k^4}{12\pi^2}\left[\frac{1}{\epsilon_k^\sigma}\coth\left(\frac{\epsilon_k^\sigma}{2T}\right)+\frac{3}{\epsilon_k^\pi}\coth\left(\frac{\epsilon_k^\pi}{2T}\right)\right]\,.\end{aligned} \tag{C.31}$$

The fermionic loop contribution before Matsubara summation takes the form

$$\begin{aligned}\mathcal{J}_\psi &= -\frac{2k^4N_f}{3\pi^2}\Big(2k^2+2m_0^2+m_1^2+m_2^2+2(q_0-i\mu)^2\Big)\Big/ &\text{(C.32)}\\ &\quad\Big(\big(k^4+k^2(2m_0^2+m_1^2+m_2^2+2(q_0-i\mu)^2\big)+\\ &\quad\big(m_0^2+(\mu+m_1+iq_0)(-\mu+m_2-iq_0)\big)\times\\ &\quad\big(m_0^2+(-\mu+m_1-iq_0)(\mu+m_2+iq_0)\big)\big)\Big)\,,\end{aligned}$$

where $m_{1/2}=h_{1/2}\sigma$.

Performing the Matsubara sum gives

$$\begin{aligned}\partial_k U_{k,F} &= -\frac{N_f k^4}{6\pi^2}\sum_\pm\frac{\epsilon_k^\pm(1-n_F(\epsilon_k^\mp+\tilde{\mu}_B))-\epsilon_k^\pm n_F(\epsilon_k^\mp+\tilde{\mu}_B)}{\epsilon_k^\mp\epsilon_k^\pm}\\ &= -\frac{N_f k^4}{6\pi^2}\sum_\pm\left[\frac{2(k^2+m_0^2-\epsilon_k^{\pm 2})+(h_1^2+h_2^2)\sigma^2}{(\epsilon_k^{\mp 2}-\epsilon_k^{\pm 2})\epsilon_k^\pm}\right.\\ &\quad\left.\times\left(\tanh\left(\tfrac{\epsilon_k^\pm+\tilde{\mu}_B}{2T}\right)+\tanh\left(\tfrac{\epsilon_k^\pm-\tilde{\mu}_B}{2T}\right)\right)\right]\,.\end{aligned} \tag{C.33}$$

C.4. Parity-doublet Model LPA'

C.4.1. Regulators

We use the following 3-dimensional Litim regulators

$$R_{k,F}(\vec{p}) = -\mathrm{i}\vec{p}\cdot\vec{\gamma}(\sqrt{\tfrac{k^2}{\vec{p}^2}}-1)\theta(k^2-\vec{p}^2)\,, \tag{C.34}$$

$$R_{k,B}(\vec{p}) = Z_{\phi,k}(k^2-\vec{q}^2)\theta(k^2-\vec{p}^2)\,. \tag{C.35}$$

C.4.2. Flow of the effective potential

The loop contributions in the Wetterich equation from pions and sigma meson are

$$\begin{aligned}\mathcal{J}_\sigma+\mathcal{J}_\pi &= \frac{k^4\left(kZ'_{\phi,k}+5Z_{\phi,k}\right)}{30\pi^2\left(\left(k^2+q_0^2\right)Z_{\phi,k}+m_\sigma^2\right)} &\text{(C.36)}\\ &\quad+\frac{k^4\left(N_f^2-1\right)\left(kZ'_{\phi,k}+5Z_{\phi,k}\right)}{30\pi^2\left(\left(k^2+q_0^2\right)Z_{\phi,k}+m_\pi^2\right)}\,. &\text{(C.37)}\end{aligned}$$

Analytically performing the Matsubara sum gives

$$\begin{aligned}\partial_k U_{k,B} = &\frac{k^4}{60\pi^2}\left[\frac{\big(1+2n_B(E_k^\sigma)\big)(5Z_{\phi,k}+k\partial_k Z_{\phi,k})}{E_k^\sigma Z_{\phi,k}}\right]\\ &+\frac{k^4}{60\pi^2}\left[\frac{(N_f^2-1)\big(1+2n_B(E_k^\pi)\big)(5Z_{\phi,k}+k\partial_k Z_{\phi,k})}{E_k^\pi Z_{\phi,k}}\right].\end{aligned} \tag{C.38}$$

C.4.3. Flow of $Z_{\phi,k}$

The flow equations for $Z_{\phi,k}$ can be directly obtained by the respective equations for $Z_{\pi,k}$ in Sec. C.2, by setting $Z_{\pi,k}=Z_{\phi,k}$. Only the nucleon loop has to be calculated separately due to the block structure of the inverse nucleon propagator in Eq. 5.2, resulting in rather long and complicated expressions we want to spare the reader here.

C.5. $O(4)$ Action and N-point Functions to $\mathcal{O}(\partial^2)$

The bosonic part of the action used in Sec. 4.2 is the action of a O(4) model. In a consistent derivative expansion up to $\mathcal{O}(\partial^2)$ this action looks like

$$\Gamma_k[\phi] = \int d^4x' \Big(\frac{1}{2} Z_{\phi,k} (\partial_\mu \phi(x'))^2 + \frac{1}{8} Y_{\phi,k} (\partial_\mu \phi^2(x'))^2 + U_k(\phi^2(x')) \Big), \tag{C.39}$$

where $U_k(\phi^2)$ is an arbitrary potential function of the invariant ϕ^2. As will be shown later on, this ansatz allows for a $O(4)$ invariant treatment of the radial σ and Goldstone modes $\vec{\pi}$ of the model, when a non-vanishing expectation value in the σ-direction is assumed $\phi_0 = \sigma \delta_{1i}$.

Two-point function

We start with the two-point function. By taking two functional derivatives in coordinate space we get

$$\begin{aligned}
\Gamma^{(2)}_{\phi_a \phi_b}(x,y) &= \frac{\delta^2 \Gamma_k[\phi]}{\delta\phi_b(y)\delta\phi_a(x)} \\
&= Z_{\phi,k}\delta_{ab} \int_p p^2 e^{\mathrm{i}p(x-y)} \\
&+ \tfrac{1}{2} Y_{\phi,k}\delta_{ab} \int_p (\mathrm{i}p_\mu) \Big(e^{\mathrm{i}p(y-x)} (\partial^\mu \phi^2_m(y)) + e^{\mathrm{i}p(x-y)} (\partial^\mu \phi^2_m(x)) \Big) \\
&+ Y_{\phi,k} \int_{x'} \Big(\partial_\mu \delta^{(4)}(x'-x)\phi_a(x') \Big) \Big(\partial^\mu \delta^{(4)}(x'-y)\phi_b(x') \Big) \\
&+ \Big(2U^{(1)}_k(\phi^2_m(x))\delta_{ab} + 4U^{(2)}_k(\phi^2_m(x))\phi_a(x)\phi_b(x) \Big) \delta^{(4)}(x-y)
\end{aligned} \tag{C.40}$$

Now we can set the field to its vacuum expectation value $\phi_0 = \sigma\delta_{1i}$ and insert a suitable number of auxiliary momentum integrations to get rid of the delta functions.

$$\begin{aligned}
\Gamma^{(2)}_{ab}(x,y) &= \frac{\delta^2 \Gamma_k[\phi]}{\delta\phi_b(y)\delta\phi_a(x)}\Big|_{\phi=\phi_0} \\
&= \int_p p^2 e^{\mathrm{i}p(x-y)} \Big(Z_{\phi,k}\delta_{ab} + Y_{\phi,k}\sigma^2\delta_{a1}\delta_{b1} \Big) \\
&\quad + \int_p e^{\mathrm{i}p(x-y)} \Big(2U^{(1)}_k(\sigma^2)\delta_{ab} + 4\sigma^2 U^{(2)}_k(\sigma^2)\delta_{a1}\delta_{b1} \Big)
\end{aligned} \tag{C.41}$$

Now we Fourier transform the above result to get the momentum space representations, which gives the following for two-point function

$$\begin{aligned}
\Gamma^{(2)}_{ab}(q,r) &= \int_x \int_y \Gamma^{(2)}_{ab}(x,y) e^{-\mathrm{i}qx} e^{-\mathrm{i}ry} \\
&= \Big(q^2 (Z_{\phi,k}\delta_{ab} + Y_{\phi,k}\sigma^2\delta_{a1}\delta_{b1}) + \\
&\quad 2U^{(1)}_k(\sigma^2)\delta_{ab} + 4\sigma^2 U^{(2)}_k(\sigma^2)\delta_{a1}\delta_{b1} \Big) (2\pi)^4 \delta^{(4)}(q+r).
\end{aligned} \tag{C.42}$$

3-point function

For completeness we also want to give the respective expressions for the 3- and 4-point functions.

For the 3-point function

$$\begin{aligned}
&\Gamma^{(3)}_{\phi_a\phi_b\phi_c}(x,y,z) = \frac{\delta^3\Gamma_k[\phi]}{\delta\phi_c(z)\delta\phi_b(y)\delta\phi_a(x)} \qquad \text{(C.43)}\\
&= Y_{\phi,k}\delta_{ab}\int_p (\mathrm{i}p_\mu)\Big(e^{\mathrm{i}p(y-x)}\partial^\mu\delta^{(4)}(y-z)\phi_c(y) + \\
&\quad e^{\mathrm{i}p(x-y)}\partial^\mu\delta^{(4)}(x-z)\phi_c(x)\Big) + \\
&Y_{\phi,k}\delta_{ac}\int_{x'}\Big(\partial_\mu\delta^{(4)}(x'-x)\delta^{(4)}(x'-z)\Big)\Big(\partial^\mu\delta^{(4)}(x'-y)\phi_b(x')\Big)\\
&+Y_{\phi,k}\delta_{bc}\int_{x'}\Big(\partial_\mu\delta^{(4)}(x'-x)\phi_a(x')\Big)\Big(\partial^\mu\delta^{(4)}(x'-y)\delta^{(4)}(x'-z)\Big)\\
&+4U_k^{(2)}(\phi_m^2(x))\Big(\delta_{ab}\phi_c(x)+\delta_{ac}\phi_b(x)+\delta_{bc}\phi_a(x)\Big)\delta^{(4)}(x-y)\delta^{(4)}(x-z)\\
&+8U_k^{(3)}(\phi_m^2(x))\phi_a(x)\phi_b(x)\phi_c(x)\delta^{(4)}(x-y)\delta^{(4)}(x-z)\ .
\end{aligned}$$

Plugging in the vacuum expectation value for ϕ we find

$$\begin{aligned}
&\Gamma^{(3)}_{abc}(x,y,z) = \frac{\delta^3\Gamma_k[\phi]}{\delta\phi_c(z)\delta\phi_b(y)\delta\phi_a(x)}\Big|_{\phi=\phi_0} \qquad \text{(C.44)}\\
&= Y_{\phi,k}\delta_{ab}\delta_{c1}\sigma\int_p\int_{p'}(\mathrm{i}p_\mu)(\mathrm{i}p'^\mu)\Big(e^{\mathrm{i}p(y-x)}e^{\mathrm{i}p'(y-z)}+e^{\mathrm{i}p(x-y)}e^{\mathrm{i}p'(x-z)}\Big)\\
&+Y_{\phi,k}\delta_{ac}\delta_{b1}\sigma\int_p\int_{p'}(\mathrm{i}p_\mu)(\mathrm{i}p'^\mu)\Big(e^{\mathrm{i}p(z-x)}e^{\mathrm{i}p'(z-y)}+e^{\mathrm{i}p(x-z)}e^{\mathrm{i}p'(x-y)}\Big)\\
&+Y_{\phi,k}\delta_{bc}\delta_{a1}\sigma\int_p\int_{p'}(\mathrm{i}p_\mu)(\mathrm{i}p'^\mu)\Big(e^{\mathrm{i}p(z-x)}e^{\mathrm{i}p'(z-y)}+e^{\mathrm{i}p(y-x)}e^{\mathrm{i}p'(y-z)}\Big)\\
&+4\sigma U_k^{(2)}(\sigma^2)\Big(\delta_{ab}\delta_{c1}+\delta_{ac}\delta_{b1}+\delta_{bc}\delta_{a1}\Big)\delta^{(4)}(x-y)\delta^{(4)}(x-z)\\
&+8\sigma^3U_k^{(3)}(\sigma^2)\delta_{a1}\delta_{b1}\delta_{c1}\delta^{(4)}(x-y)\delta^{(4)}(x-z)\ .
\end{aligned}$$

The 3-point function in momentum space then reads

$$\begin{aligned}
&\Gamma^{(3)}_{abc}(q,r,s) = \int_x\int_y\int_z\Gamma^{(3)}_{abc}(x,y,z)e^{-\mathrm{i}qx}e^{-\mathrm{i}ry}e^{-\mathrm{i}sz} \qquad \text{(C.45)}\\
&= \Big(-Y_{\phi,k}\sigma\big(\delta_{ab}\delta_{c1}(q+r)s+Y_{\phi,k}\delta_{ac}\delta_{b1}(q+s)r+\delta_{bc}\delta_{a1}(r+s)q\big)+\\
&\quad 4\sigma U_k^{(2)}(\sigma^2)\big(\delta_{ab}\delta_{c1}+\delta_{ac}\delta_{b1}+\delta_{bc}\delta_{a1}\big)+\\
&\quad 8\sigma^3U_k^{(3)}(\sigma^2)\delta_{a1}\delta_{b1}\delta_{c1}\Big)(2\pi)^4\delta^{(4)}(q+r+s)\ .
\end{aligned}$$

4-point function

Moving on to the 4-point function, we will for brevity just give the result in momentum space

$$\Gamma^{(4)}_{abcd}(q,r,s,t) = \int_x \int_y \int_z \int_{z'} \Gamma^{(4)}_{abcd}(x,y,z,z') e^{-\mathrm{i}qx} e^{-\mathrm{i}ry} e^{-\mathrm{i}sz} e^{-\mathrm{i}tz'} \tag{C.46}$$

$$\begin{aligned}
&= \Big(- Y_{\phi,k}\big(\delta_{ab}\delta_{cd}(q+r)(s+t) + \delta_{ac}\delta_{bd}(q+s)(r+t) \\
&\quad + \delta_{bc}\delta_{ad}(r+s)(q+t)\big) \\
&\quad + 4U_k^{(2)}(\sigma^2)\big(\delta_{ab}\delta_{cd} + \delta_{ac}\delta_{bd} + \delta_{bc}\delta_{ad}\big) \\
&\quad + 8U_k^{(3)}(\sigma^2)\big(\delta_{ab}\delta_{c1}\delta_{d1} + \delta_{ac}\delta_{b1}\delta_{d1} + \delta_{bc}\delta_{a1}\delta_{d1} \\
&\quad + \delta_{ad}\delta_{b1}\delta_{c1} + \delta_{bd}\delta_{a1}\delta_{c1} + \delta_{cd}\delta_{a1}\delta_{b1}\big) + 16\sigma^4 U_k^{(4)}(\sigma^2)\delta_{a1}\delta_{b1}\delta_{c1}\delta_{d1}\Big) \cdot \\
&\quad (2\pi)^4 \delta^{(4)}(q+r+s+t) \; .
\end{aligned}$$

Bibliography

[1] H. Yukawa, "On the Interaction of Elementary Particles I," *Proc. Phys. Math. Soc. Jap.* **17** (1935) 48–57. [Prog. Theor. Phys. Suppl.1,1(1935)].

[2] C. M. G. Lattes, H. Muirhead, G. P. S. Occhialini, and C. F. Powell, "PROCESSES INVOLVING CHARGED MESONS," *Nature* **159** (1947) 694–697. [,42(1947)].

[3] S. Weinberg, "Phenomenological Lagrangians," *Physica* **A96** (1979) 327–340.

[4] M. Gell-Mann, "A Schematic Model of Baryons and Mesons," *Phys. Lett.* **8** (1964) 214–215.

[5] H. Fritzsch, M. Gell-Mann, and H. Leutwyler, "Advantages of the Color Octet Gluon Picture," *Phys. Lett.* **47B** (1973) 365–368.

[6] S. Bethke, "alphas 2016," *Nuclear and Particle Physics Proceedings* **282-284** (2017) 149 – 152. 19th International Conference in Quantum Chromodynamics.

[7] M. Breidenbach, J. I. Friedman, H. W. Kendall, E. D. Bloom, D. H. Coward, H. DeStaebler, J. Drees, L. W. Mo, and R. E. Taylor, "Observed behavior of highly inelastic electron-proton scattering," *Phys. Rev. Lett.* **23** (1969) 935–939.

[8] D. J. Gross and F. Wilczek, "Ultraviolet behavior of non-abelian gauge theories," *Phys. Rev. Lett.* **30** (1973) 1343–1346.

[9] H. D. Politzer, "Reliable perturbative results for strong interactions?," *Phys. Rev. Lett.* **30** (1973) 1346–1349.

[10] J. Greensite, ed., *An Introduction to the Confinement Problem*, vol. 821 of *Lecture Notes in Physics, Berlin Springer Verlag*. 2011.

[11] P. Braun-Munzinger and J. Stachel, "The quest for the quark-gluon plasma," *Nature* **448** (2007) 302–309.

[12] S. Borsanyi, Z. Fodor, C. Hoelbling, S. D. Katz, S. Krieg, C. Ratti, and K. K. Szabó, "Is there still any tc mystery in lattice qcd? results with physical masses in the continuum limit iii," *Journal of High Energy Physics* **2010** (2010) 73.

[13] **HotQCD Collaboration** Collaboration, A. Bazavov, T. Bhattacharya, C. DeTar, H.-T. Ding, S. Gottlieb, R. Gupta, P. Hegde, U. M. Heller, F. Karsch, E. Laermann, *et al.*, "Equation of state in $(2+1)$-flavor qcd," *Phys. Rev. D* **90** (2014) 094503.

[14] F. Becattini, "An Introduction to the Statistical Hadronization Model," in *International School on Quark-Gluon Plasma and Heavy Ion Collisions: past, present, future Villa Gualino, Torino, Italy, December 8-14, 2008*. 2009. `arXiv:0901.3643 [hep-ph]`. `http://inspirehep.net/record/811687/files/arXiv:0901.3643.pdf`.

[15] J. Stachel, A. Andronic, P. Braun-Munzinger, and K. Redlich, "Confronting lhc data with the statistical hadronization model," *Journal of Physics: Conference Series* **509** (2014) 012019.

[16] T. Matsui and H. Satz, "J/ψ suppression by quark-gluon plasma formation," *Physics Letters B* **178** (1986) 416 – 422.

[17] H. Satz, "A Brief history of J/Ψ suppression," in *Quarkonium production in high-energy nuclear collisions. Proceedings, Winter Workshop, RHIC/INT'98, Seattle, USA, May 11-15, 1998*, pp. 1–8. 1998. `arXiv:hep-ph/9806319 [hep-ph]`.

[18] R. Rapp and J. Wambach, "Chiral symmetry restoration and dileptons in relativistic heavy ion collisions," *Adv. Nucl. Phys.* **25** (2000) 1, `arXiv:hep-ph/9909229 [hep-ph]`.

[19] R. Rapp, G. Chanfray, and J. Wambach, "Rho meson propagation and dilepton enhancement in hot hadronic matter," *Nuclear Physics A* **617** (1997) 472 – 495.

[20] P. M. Hohler and R. Rapp, "Is rho-meson melting compatible with chiral restoration?," *Physics Letters B* **731** (2014) 103 – 109.

[21] D. Adamová, G. Agakichiev, D. Antończyk, H. Appelshäuser, V. Belaga, J. Bielcikova, P. Braun-Munzinger, O. Busch, A. Cherlin, S. Damjanović, *et al.*, "Modification of the rho meson detected by low-mass electron-positron pairs," *Physics Letters B* **666** (2008) 425 – 429.

[22] **NA60** Collaboration, R. Arnaldi *et al.*, "NA60 results on thermal dimuons," *Eur. Phys. J.* **C61** (2009) 711–720, `arXiv:0812.3053 [nucl-ex]`.

[23] F. Geurts, "The star dilepton physics program," *Nuclear Physics A* **904-905** (2013) 217c – 224c. The Quark Matter 2012.

[24] Y. Aoki, Z. Fodor, S. D. Katz, and K. K. Szabo, "The QCD transition temperature: Results with physical masses in the continuum limit," *Phys. Lett.* **B643** (2006) 46–54, arXiv:hep-lat/0609068 [hep-lat].

[25] P. de Forcrand and O. Philipsen, "The Chiral critical line of N(f) = 2+1 QCD at zero and non-zero baryon density," *JHEP* **01** (2007) 077, arXiv:hep-lat/0607017 [hep-lat].

[26] **HotQCD** Collaboration, C. E. Detar and R. Gupta, "Toward a precise determination of T(c) with 2+1 flavors of quarks," *PoS* **LATTICE2007** (2007) 179, arXiv:0710.1655 [hep-lat].

[27] F. Karsch, "Recent lattice results on finite temperature and density QCD. Part II.," *PoS* **LATTICE2007** (2007) 015, arXiv:0711.0661 [hep-lat].

[28] U. Vogl and W. Weise, "The Nambu and Jona Lasinio model: Its implications for hadrons and nuclei," *Prog. Part. Nucl. Phys.* **27** (1991) 195–272.

[29] T. Hatsuda and T. Kunihiro, "QCD phenomenology based on a chiral effective Lagrangian," *Phys. Rept.* **247** (1994) 221–367, arXiv:hep-ph/9401310 [hep-ph].

[30] M. Buballa, "NJL model analysis of quark matter at large density," *Phys. Rept.* **407** (2005) 205–376, arXiv:hep-ph/0402234 [hep-ph].

[31] B.-J. Schaefer and J. Wambach, "The Phase diagram of the quark meson model," *Nucl.Phys.* **A757** (2005) 479–492, arXiv:nucl-th/0403039 [nucl-th].

[32] C. Ratti, M. A. Thaler, and W. Weise, "Phases of QCD: Lattice thermodynamics and a field theoretical model," *Phys. Rev.* **D73** (2006) 014019, arXiv:hep-ph/0506234 [hep-ph].

[33] S. Roessner, C. Ratti, and W. Weise, "Polyakov loop, diquarks and the two-flavour phase diagram," *Phys. Rev.* **D75** (2007) 034007, arXiv:hep-ph/0609281 [hep-ph].

[34] K. Fukushima, "Phase diagrams in the three-flavor Nambu-Jona-Lasinio model with the Polyakov loop," *Phys. Rev.* **D77** (2008) 114028, arXiv:0803.3318 [hep-ph]. [Erratum: Phys. Rev.D78,039902(2008)].

[35] B.-J. Schaefer, J. M. Pawlowski, and J. Wambach, "The Phase Structure of the Polyakov–Quark-Meson Model," *Phys. Rev.* **D76** (2007) 074023, arXiv:0704.3234 [hep-ph].

[36] T. K. Herbst, J. M. Pawlowski, and B.-J. Schaefer, "The phase structure of the Polyakov–quark–meson model beyond mean field," *Phys. Lett.* **B696** (2011) 58–67, arXiv:1008.0081 [hep-ph].

[37] S. Carignano, D. Nickel, and M. Buballa, "Influence of vector interaction and Polyakov loop dynamics on inhomogeneous chiral symmetry breaking phases," *Phys. Rev.* **D82** (2010) 054009, arXiv:1007.1397 [hep-ph].

[38] M. Buballa and S. Carignano, "Inhomogeneous chiral condensates," *Prog. Part. Nucl. Phys.* **81** (2015) 39–96, arXiv:1406.1367 [hep-ph].

[39] S. Carignano, M. Buballa, and B.-J. Schaefer, "Inhomogeneous phases in the quark-meson model with vacuum fluctuations," *Phys. Rev.* **D90** (2014) 014033, arXiv:1404.0057 [hep-ph].

[40] M. Buballa and S. Carignano, "Inhomogeneous chiral symmetry breaking in dense neutron-star matter," *Eur. Phys. J.* **A52** (2016) 57, arXiv:1508.04361 [nucl-th].

[41] F. J. Dyson, "The s matrix in quantum electrodynamics," *Phys. Rev.* **75** (1949) 1736–1755.

[42] J. Schwinger, "On the green's functions of quantized fields. i," *Proceedings of the National Academy of Sciences* **37** (1951) 452–455, http://www.pnas.org/content/37/7/452.full.pdf.

[43] J. Schwinger, "On the green's functions of quantized fields. ii," *Proceedings of the National Academy of Sciences* **37** (1951) 455–459, http://www.pnas.org/content/37/7/455.full.pdf.

[44] R. Alkofer and L. von Smekal, "The Infrared behavior of QCD Green's functions: Confinement dynamical symmetry breaking, and hadrons as relativistic bound states," *Phys. Rept.* **353** (2001) 281, arXiv:hep-ph/0007355 [hep-ph].

[45] C. D. Roberts and A. G. Williams, "Dyson-schwinger equations and their application to hadronic physics," *Progress in Particle and Nuclear Physics* **33** (1994) 477 – 575.

[46] P. Maris and C. D. Roberts, "Dyson–schwinger equations: A tool for hadron physics," *International Journal of Modern Physics E* **12** (2003) 297–365, https://www.worldscientific.com/doi/pdf/10.1142/S0218301303001326.

[47] C. S. Fischer, "Infrared properties of qcd from dyson–schwinger equations," *Journal of Physics G: Nuclear and Particle Physics* **32** (2006) R253.

[48] G. Eichmann, H. Sanchis-Alepuz, R. Williams, R. Alkofer, and C. S. Fischer, "Baryons as relativistic three-quark bound states," *Prog. Part. Nucl. Phys.* **91** (2016) 1–100, arXiv:1606.09602 [hep-ph].

[49] C. D. Roberts and S. M. Schmidt, "Dyson-Schwinger equations: Density, temperature and continuum strong QCD," *Prog. Part. Nucl. Phys.* **45** (2000) S1–S103, arXiv:nucl-th/0005064 [nucl-th].

[50] C. S. Fischer, "Deconfinement phase transition and the quark condensate," *Phys. Rev. Lett.* **103** (2009) 052003, arXiv:0904.2700 [hep-ph].

[51] C. S. Fischer and J. A. Mueller, "Chiral and deconfinement transition from Dyson-Schwinger equations," *Phys. Rev.* **D80** (2009) 074029, arXiv:0908.0007 [hep-ph].

[52] C. S. Fischer, A. Maas, and J. A. Muller, "Chiral and deconfinement transition from correlation functions: SU(2) vs. SU(3)," *Eur. Phys. J.* **C68** (2010) 165–181, arXiv:1003.1960 [hep-ph].

[53] C. S. Fischer, J. Luecker, and J. A. Mueller, "Chiral and deconfinement phase transitions of two-flavour QCD at finite temperature and chemical potential," *Phys. Lett.* **B702** (2011) 438–441, arXiv:1104.1564 [hep-ph].

[54] C. S. Fischer, J. Luecker, and C. A. Welzbacher, "Locating the critical end point of QCD," *Nucl. Phys.* **A931** (2014) 774–779, arXiv:1410.0124 [hep-ph].

[55] B. C. Barrois, "Superconducting quark matter," *Nuclear Physics B* **129** (1977) 390 – 396.

[56] S. C. Frautschi, "ASYMPTOTIC FREEDOM AND COLOR SUPERCONDUCTIVITY IN DENSE QUARK MATTER," in *Workshop on Theoretical Physics: Hadronic Matter at Extreme Energy Density Erice, Italy, October 13-21, 1978*, p. 18. 1978.

[57] M. G. Alford, K. Rajagopal, and F. Wilczek, "QCD at finite baryon density: Nucleon droplets and color superconductivity," *Phys. Lett.* **B422** (1998) 247–256, arXiv:hep-ph/9711395 [hep-ph].

[58] R. Rapp, T. Schäfer, E. V. Shuryak, and M. Velkovsky, "Diquark Bose condensates in high density matter and instantons," *Phys. Rev. Lett.* **81** (1998) 53–56, arXiv:hep-ph/9711396 [hep-ph].

[59] D. Nickel, J. Wambach, and R. Alkofer, "Color-superconductivity in the strong-coupling regime of Landau gauge QCD," *Phys. Rev.* **D73** (2006) 114028, arXiv:hep-ph/0603163 [hep-ph].

[60] D. Nickel, R. Alkofer, and J. Wambach, "On the unlocking of color and flavor in color-superconducting quark matter," *Phys. Rev.* **D74** (2006) 114015, arXiv:hep-ph/0609198 [hep-ph].

[61] D. Müller, M. Buballa, and J. Wambach, "Dyson-Schwinger approach to color superconductivity at finite temperature and density," *Eur. Phys. J.* **A49** (2013) 96, arXiv:1303.2693 [hep-ph].

[62] J. Walecka, "A theory of highly condensed matter," *Annals of Physics* **83** (1974) 491–529.

[63] T. D. Lee and G. C. Wick, "Vacuum Stability and Vacuum Excitation in a Spin 0 Field Theory," *Phys. Rev.* **D9** (1974) 2291–2316.

[64] G. Sauer, H. Chandra, and U. Mosel, "Thermal properties of nuclei," *Nucl. Phys.* **A264** (1976) 221–243.

[65] B. Friman, C. Hohne, J. Knoll, S. Leupold, J. Randrup, R. Rapp, and P. Senger, "The CBM physics book: Compressed baryonic matter in laboratory experiments," *Lect. Notes Phys.* **814** (2011) pp.1–980.

[66] C. Wetterich, "Exact evolution equation for the effective potential," *Physics Letters B* **301** (1993) 90–94.

[67] J. Berges, N. Tetradis, and C. Wetterich, "Nonperturbative renormalization flow in quantum field theory and statistical physics," *Phys.Rept.* **363** (2002) 223–386, arXiv:hep-ph/0005122 [hep-ph].

[68] J. M. Pawlowski, "Aspects of the functional renormalisation group," *Annals Phys.* **322** (2007) 2831–2915, arXiv:hep-th/0512261 [hep-th].

[69] H. Gies, "Introduction to the functional RG and applications to gauge theories," *Lect.Notes Phys.* **852** (2012) 287–348, arXiv:hep-ph/0611146 [hep-ph].

[70] J. Braun, "Fermion Interactions and Universal Behavior in Strongly Interacting Theories," *J.Phys.* **G39** (2012) 033001, arXiv:1108.4449 [hep-ph].

[71] J. Braun, L. M. Haas, F. Marhauser, and J. M. Pawlowski, "Phase Structure of Two-Flavor QCD at Finite Chemical Potential," *Phys. Rev. Lett.* **106** (2011) 022002, arXiv:0908.0008 [hep-ph].

[72] M. Mitter, J. M. Pawlowski, and N. Strodthoff, "Chiral symmetry breaking in continuum QCD," *Phys. Rev.* **D91** (2015) 054035, arXiv:1411.7978 [hep-ph].

[73] B.-J. Schaefer and J. Wambach, "Renormalization group approach towards the QCD phase diagram," *Phys.Part.Nucl.* **39** (2008) 1025–1032, arXiv:hep-ph/0611191 [hep-ph].

[74] R.-A. Tripolt, B.-J. Schaefer, L. von Smekal, and J. Wambach, "Low-temperature behavior of the quark-meson model," *Phys. Rev.* **D97** (2018) 034022, arXiv:1709.05991 [hep-ph].

[75] N. Strodthoff, B.-J. Schaefer, and L. von Smekal, "Quark-meson-diquark model for two-color QCD," *Phys.Rev.* **D85** (2012) 074007, arXiv:1112.5401 [hep-ph].

[76] N. Strodthoff and L. von Smekal, "Polyakov-Quark-Meson-Diquark Model for two-color QCD," *Phys. Lett.* **B731** (2014) 350–357, arXiv:1306.2897 [hep-ph].

[77] K. Kamikado, N. Strodthoff, L. von Smekal, and J. Wambach, "Fluctuations in the quark-meson model for QCD with isospin chemical potential," *Phys. Lett.* **B718** (2013) 1044–1053, arXiv:1207.0400 [hep-ph].

[78] S. Floerchinger and C. Wetterich, "Chemical freeze-out in heavy ion collisions at large baryon densities," *Nucl.Phys.* **A890-891** (2012) 11–24, arXiv:1202.1671 [nucl-th].

[79] M. Drews, T. Hell, B. Klein, and W. Weise, "Thermodynamic phases and mesonic fluctuations in a chiral nucleon-meson model," *Phys.Rev.* **D88** (2013) 096011, arXiv:1308.5596 [hep-ph].

[80] M. Drews and W. Weise, "Functional renormalization group approach to neutron matter," *Phys.Lett.* **B738** (2014) 187–190, arXiv:1404.0882 [nucl-th].

[81] M. Drews and W. Weise, "From asymmetric nuclear matter to neutron stars: a functional renormalization group study," *Phys.Rev.* **C91** (2015) 035802, arXiv:1412.7655 [nucl-th].

[82] J. Weyrich, N. Strodthoff, and L. von Smekal, "Chiral mirror-baryon-meson model and nuclear matter beyond mean-field approximation," *Phys. Rev.* **C92** (2015) 015214, arXiv:1504.02697 [nucl-th].

[83] S. Floerchinger, "Analytic Continuation of Functional Renormalization Group Equations," *JHEP* **05** (2012) 021, arXiv:1112.4374 [hep-th].

[84] K. Kamikado, N. Strodthoff, L. von Smekal, and J. Wambach, "Real-time correlation functions in the $O(N)$ model from the functional renormalization group," *Eur.Phys.J.* **C74** (2014) 2806, arXiv:1302.6199 [hep-ph].

[85] R.-A. Tripolt, N. Strodthoff, L. von Smekal, and J. Wambach, "Spectral Functions for the Quark-Meson Model Phase Diagram from the Functional Renormalization Group," *Phys.Rev.* **D89** (2014) 034010, arXiv:1311.0630 [hep-ph].

[86] R.-A. Tripolt, L. von Smekal, and J. Wambach, "Flow equations for spectral functions at finite external momenta," *Phys.Rev.* **D90** (2014) 074031, arXiv:1408.3512 [hep-ph].

[87] C. Jung, F. Rennecke, R.-A. Tripolt, L. von Smekal, and J. Wambach, "In-Medium Spectral Functions of Vector- and Axial-Vector Mesons from the Functional Renormalization Group," *Phys. Rev.* **D95** (2017) 036020, arXiv:1610.08754 [hep-ph].

[88] M. E. Peskin and D. V. Schroeder, *An Introduction to quantum field theory.* Addison-Wesley, Reading, USA, 1995. http://www.slac.stanford.edu/~mpeskin/QFT.html.

[89] S. Weinberg, *The Quantum theory of fields. Vol. 1: Foundations.* Cambridge University Press, 2005.

[90] S. Weinberg, *The quantum theory of fields. Vol. 2: Modern applications.* Cambridge University Press, 2013.

[91] S. Weinberg, "Nonabelian Gauge Theories of the Strong Interactions," *Phys. Rev. Lett.* **31** (1973) 494–497.

[92] G. 't Hooft, "Symmetry breaking through bell-jackiw anomalies," *Phys. Rev. Lett.* **37** (1976) 8–11.

[93] R. D. Pisarski, "Notes on the deconfining phase transition," in *QCD perspectives on hot and dense matter. Proceedings, NATO Advanced Study Institute, Summer School, Cargese, France, August 6-18, 2001*, pp. 353–384. 2002. `arXiv:hep-ph/0203271 [hep-ph]`.

[94] S. Hands, J. B. Kogut, M.-P. Lombardo, and S. E. Morrison, "Symmetries and spectrum of SU(2) lattice gauge theory at finite chemical potential," *Nucl. Phys.* **B558** (1999) 327–346, `arXiv:hep-lat/9902034 [hep-lat]`.

[95] S. Hands, S. Kim, and J.-I. Skullerud, "Deconfinement in dense 2-color QCD," *Eur. Phys. J.* **C48** (2006) 193, `arXiv:hep-lat/0604004 [hep-lat]`.

[96] S. Cotter, P. Giudice, S. Hands, and J.-I. Skullerud, "Towards the phase diagram of dense two-color matter," *Phys. Rev. D* **87** (2013) 034507.

[97] T. Boz, S. Cotter, L. Fister, D. Mehta, and J.-I. Skullerud, "Phase transitions and gluodynamics in 2-colour matter at high density," *The European Physical Journal A* **49** (2013) 87.

[98] J. Engels, J. Fingberg, and M. Weber, "Finite size scaling analysis of su(2) lattice gauge theory in (3 + 1) dimensions," *Nuclear Physics B* **332** (1990) 737 – 759.

[99] A. Maas, L. von Smekal, B. Wellegehausen, and A. Wipf, "The phase diagram of a gauge theory with fermionic baryons," *Phys.Rev.* **D86** (2012) 111901, `arXiv:1203.5653 [hep-lat]`.

[100] B. H. Wellegehausen, A. Maas, A. Wipf, and L. von Smekal, "Hadron masses and baryonic scales in G_2-QCD at finite density," *Phys.Rev.* **D89** (2014) 056007, `arXiv:1312.5579 [hep-lat]`.

[101] P. de Forcrand and O. Philipsen, "Qcd phase diagram for small densities from simulations at imaginary μ," *Nuclear Physics B - Proceedings Supplements* **119** (2003) 535 – 537. Proceedings of the XXth International Symposium on Lattice Field Theory.

[102] O. Kaczmarek, F. Karsch, E. Laermann, C. Miao, S. Mukherjee, P. Petreczky, C. Schmidt, W. Soeldner, and W. Unger, "Phase boundary for the chiral transition in $(2 + 1)$-flavor qcd at small values of the chemical potential," *Phys. Rev. D* **83** (2011) 014504.

[103] G. Endrődi, Z. Fodor, S. D. Katz, Szabó, and K. K., "The qcd phase diagram at nonzero quark density," *Journal of High Energy Physics* **2011** (2011) 1.

[104] D. Sexty, "Simulating full QCD at nonzero density using the complex Langevin equation," *Phys.Lett.* **B729** (2014) 108–111, arXiv:1307.7748 [hep-lat].

[105] M. Cristoforetti, F. Di Renzo, G. Eruzzi, A. Mukherjee, C. Schmidt, L. Scorzato, and C. Torrero, "An efficient method to compute the residual phase on a lefschetz thimble," *Phys. Rev. D* **89** (2014) 114505.

[106] J. Langelage, S. Lottini, and O. Philipsen, "Centre symmetric 3d effective actions for thermal su(n) yang-mills from strong coupling series," *Journal of High Energy Physics* **2011** (2011) 57.

[107] M. Fromm, J. Langelage, S. Lottini, M. Neuman, and O. Philipsen, "Onset Transition to Cold Nuclear Matter from Lattice QCD with Heavy Quarks," *Phys.Rev.Lett.* **110** (2013) 122001, arXiv:1207.3005 [hep-lat].

[108] J. Langelage, M. Neuman, and O. Philipsen, "Heavy dense QCD and nuclear matter from an effective lattice theory," *JHEP* **1409** (2014) 131, arXiv:1403.4162 [hep-lat].

[109] P. de Forcrand and M. Fromm, "Nuclear Physics from lattice QCD at strong coupling," *Phys.Rev.Lett.* **104** (2010) 112005, arXiv:0907.1915 [hep-lat].

[110] P. de Forcrand, J. Langelage, O. Philipsen, and W. Unger, "Lattice QCD Phase Diagram In and Away from the Strong Coupling Limit," *Phys.Rev.Lett.* **113** (2014) 152002, arXiv:1406.4397 [hep-lat].

[111] P. Scior and L. von Smekal, "Baryonic matter onset in two-color qcd with heavy quarks," *Phys. Rev. D* **92** (2015) 094504.

[112] A. L. Blum, M. Q. Huber, M. Mitter, and L. von Smekal, "Gluonic three-point correlations in pure landau gauge qcd," *Phys. Rev. D* **89** (2014) 061703.

[113] G. Eichmann, R. Williams, R. Alkofer, and M. Vujinovic, "Three-gluon vertex in landau gauge," *Phys. Rev. D* **89** (2014) 105014.

[114] A. C. Aguilar, D. Binosi, D. Ibañez, and J. Papavassiliou, "New method for determining the quark-gluon vertex," *Phys. Rev. D* **90** (2014) 065027.

[115] R. Williams, "The quark-gluon vertex in Landau gauge bound-state studies," *Eur. Phys. J.* **A51** (2015) 57, arXiv:1404.2545 [hep-ph].

[116] A. K. Cyrol, M. Q. Huber, and L. v. Smekal, "A dyson–schwinger study of the four-gluon vertex," *The European Physical Journal C* **75** (2015) 102.

[117] R. Williams, C. S. Fischer, and W. Heupel, "Light mesons in qcd and unquenching effects from the 3pi effective action," *Phys. Rev. D* **93** (2016) 034026.

[118] M. Q. Huber, "Correlation functions of three-dimensional yang-mills theory from dyson-schwinger equations," *Phys. Rev. D* **93** (2016) 085033.

[119] M. Q. Huber, "On non-primitively divergent vertices of Yang–Mills theory," *Eur. Phys. J.* **C77** (2017) 733, arXiv:1709.05848 [hep-ph].

[120] L. P. Kadanoff, "Scaling laws for Ising models near T(c)," *Physics* **2** (1966) 263–272.

[121] P. C. Hohenberg and B. I. Halperin, "Theory of dynamic critical phenomena," *Rev. Mod. Phys.* **49** (1977) 435–479.

[122] K. G. Wilson and J. B. Kogut, "The Renormalization group and the epsilon expansion," *Phys. Rept.* **12** (1974) 75–200.

[123] K. G. Wilson, "The Renormalization Group: Critical Phenomena and the Kondo Problem," *Rev. Mod. Phys.* **47** (1975) 773.

[124] I. Boettcher, J. M. Pawlowski, and S. Diehl, "Ultracold atoms and the Functional Renormalization Group," *Nucl. Phys. Proc. Suppl.* **228** (2012) 63–135, arXiv:1204.4394 [cond-mat.quant-gas].

[125] I. Boettcher, T. Herbst, J. Pawlowski, N. Strodthoff, L. von Smekal, *et al.*, "Sarma phase in relativistic and non-relativistic systems," *Phys.Lett.* **B742** (2015) 86–93, arXiv:1409.5232 [cond-mat.quant-gas].

[126] W. Metzner, M. Salmhofer, C. Honerkamp, V. Meden, and K. Schönhammer, "Functional renormalization group approach to correlated fermion systems," *Rev. Mod. Phys.* **84** (2012) 299–352.

[127] R. Percacci, "Asymptotic Safety," arXiv:0709.3851 [hep-th].

[128] D. F. Litim, "Fixed Points of Quantum Gravity and the Renormalisation Group," arXiv:0810.3675 [hep-th]. [PoSQG-Ph,024(2007)].

[129] M. Reuter and F. Saueressig, "Quantum Einstein Gravity," *New J. Phys.* **14** (2012) 055022, arXiv:1202.2274 [hep-th].

[130] D. F. Litim and J. M. Pawlowski, "On gauge invariant Wilsonian flows," in *The exact renormalization group. Proceedings, Workshop, Faro, Portugal, September 10-12, 1998*, pp. 168–185. 1998. arXiv:hep-th/9901063 [hep-th]. https://inspirehep.net/record/482330/files/arXiv:hep-th_9901063.pdf.

[131] O. J. Rosten, "Fundamentals of the Exact Renormalization Group," *Phys. Rept.* **511** (2012) 177–272, arXiv:1003.1366 [hep-th].

[132] L. von Smekal, "Universal Aspects of QCD-like Theories," *Nucl. Phys. Proc. Suppl.* **228** (2012) 179–220, arXiv:1205.4205 [hep-ph].

[133] P. Braun-Munzinger and J. Wambach, "The Phase Diagram of Strongly-Interacting Matter," *Rev.Mod.Phys.* **81** (2009) 1031–1050, arXiv:0801.4256 [hep-ph].

[134] K. Fukushima and C. Sasaki, "The phase diagram of nuclear and quark matter at high baryon density," *Prog.Part.Nucl.Phys.* **72** (2013) 99–154, arXiv:1301.6377 [hep-ph].

[135] B. D. Serot and J. D. Walecka, "The Relativistic Nuclear Many Body Problem," *Adv.Nucl.Phys.* **16** (1986) 1–327.

[136] B. D. Serot and J. D. Walecka, "Recent progress in quantum hadrodynamics," *Int.J.Mod.Phys.* **E6** (1997) 515–631, arXiv:nucl-th/9701058 [nucl-th].

[137] **Particle Data Group** Collaboration, J. Beringer *et al.*, "Review of Particle Physics (RPP)," *Phys. Rev.* **D86** (2012) 010001.

[138] D. Jido, M. Oka, and A. Hosaka, "Chiral symmetry of baryons," *Prog. Theor. Phys.* **106** (2001) 873–908, arXiv:hep-ph/0110005 [hep-ph].

[139] S. Gallas and F. Giacosa, "Mirror versus naive assignment in chiral models for the nucleon," *Int.J.Mod.Phys.* **A29** (2014) 1450098, arXiv:1308.4817 [hep-ph].

[140] C. E. Detar and T. Kunihiro, "Linear σ Model With Parity Doubling," *Phys.Rev.* **D39** (1989) 2805.

[141] T. Hatsuda and M. Prakash, "Parity Doubling of the Nucleon and First Order Chiral Transition in Dense Matter," *Phys.Lett.* **B224** (1989) 11.

[142] D. Jido, Y. Nemoto, M. Oka, and A. Hosaka, "Chiral symmetry for positive and negative parity nucleons," *Nucl.Phys.* **A671** (2000) 471–480, arXiv:hep-ph/9805306 [hep-ph].

[143] L. Y. Glozman, "Confinement, chiral symmetry breaking and the mass generation of hadrons," *Acta Phys.Polon.Supp.* **6** (2013) 245–250, arXiv:1211.7267 [hep-ph].

[144] L. Y. Glozman, C. Lang, and M. Schrock, "Symmetries of hadrons after unbreaking the chiral symmetry," *Phys.Rev.* **D86** (2012) 014507, arXiv:1205.4887 [hep-lat].

[145] L. Y. Glozman, C. Lang, and M. Schrock, "Effects of the low lying Dirac modes on excited hadrons in lattice QCD," *Acta Phys.Polon.Supp.* **5** (2012) 1001–1006, arXiv:1207.7323 [hep-lat].

[146] T. Banks and A. Casher, "Chiral Symmetry Breaking in Confining Theories," *Nucl. Phys.* **B169** (1980) 103–125.

[147] T. D. Cohen and L. Y. Glozman, "Does one observe chiral symmetry restoration in baryon spectrum?," *Int.J.Mod.Phys.* **A17** (2002) 1327–1354, arXiv:hep-ph/0201242 [hep-ph].

[148] R. Jaffe, D. Pirjol, and A. Scardicchio, "Parity doubling among the baryons," *Phys.Rept.* **435** (2006) 157–182, arXiv:hep-ph/0602010 [hep-ph].

[149] M. Urban, M. Buballa, and J. Wambach, "Vector and axial vector correlators in a chirally symmetric model," *Nucl.Phys.* **A697** (2002) 338–371, arXiv:hep-ph/0102260 [hep-ph].

[150] S. Struber and D. H. Rischke, "Vector and axialvector mesons at nonzero temperature within a gauged linear sigma model," *Phys.Rev.* **D77** (2008) 085004, arXiv:0708.2389 [hep-th].

[151] E. E. Svanes and J. O. Andersen, "Functional renormalization group at finite density and Bose condensation," *Nucl.Phys.* **A857** (2011) 16–28, arXiv:1009.0430 [hep-ph].

[152] A. J. Helmboldt, J. M. Pawlowski, and N. Strodthoff, "Towards quantitative precision in the chiral crossover: masses and fluctuation scales," *Phys. Rev.* **D91** (2015) 054010, arXiv:1409.8414 [hep-ph].

[153] M. L. Goldberger and S. B. Treiman, "Conserved currents in the theory of fermi interactions," *Phys. Rev.* **110** (1958) 1478–1479.

[154] M. Gell-Mann, "Symmetries of baryons and mesons," *Phys. Rev.* **125** (1962) 1067–1084.

[155] C. Sasaki and I. Mishustin, "Thermodynamics of dense hadronic matter in a parity doublet model," *Phys.Rev.* **C82** (2010) 035204, arXiv:1005.4811 [hep-ph].

[156] W. Weise, "Nuclear chiral dynamics and phases of QCD," *Prog.Part.Nucl.Phys.* **67** (2012) 299–311, arXiv:1201.0950 [nucl-th].

[157] S. Fiorilla, N. Kaiser, and W. Weise, "Nuclear thermodynamics and the in-medium chiral condensate," *Phys.Lett.* **B714** (2012) 251–255, arXiv:1204.4318 [nucl-th].

[158] T. D. Cohen, R. J. Furnstahl, and D. K. Griegel, "Quark and gluon condensates in nuclear matter," *Phys. Rev. C* **45** (1992) 1881–1893.

[159] M. Gell-Mann, R. J. Oakes, and B. Renner, "Behavior of current divergences under $su_3 \times su_3$," *Phys. Rev.* **175** (1968) 2195–2199.

[160] V. Bernard, N. Kaiser, and U.-G. Meissner, "Chiral dynamics in nucleons and nuclei," *Int. J. Mod. Phys.* **E4** (1995) 193–346, arXiv:hep-ph/9501384 [hep-ph].

[161] D. Zschiesche, L. Tolos, J. Schaffner-Bielich, and R. D. Pisarski, "Cold, dense nuclear matter in a SU(2) parity doublet model," *Phys.Rev.* **C75** (2007) 055202, arXiv:nucl-th/0608044 [nucl-th].

[162] S. Wilms, F. Giacosa, and D. H. Rischke, "Pion-nucleon scattering within a gauged linear sigma model with parity-doubled nucleons," *Int.J.Mod.Phys.* **E16** (2007) 2388–2393, arXiv:nucl-th/0702076 [NUCL-TH].

[163] V. Dexheimer, S. Schramm, and D. Zschiesche, "Nuclear matter and neutron stars in a parity doublet model," *Phys.Rev.* **C77** (2008) 025803, arXiv:0710.4192 [nucl-th].

[164] S. Gallas, F. Giacosa, and D. H. Rischke, "Vacuum phenomenology of the chiral partner of the nucleon in a linear sigma model with vector mesons," *Phys.Rev.* **D82** (2010) 014004, arXiv:0907.5084 [hep-ph].

[165] C. Sasaki, H. K. Lee, W.-G. Paeng, and M. Rho, "Conformal anomaly and the vector coupling in dense matter," *Phys.Rev.* **D84** (2011) 034011, arXiv:1103.0184 [hep-ph].

[166] S. Gallas, F. Giacosa, and G. Pagliara, "Nuclear matter within a dilatation-invariant parity doublet model: the role of the tetraquark at nonzero density," *Nucl.Phys.* **A872** (2011) 13–24, arXiv:1105.5003 [hep-ph].

[167] J. Steinheimer, S. Schramm, and H. Stocker, "The hadronic SU(3) Parity Doublet Model for Dense Matter, its extension to quarks and the strange equation of state," *Phys.Rev.* **C84** (2011) 045208, arXiv:1108.2596 [hep-ph].

[168] W.-G. Paeng, H. K. Lee, M. Rho, and C. Sasaki, "Dilaton-Limit Fixed Point in Hidden Local Symmetric Parity Doublet Model," *Phys.Rev.* **D85** (2012) 054022, arXiv:1109.5431 [hep-ph].

[169] F. Giacosa, "Properties of hadrons in a chiral model with (axial-)vector mesons," *Prog.Part.Nucl.Phys.* **67** (2012) 332–336, arXiv:1111.4944 [hep-ph].

[170] S. Benic, I. Mishustin, and C. Sasaki, "An effective model for the QCD phase transitions at finite baryon density," arXiv:1502.05969 [hep-ph].

[171] D.-U. Jungnickel and C. Wetterich, "Effective action for the chiral quark-meson model," *Phys. Rev. D* **53** (1996) 5142–5175.

[172] J. Hubbard, "Calculation of partition functions," *Phys. Rev. Lett.* **3** (1959) 77–78.

[173] R. L. Stratonovich, "On a Method of Calculating Quantum Distribution Functions," *Soviet Physics Doklady* **2** (1957) 416.

[174] J. Kogut and M. Stephanov, *The Phases of Quantum Chromodynamics: From Confinement to Extreme Environments,*. Cambridge monographs on particle physics, nuclear physics, and cosmology. Cambridge University Press, 2003.

[175] M. Asakawa, Y. Nakahara, and T. Hatsuda, "Maximum entropy analysis of the spectral functions in lattice qcd," *Progress in Particle and Nuclear Physics* **46** (2001) 459 – 508.

[176] S.-x. Qin, L. Chang, Y.-x. Liu, and C. D. Roberts, "Quark spectral density and a strongly-coupled QGP," *Phys. Rev.* **D84** (2011) 014017, arXiv:1010.4231 [nucl-th].

[177] S.-x. Qin and D. H. Rischke, "Quark Spectral Function and Deconfinement at Nonzero Temperature," *Phys. Rev.* **D88** (2013) 056007, arXiv:1304.6547 [nucl-th].

[178] F. Gao, S.-X. Qin, Y.-X. Liu, C. D. Roberts, and S. M. Schmidt, "Zero mode in a strongly coupled quark gluon plasma," *Phys. Rev.* **D89** (2014) 076009, arXiv:1401.2406 [nucl-th].

[179] D. Nickel, "Extraction of Spectral Functions from Dyson-Schwinger Studies via the Maximum Entropy Method," *Annals Phys.* **322** (2007) 1949–1960, arXiv:hep-ph/0607224 [hep-ph].

[180] C. S. Fischer, J. M. Pawlowski, A. Rothkopf, and C. A. Welzbacher, "Bayesian analysis of quark spectral properties from the Dyson-Schwinger equation," arXiv:1705.03207 [hep-ph].

[181] G. Baym and N. D. Mermin, "Determination of thermodynamic green's functions," *Journal of Mathematical Physics* **2** (1961) 232–234, https://doi.org/10.1063/1.1703704.

[182] T. R. Morris, "The Exact renormalization group and approximate solutions," *Int. J. Mod. Phys.* **A9** (1994) 2411–2450, arXiv:hep-ph/9308265 [hep-ph].

[183] D. F. Litim, "Optimised renormalisation group flows," *Phys. Rev.* **D64** (2001) 105007, arXiv:hep-th/0103195.

[184] S. Fiorilla, N. Kaiser, and W. Weise, "Chiral thermodynamics of nuclear matter," *Nucl.Phys.* **A880** (2012) 65–87, arXiv:1111.2791 [nucl-th].

[185] T. D. . Cohen, "Functional integrals for QCD at nonzero chemical potential and zero density," *Phys. Rev. Lett.* **91** (2003) 222001, arXiv:hep-ph/0307089 [hep-ph].

[186] A. K. Cyrol, M. Mitter, and N. Strodthoff, "FormTracer - A Mathematica Tracing Package Using FORM," *Comput. Phys. Commun.* **219** (2017) 346–352, arXiv:1610.09331 [hep-ph].

Danksagung

Zunächst möchte ich Prof. Dr. Lorenz von Smekal dafür danken, dass er mir die Möglichkeit gegeben hat meine Doktorarbeit in seiner Arbeitsgruppe zu schreiben sowie für all die Jahre der guten Zusammenarbeit sowohl in Darmstadt als auch in Gießen. Weiterhin möchste ich Prof. Dr. Christian Fischer für die Übernahme des Zweitgutachtens dieser Arbeit recht herzlich danken. Prof. Dr. Jochen Wambach gilt Dank für seine Betreuung während meiner Darmstädter Zeit sowie Nils Strodthoff und Arno Tripolt für die interessante Zusammenarbeit.

Natürlich sollen auch die restliche Arbeitsgruppe und weitere Kollegen aus dem Institut für theoretische Physik nicht unerwähnt bleiben. Hier möchte ich insbesondere meinem langjährigen Bürokollegen Christopher Jung, sowie Lukas Holicki und Eduard Seifert für eine gute Atmosphäre und den ein oder anderen Schabernack recht herzlich danken. Besonderer Dank gilt auch Philipp Friedrich Scior für die Durchsicht dieser Arbeit und Richard Williams für seinen Rat bezüglich Dyson-Schwinger Gleichungen.

Abschließend möchte ich meinen Eltern und meiner Schwester, sowie meiner lieben Freundin Linda für die stete Unterstützung in allen Belangen meinen herzlichsten Dank aussprechen, ohne euch wäre es nicht möglich gewesen.

Erklärung zur Dissertation

Ich erkläre: Ich habe die vorgelegte Dissertation selbstständig und ohne unerlaubte fremde Hilfe und nur mit den Hilfen angefertigt, die ich in der Dissertation angegeben habe. Alle Textstellen, die wörtlich oder sinngemäß aus veröffentlichten Schriften entnommen sind, und alle Angaben, die auf mündlichen Auskünften beruhen, sind als solche kenntlich gemacht. Ich stimme einer evtl. Überprüfung meiner Dissertation durch eine Antiplagiat-Software zu. Bei den von mir durchgeführten und in der Dissertation erwähnten Untersuchungen habe ich die Grundsätze guter wissenschaftlicher Praxis, wie sie in der ,,Satzung der Justus-Liebig-Universität Gießen zur Sicherung guter wissenschaftlicher Praxis" niedergelegt sind, eingehalten.

Ort, Datum	Johannes Weyrich